FACULTY
OF MATHEMATICS
AND PHYSICS
Charles University

DOCTORAL THESIS

Michaela Mlynáriková

Cross-section measurements of the Higgs boson decaying into a pair of tau leptons with the ATLAS detector

Institute of Particle and Nuclear Physics

Supervisor of the doctoral thesis:	doc. RNDr. Tomáš Davídek, Ph.D.
Study programme:	Physics
Study branch:	Subnuclear physics

Prague 2019

I declare that I carried out this doctoral thesis independently, and only with the cited sources, literature and other professional sources.

I understand that my work relates to the rights and obligations under the Act No. 121/2000 Sb., the Copyright Act, as amended, in particular the fact that the Charles University has the right to conclude a license agreement on the use of this work as a school work pursuant to Section 60 subsection 1 of the Copyright Act.

In Prague, 6th June 2019

I would like to thank numerous people, although I mention here only a few of them with whom I closely collaborated during my PhD studies.

To Tomáš Davídek, my supervisor, you have my most sincere gratitude for admitting me as a young student with no previous experience in experimental particle physics. During the last four years you gave me a great deal of support from you and I am very grateful I had an opportunity to collaborate with you. Your enthusiasm encouraged me not to give up during the difficult times and I truly appreciate the freedom you gave me throughout my stay at CERN.

To Daniel Scheirich, my consultant, I really appreciate the incredible patience you have shown during our never-ending discussions about the fit model, likelihood functions or constrained nuisance parameters. Thank you for introducing me to statistics and for watching over me for the last couple of years.

To Jana Faltová, my consultant, thank you for many physics and non-physics related chats, support and advices you gave me.

To Elias Coniavitis, the former fit expert of the HLepton group, thank you for introducing me to the fit machinery and passing your knowledge to me, so I was able to become a fit expert in our group after you left CERN.

To Quentin Buat and Pier-Olivier DeViveiros, outstanding conveners of the HLepton group, thank you for your leadership, support and trust you had in me.

To Antonio De Maria, my best colleague and friend, thank you for always keeping an eye on me and the countless coffees and dinners you prepared for me.

Eventually, I would like to express my utmost gratitude to my family, colleagues and friends for your patience and support.

At this place, I take the liberty to acknowledge the financial support provided by Ministry of Education, Youth and Sports – Research infrastructure CERN-CZ and Inter-Excellence/Inter-Transfer (Grant. No. LTT17018), and Charles University (Project No. UNCE/SCI/013).

Title: Cross-section measurements of the Higgs boson decaying into a pair of tau leptons with the ATLAS detector

Author: Michaela Mlynáriková

Institute: Institute of Particle and Nuclear Physics (IPNP)

Supervisor: doc. RNDr. Tomáš Davídek, Ph.D., IPNP

Abstract: The ATLAS experiment is one of the two general-purpose detectors at the Large Hadron Collider (LHC) at the European Organisation for Nuclear Research (CERN) in Switzerland. ATLAS is designed for precision measurements of particle properties, the search of the Higgs boson and new physics beyond the Standard Model. The experiment got worldwide attention in 2012, when after the collaborative efforts with the CMS experiment the Higgs boson discovery was announced. After the discovery, the precision measurements of its properties became one of the main objectives of the LHC physics programme, since a potential observation of deviations from the Standard Model predictions might lead to the discovery of new physics.

In this thesis, the measurements of the Higgs boson production cross-sections in the $H \to \tau\tau$ decay channel are presented. Based on the proton-proton collision data collected at the centre-of-mass energy of 13 TeV in years 2015 and 2016, the signal over the expected background from the other Standard Model processes is established with the observed significance of 4.4σ. Combined with the data collected at 7 and 8 TeV, the observed signal significance amounts to 6.4σ, which constitutes a single experiment observation of the $H \to \tau\tau$ decays by ATLAS. All presented results are found to be consistent with the Standard Model predictions.

In addition to the analysis, we introduce the topic of time calibration of the Tile Calorimeter and its subsequent time stability monitoring during the data taking in years 2015 and 2016.

Keywords: Higgs boson, Statistical analysis, Tile Calorimeter, Time calibration

Contents

Introduction

The Large Hadron Collider (LHC) [1] is a proton-proton (pp) accelerator built in the European Organisation for Nuclear Research (CERN). It is designed to collide two proton beams at the centre-of-mass energy ($\sqrt{s}$) of 14 TeV at the luminosity of $10^{34}\,\mathrm{cm}^{-2}\mathrm{s}^{-1}$. ATLAS (A Toroidal LHC Apparatus)[2] is one of the multipurpose detectors built at the LHC designed to study the widest possible range of physics processes.

The Standard Model (SM) of particle physics [3, 4, 5] describes all currently known fundamental particles – fermions and bosons, and their interactions. It has successfully passed many experimental tests such as the prediction of intermediate vector bosons W and Z existence. Moreover, it predicts the existence of the Higgs boson, whose direct observation was the last missing piece of the SM for long decades. The Higgs boson is a scalar particle emerging the SM as a leftover of the Brout-Englert-Higgs mechanism (BEH mechanism), which generates masses of the fundamental particles in the SM by utilising the electroweak symmetry breaking mechanism.

In 2012, the ATLAS and CMS [6] collaborations discovered a particle with a mass of approximately 125 GeV consistent with the SM Higgs boson. The excess of events with a signal significance greater than 5σ was observed in the decays to $\gamma\gamma$, WW^* and ZZ^* [7, 8].

The Higgs boson coupling to fermions has been established with the observation of the $H \to \tau\tau$ decay mode, which was discovered combining ATLAS and CMS results obtained by analysis data collected in years 2011 and 2012 [9, 10, 11]. The Higgs boson couplings to other fermions such as top and bottom quarks [12, 13, 14, 15] have been observed as well. However, only upper limits exist on its coupling to muons [16, 17] and thus $H \to \tau\tau$ has been the only leptonic decay mode accessible with the currently available datasets.

The Higgs boson properties, such as its coupling strengths, spin and charge-parity (CP) quantum numbers were predominantly studied in the bosonic decay modes [18, 19, 20, 21] and have not shown any significant deviations from the SM expectations.

The main part of this work describes the author's contribution to the measurements of the Higgs boson production cross-section in its decays to a pair of tau leptons. The data used for these measurements were collected by the ATLAS detector in pp collisions at $\sqrt{s} = 13$ TeV in years 2015 and 2016. Combining the results presented in this thesis with Run 1 results led to the single experiment discovery of the Higgs boson decays to a pair of tau leptons at the ATLAS experiment [22].

Furthermore, we introduce in detail the hadronic Tile Calorimeter (TileCal) [23] of the ATLAS experiment and its time calibration. The TileCal provides essential input to the measurement of jet energies and to the missing transverse energy reconstruction. The amount of energy deposited by the incident particle in the corresponding calorimeter cell is proportional to the maximum height of the analogue pulse in one channel. The electrical signal for each channel is reconstructed from seven consecutive digital samples taken every 25 ns. The goal of the time calibration is to reconstruct the signal pulse in such a manner that the maximum of the signal peak corresponds to the central sample. This correction is necessary due to the fluctuations in particle travel time, channel-to-channel differences in the signal propagation time and uncertainties in the electronics read-out. The incorrect time calibration and consequently the incorrect signal reconstruction may lead to the inaccurate energy reconstruction. Moreover, the correct channel time is necessary for the object selection and time-of-flight analyses searching for hypothetical long-lived particles entering the calorimeter. Usually, the time calibration is performed each year before the start of the data taking. During the data taking, sudden changes in time settings might occur for some channels. It is, therefore, necessary to monitor the time stability during the data taking and if needed, to provide the corrections to the time constants saved in the database.

The thesis is structured as follows: Chapter 1 introduces the theoretical foundations of the analysis and briefly summarises the Higgs boson searches and measurements of its properties. Chapter 2 describes the ATLAS detector at the LHC. Chapter 3 describes in more detail the hadronic Tile Calorimeter of the ATLAS detector and its time calibration. In Chapter 4, we present the strategies used in high-energy physics for developing a statistical model of data. Chapter 5 gives an overview of the measurement of the Higgs boson production cross-section in its decays to a pair of tau leptons with the ATLAS detector.

1. The Higgs boson of the Standard Model

The SM of particle physics [3, 4, 5] is a theory which describes all currently known fundamental particles – fermions and bosons, and their interactions. An overview of these particles together with their masses, spin and electric charge quantum numbers is shown in Figure 1.1.

The SM predicts the existence of one scalar boson (spin 0) – the Higgs boson. All other fundamental bosons in the SM are vector fields (spin 1) and they mediate the fundamental interactions. Massive W and Z bosons mediate the weak force, while a massless photon γ and gluons g mediate the electromagnetic and strong interaction, respectively.

In general, the SM is based on the local $SU(3)_c \times SU(2)_L \times U(1)_Y$ gauge symmetry, where c denotes colour, L weak isospin and Y weak hypercharge. The non-Abelian $SU(3)_c$ gauge symmetry drives the strong interaction between quarks and gluons, while the $SU(2)_L \times U(1)_Y$ gauge symmetry rules the electroweak interaction. The gauge theories predict the intermediate vector bosons to be massless, while the $SU(2)_L$ symmetry forbids massive chiral fermions. However, it is well known from experiments that the intermediate vector bosons W and Z have non-zero masses. These can be introduced in the SM via the BEH mechanism [24, 25, 26, 27, 28] by introducing an $SU(2)_L$ doublet scalar field Φ, the BEH field. It can be written as

$$\Phi = \begin{pmatrix} \phi^+ \\ \phi^0 \end{pmatrix} , \tag{1.1}$$

where the two complex components ϕ^+ and ϕ^0 are equivalent to four real fields. Due to its non-vanishing vacuum expectation value $v = \sqrt{2}\langle\Phi_0\rangle$, it reduces the electroweak gauge symmetry to the electromagnetic gauge symmetry $U(1)_{EM}$. Hence, the ground state of the theory is invariant only under the strong $SU(3)_c$ and the electromagnetic $U(1)_{EM}$ gauge symmetries and thus leaving gluons and photon massless. Three degrees of freedom of Φ are absorbed in the mass terms of the Z and W bosons, while the remaining degree of freedom results in a physical state – the Higgs boson. The Higgs boson mass is a free parameter within the theory. Additionally, in the theory with massive W and Z bosons, the Higgs boson ensures the unitarity of tree-level scattering amplitudes at high energies.

The Higgs boson couplings to all fundamental particles are proportional to the particles' masses. For the intermediate vector bosons W and Z, their masses are predicted to be

$$m_Z = \frac{1}{2} v \sqrt{g^2 + g'^2} \tag{1.2}$$

and

$$m_W = \frac{1}{2} v g, \tag{1.3}$$

where g and g' are the $SU(2)_L$ and $U(1)_Y$ gauge coupling constants, respectively. The BEH mechanism can be utilised to generate masses of fermions as well. An interaction between the BEH field and fermion fields is driven through the Yukawa

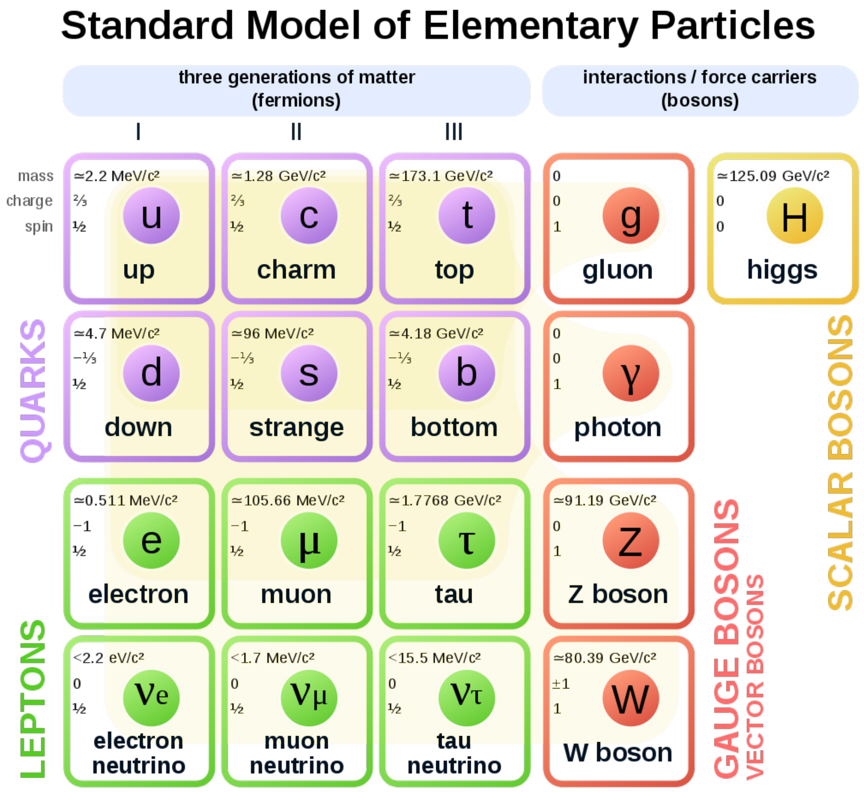

Figure 1.1: The fields of the Standard Model with their respective masses, spin and electric charge quantum numbers. Fermions are arranged in three families, each containing a pair of quarks (violet) and a pair of leptons (green) with the same quantum numbers, but different masses. Bosons (red) include the vector bosons, which mediate the fundamental interactions, and the scalar Higgs boson (yellow). The massless photon mediates the electromagnetic force between all electrically charged particles. The eight massless gluons mediate the strong interaction between quarks and gluons. The massive W and Z bosons mediate the weak interaction. The massive scalar Higgs boson couples to all massive particles. For electrically neutral neutrinos, it is not yet known whether they are different from their anti-particles [29].

interaction. The coupling constant for the Yukawa interaction is proportional to the fermion mass

$$g_{ffH} = -\frac{m_f}{v}. \tag{1.4}$$

1.1 Higgs boson production

The main Higgs boson production processes at the LHC are: gluon–gluon fusion (ggF), vector boson fusion (VBF), the associated production of a Higgs boson with a vector boson (VH, where V is W or Z boson) and the associated production of a Higgs boson with a top-antitop or bottom-antibottom quark pair ($t\bar{t}H$ or $b\bar{b}H$). Examples of leading-order Feynman diagrams of these processes are shown in Figure 1.2. In this section we assume the Higgs boson mass to be $m_H = 125\,\text{GeV}$ [30].

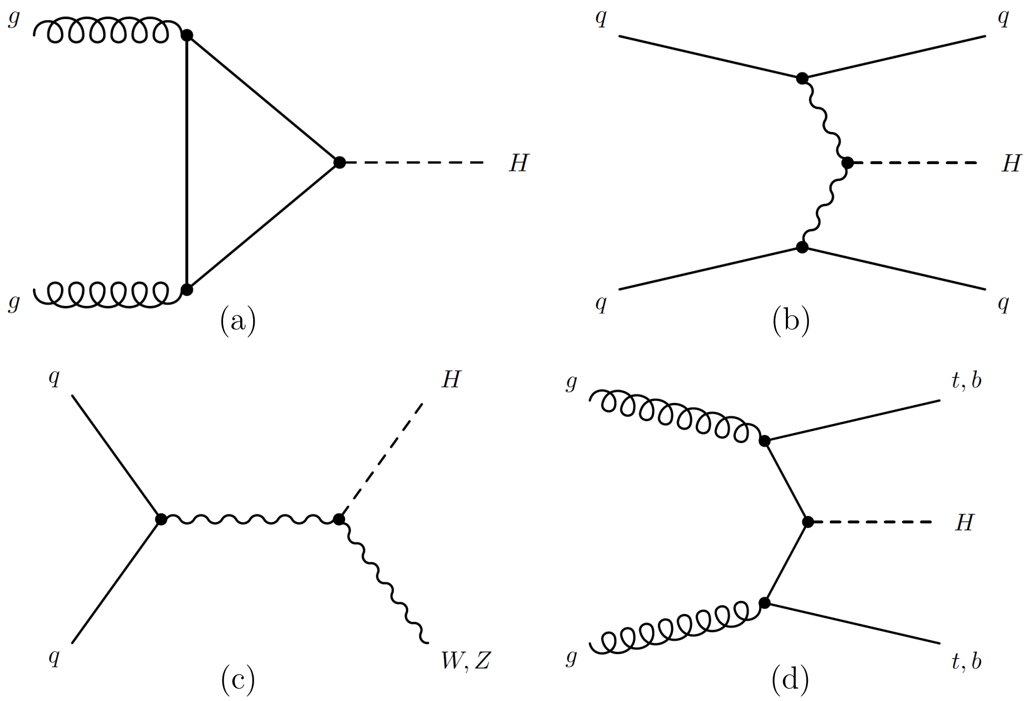

Figure 1.2: Examples of leading-order Feynman diagrams of the Higgs boson production modes: (a) gluon–gluon fusion, (b) vector boson fusion, (c) the associated production of a Higgs boson with a vector boson (VH, where V is W or Z boson) and (d) the associated production of a Higgs boson with a top-antitop or bottom-antibottom quark pair ($t\bar{t}H$ or $b\bar{b}H$) [32].

The corresponding production cross-sections σ in pp collisions at the centre-of-mass energy $\sqrt{s} = 13\,\text{TeV}$ are shown as the function of the Higgs boson mass m_H [31] in the left plot in Figure 1.3. The production cross-section values listed in Table 1.1 taken from [31] correspond to those used in the measurement presented in Section 5.

The dominant Higgs boson production mode at the LHC is the ggF, with the main contribution from the top quark loop, since the Higgs boson coupling to fermions is proportional to the fermion mass. The cross-section depends on the parton distribution function (PDF) of a gluon in a proton and on the quantum chromodynamics (QCD) radiative corrections.

In the second highest production cross-section mode, VBF, each of the two initial quarks radiates one vector boson. The two vector bosons annihilate and produce the Higgs boson, while the two radiated quarks subsequently hadronise and form two jets, which are emitted predominantly to the forward region of the detector. Even though its production cross-section is an order of magnitude smaller than for ggF, VBF is very important Higgs boson production mechanism, due to its typical final state topology with the two jets.

To test the SM predictions, it is necessary to explore all accessible production mode processes. The Yukawa couplings of the Higgs boson to fermions determines the ggF, while VBF depends on the coupling to the weak vector bosons. Similarly, the $t\bar{t}H$ production allows for the direct measurement of the top quark Yukawa coupling.

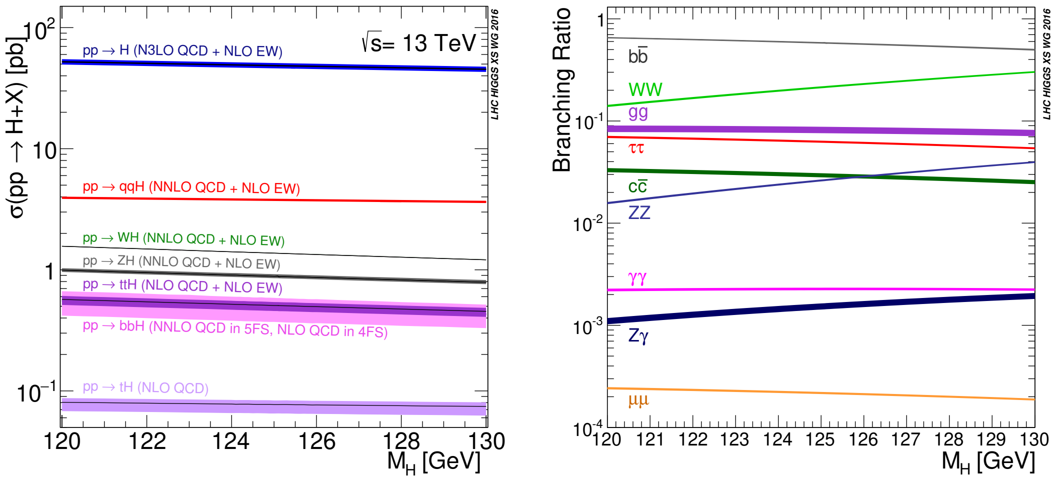

Figure 1.3: Left: The SM Higgs boson production cross-sections near $m_H = 125\,\text{GeV}$ in pp collisions at $\sqrt{s} = 13\,\text{TeV}$. Theoretical uncertainties are indicated as bands [31]. Right: Branching ratios for the main decays of the SM Higgs boson near $m_H = 125\,\text{GeV}$. Theoretical uncertainties are indicated as bands [31].

Table 1.1: The SM Higgs boson production cross-sections for $m_H = 125\,\text{GeV}$ in proton-proton collisions at $\sqrt{s} = 13\,\text{TeV}$ [31].

process	ggF	VBF	WH	ZH	$t\bar{t}H$	total
cross-section [pb]	$44.1^{+11\%}_{-11\%}$	$3.78^{+2\%}_{-2\%}$	$1.37^{+2\%}_{-2\%}$	$0.88^{+5\%}_{-5\%}$	$0.51^{+9\%}_{-13\%}$	50.6

1.2 Higgs boson decay modes

The Higgs boson coupling to the final-state particles determines the branching ratios $\mathcal{B}$ of the Higgs boson decays, which is shown as a function of m_H in the right plot in Figure 1.3. The values of $\mathcal{B}$ and corresponding relative uncertainties for the Higgs boson with $m_H = 125\,\text{GeV}$ are shown in Table 1.2.

The Higgs boson with a mass of 125 GeV most frequently decays into a bottom-antibottom quark pair, since b quarks are the heaviest particles which can be produced on-shell. However, due to the large QCD background, this decay mode is very difficult to analyse. On the other hand, the $H \to \tau\tau$ decay mode, which has the second highest $\mathcal{B}$ among the Higgs boson decays to fermions, provides good discrimination between the signal and background processes. Decays into a pair of c quarks are very difficult to distinguish from the QCD background, which in combination with the low $\mathcal{B}$ of this decay makes its observation impossible using the currently available datasets. Although $H \to \mu\mu$ provides a very clean signature in the detector due to the high di-muon invariant mass resolution, the decay suffers from extremely small $\mathcal{B}$ and thus its experimental measurement is very challenging.

The Higgs boson decays into two weak vector bosons are suppressed, since

Table 1.2: Branching ratios and relative uncertainties for a SM Higgs boson with $m_H = 125\,\text{GeV}$ [33].

Decay channel	Branching ratio	Rel. uncertainty [%]
$H \to \gamma\gamma$	2.27×10^{-3}	$+5.0/-4.9$
$H \to ZZ^*$	2.62×10^{-2}	$+4.3/-4.1$
$H \to WW^*$	2.14×10^{-1}	$+4.3/-4.2$
$H \to \tau\tau$	6.27×10^{-2}	$+5.7/-5.7$
$H \to b\bar{b}$	5.84×10^{-1}	$+3.2/-3.3$
$H \to Z\gamma$	1.53×10^{-3}	$+9.0/-8.9$
$H \to \mu\mu$	2.18×10^{-4}	$+6.0/-5.9$

only one of two bosons can be produced on-shell. This means that the accessible decays are $H \to WW^*$, $H \to ZZ^*$ and $H \to \gamma\gamma$. The $H \to \gamma\gamma$ decays occur only in the second order perturbation theory through W boson or top quark loop, thus resulting in a very small $\mathcal{B}$. However, $H \to \gamma\gamma$ decay has a very clear signature and high di-photon invariant mass resolution. The decay to a pair of gluons is impossible to study on hadron colliders due to the presence of large QCD background.

To suppress large contribution from higher order QCD processes to the production cross-section, in many Higgs boson analyses (including the one presented in Section 5), we consider only the events with at least one additional jet. In such cases, the Higgs boson recoils against the jet(s) and obtains significant momentum, which helps to identify the events with the Higgs boson.

1.3 Higgs boson discovery and measurements of its properties

One of the main motivations for the construction of the LHC was the search for the Higgs boson in pp collisions. The collider commenced its operation in November 2009 and the first period of physics data taking lasted until spring 2013. Data samples collected during this period at $\sqrt{s} = 7$ and $8\,\text{TeV}$ correspond to integrated luminosities of about $5\,\text{fb}^{-1}$ and $20\,\text{fb}^{-1}$, respectively. The resulting dataset is generally referred to as Run 1. The LHC was shut down in February 2013 for its two-year upgrade called Long Shutdown 1 (LS1). The LHC restarted again in April 2015 and data taking continued at $\sqrt{s} = 13\,\text{TeV}$ until the end of 2018. This period of data taking is referred to as Run 2 and collected data correspond to an integrated luminosity of about $150\,\text{fb}^{-1}$.

The Higgs boson searches at the LHC used Run 1 dataset, which covered the mass range up to about $1\,\text{TeV}$ [34]. The Higgs boson was discovered in 2012 by the ATLAS and CMS experiments in decays to $\gamma\gamma$, WW^* and ZZ^* [7, 8]. Data used for this discovery correspond to an integrated luminosity of about $11\,\text{fb}^{-1}$ of Run 1 dataset collected by each experiment. This discovery has later been

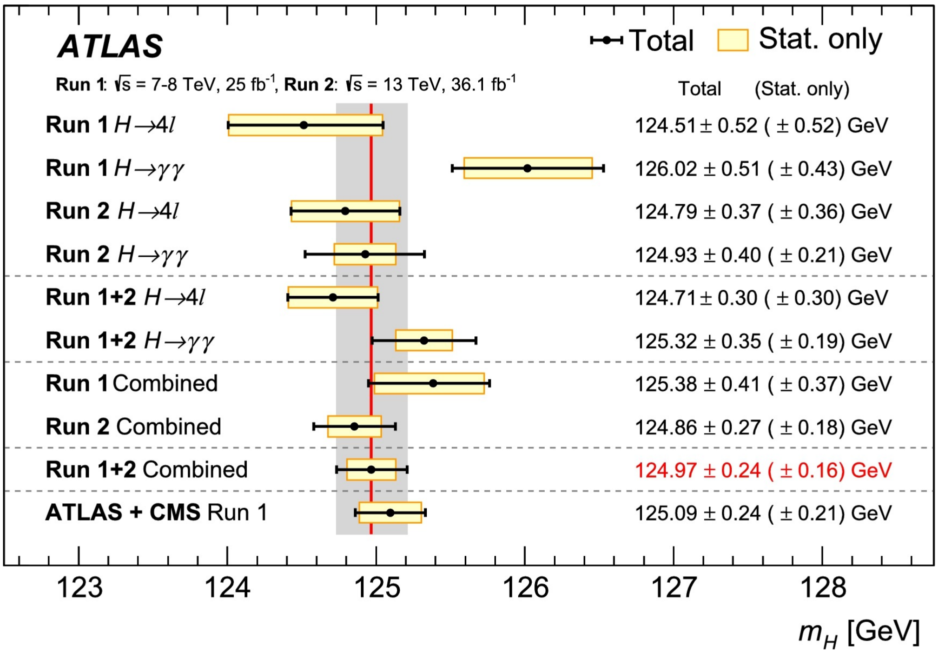

Figure 1.4: The summary of the Higgs boson mass measurements from the individual and combined analyses. It shows the results obtained by analysing $36.1\,\mathrm{fb}^{-1}$ of Run 2 dataset recorded by the ATLAS experiment [36], in comparison with the combined Run 1 measurement by the ATLAS and CMS [30] collaborations. The statistical-only (horizontal yellow-shaded bands) and total (black error bars) uncertainties are indicated. The (red) vertical line and corresponding (grey) shaded column indicate the central value and the total uncertainty of the combined ATLAS Run 1+2 measurement, respectively.

confirmed in di-boson final states by analysing full Run 1 dataset, resulting in increased precision of the measurement.

The observation of the $H \to \tau\tau$ decay mode established the Higgs boson coupling to fermions with a signal significance of 5.5 standard deviations σ by combining the results from the ATLAS and CMS experiments results [9, 10, 11] using Run 1 dataset. Moreover, the CMS collaboration used $35.9\,\mathrm{fb}^{-1}$ of Run 2 dataset and reached the signal significance of 4.9σ and 5.9σ by combining these results with Run 1 measurement [35]. Recently, we have observed the Higgs-boson coupling to other fermions such as top quarks [12, 13] and bottom quarks [14, 15]. On the other hand, on the Higgs boson coupling to muons [16, 17] only upper limits exist and the $H \to \tau\tau$ decay mode has been the only accessible leptonic decay mode.

The properties of the new particle such as mass, spin and CP quantum numbers as well as the production modes and decay rates have been predominantly measured in di-boson decays [18, 19, 20, 21] and are in agreement with the SM predictions for the Higgs boson.

Below, we present measurements conducted by the ATLAS experiment, however, one should note that the results from the ATLAS and CMS experiments' measurements are in agreement.

The Higgs boson mass measurement is performed using $H \to \gamma\gamma$ and $H \to ZZ^* \to 4\ell$ final states due to the high mass resolution. By combining these two channels, the mass is measured to be $m_H = 124.97 \pm 0.24\,\text{GeV}$ [36] by using both, the Run 1 and $36.1\,\text{fb}^{-1}$ of Run 2 datasets. The results are shown in Figure 1.4.

Combined measurements of the Higgs boson production cross-sections, $\mathcal{B}$ and couplings are summarised in Figure 1.5 [37]. These results combine the Higgs boson decays into $\gamma\gamma$, ZZ^*, WW^*, $\tau\tau$, $\mu\mu$ and $b\bar{b}$ using up to $79.8\,\text{fb}^{-1}$ of Run 2 dataset.

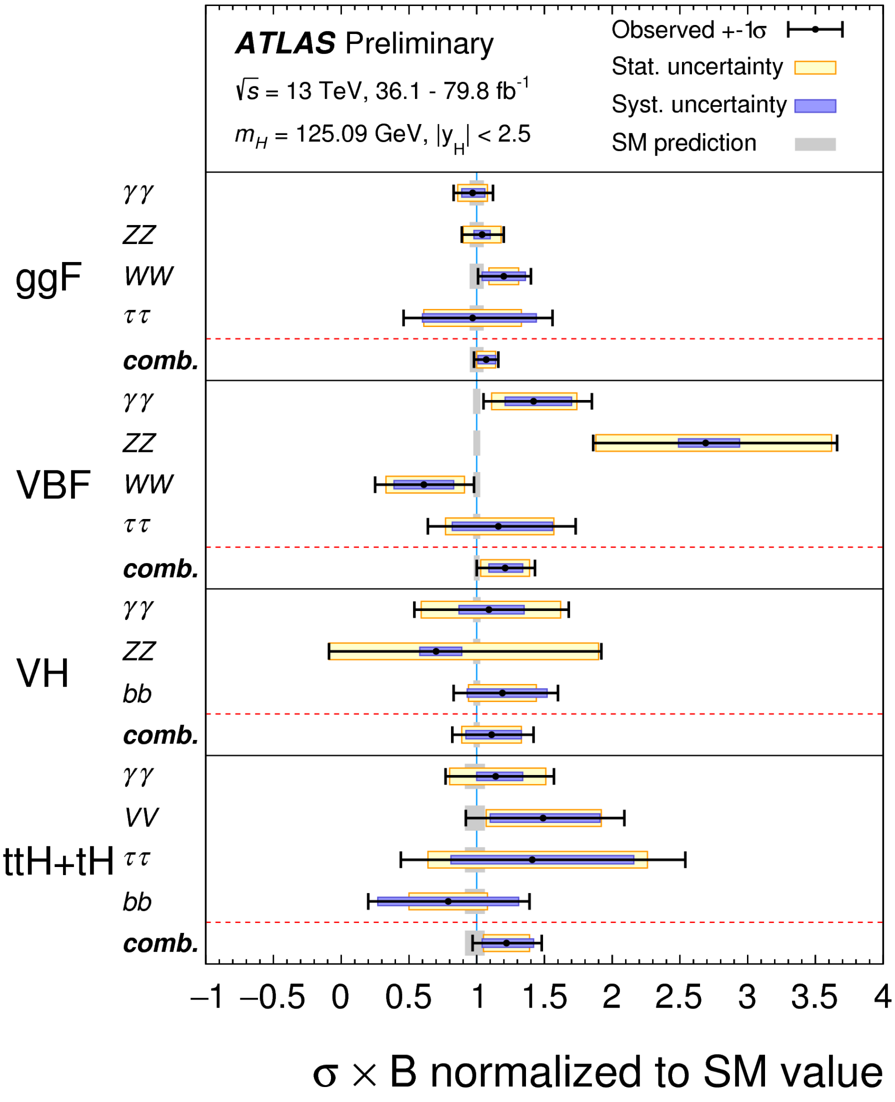

Figure 1.5: Measured $\sigma \times \mathcal{B}$ for ggF, VBF, VH and $t\bar{t}H+tH$ production mechanism in each relevant decay mode, normalised to their SM predictions [37]. The values were obtained from a simultaneous fit to all decay channels. The cross-section for the VH and $t\bar{t}H$ for $H \to \tau\tau$ process is fixed to its SM prediction. Combined results for each production mode are also shown, assuming SM values for $\mathcal{B}$ into each decay mode. The black error bars, blue boxes and yellow boxes show the total, systematic, and statistical uncertainties in the measurements, respectively. The grey bands show the theory uncertainties in the predictions.

2. The Large Hadron Collider and the ATLAS experiment

2.1 Large Hadron Collider

The LHC [1] is a circular accelerator with the circumference of approximately 27 km lying beneath the French-Swiss border. Its goal is to study particle physics processes at energies and luminosities that have not been reached before. The LHC is constructed to collide two proton beams at the centre-of-mass energy of 14 TeV and the luminosity of $10^{34}\,\mathrm{cm}^{-2}\,\mathrm{s}^{-1}$. In order to reach the energy of 7 TeV per beam, superconducting magnets capable to generate a magnetic field of 8.3 T are needed to bend the beams in a ring of a given circumference. By design, proton beams in the LHC are composed of 2808 bunches spaced by 25 ns with each bunch containing 1.15×10^{11} protons. As the result of high instantaneous luminosity, several *pp* interactions occur in the same bunch crossing (event). This effect is called pileup.

Around the LHC ring, proton beams intersect at four interaction points (IPs) where four detectors are installed: ALICE [38], ATLAS [2], CMS [6] and LHCb [39]. ATLAS and CMS are multipurpose detectors designed to test the SM and search for new physics at TeV scale. ALICE specialises in heavy ion physics and LHCb focuses on B-meson physics.

2.2 ATLAS detector

The purpose of the ATLAS detector is to reconstruct and identify all products emerging from the collisions at the LHC. Since different kinds of particles interact with detector materials in different ways, the particles can be distinguished based on the signal they leave in various detector components. Although, some particles such as neutrinos do not leave any signature, their presence in the detector can be established by computing the missing transverse energy $E_{\mathrm{T}}^{\mathrm{miss}}$.

Figure 2.1 shows a schematic view of the ATLAS detector. Its sub-detectors can be divided into three categories: tracking detectors, which are closest to the beam pipe, followed by the calorimeters and the muon system, which covers the outermost part of the detector. The measurement of the particles' momenta is based on the curvature of the reconstructed tracks, thus the tracking detectors are embedded in a 2 T strong solenoidal magnetic field. Cylindrical parts in the central region of the detector form the so-called barrel with end-caps placed at each end of the barrel-shaped detector. The main requirements on the detector design are:

- Efficient reconstruction of the interaction vertices.
- High reconstruction efficiency of particle tracks and good momentum resolution.
- Precise electromagnetic and hadronic energy measurements in the calorimeters for the reconstruction and identification of photons, electrons, muons, hadronic tau decays, jets and $E_{\mathrm{T}}^{\mathrm{miss}}$.

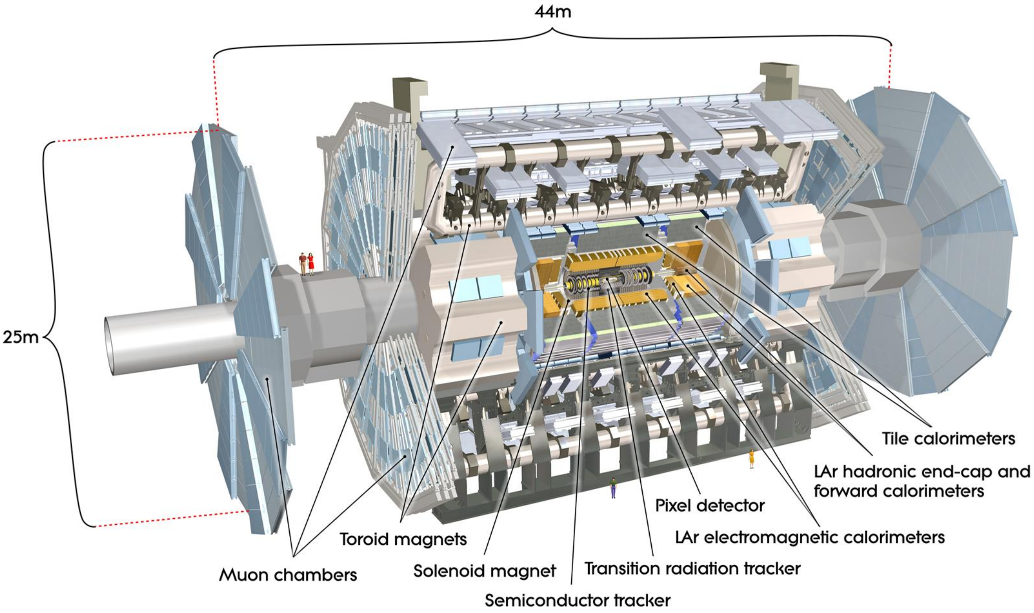

Figure 2.1: A schematic overview of the ATLAS detector [2].

- High granularity and solid angle coverage.

The ATLAS uses a right-handed coordinate system [2] with the origin at the nominal IP. The z-axis runs along the beam pipe, the y-axis points upwards to the Earth's surface and the x-axis points from the IP to the centre of the LHC ring. The xy plane, referred to as the transverse plane, is often described in terms of $R-\phi$ coordinates. The azimuthal angle ϕ is measured from the x-axis around the beam pipe, while the radial dimension R measures the distance from the beam pipe. The polar angle θ is defined as the angle from the positive z-axis. However, instead of the polar angle, we frequently use the pseudorapidity η defined as

$$\eta = -\ln \tan(\theta/2). \tag{2.1}$$

The pseudorapidity equals to the Lorentz invariant rapidity y in the limit of massless particles

$$y = \frac{1}{2} \ln \left(\frac{E + p_z}{E - p_z} \right), \tag{2.2}$$

where E is the energy of a particle and p_z its momentum component along the beam axis. Transverse momentum and energy are defined as $p_{\mathrm{T}} = p \sin\theta$ and $E_{\mathrm{T}} = E \sin\theta$, respectively. The angular separations between the particle tracks are measured by the distance $\Delta R = \sqrt{(\Delta\phi)^2 + (\Delta\eta)^2}$ in the $\eta - \phi$ plane.

2.2.1 Inner detector

The inner detector (ID) system [41] consists of three sub-detectors exploiting different techniques of particle detection: a silicon pixel detector including the Insertable B-Layer (IBL) detector, the semiconductor tracker (SCT) and the transition radiation tracker (TRT). These are used to reconstruct the charged

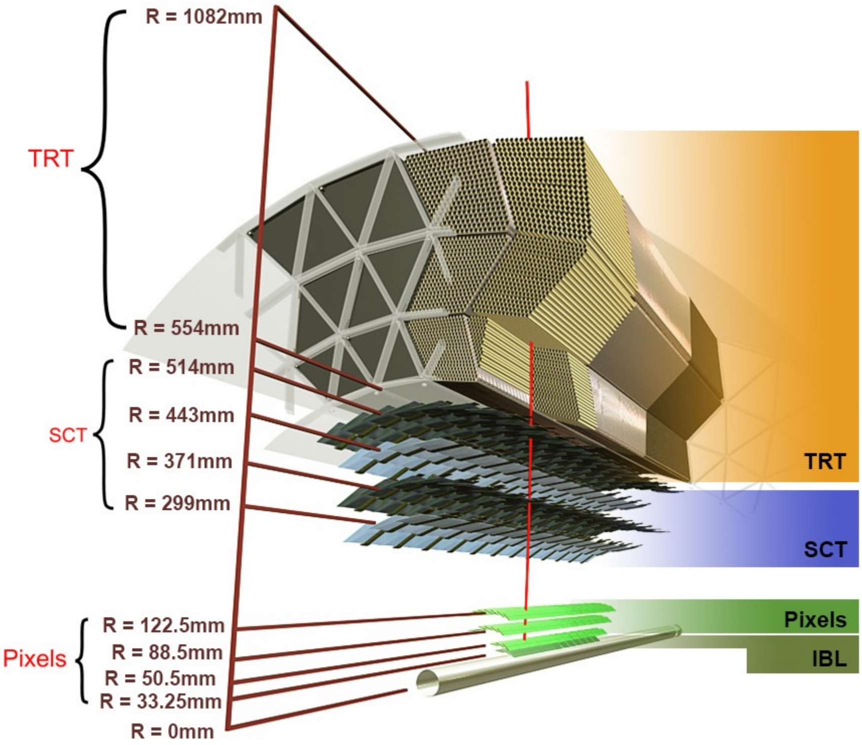

Figure 2.2: A sketch of the ATLAS inner detector showing all its components, including the Insertable B-Layer (IBL) detector. The distances to the interaction point are also shown [40].

particles' tracks, measure the position of the initial *pp* interaction, the primary vertex, or secondary vertices, and identify electrons. The ID system layout is shown in Figure 2.2.

In the barrel region, the pixel and SCT detector layers form concentric cylinders around the beam axis, while the TRT straws are parallel to the beam line. In the end-cap regions, all tracking elements are mounted on discs perpendicular to the beam axis.

The ATLAS Pixel Detector is composed of three layers of silicon pixel detectors and provides the highest granularity of the three sub-detectors. It uses silicon sensors with a nominal size of $50\,\mu\text{m} \times 400\,\mu\text{m}$ and its expected resolution is $10\,\mu\text{m}$ $(R-\phi) \times 115\,\mu\text{m}$ (z).

During the LS1, the IBL has been added to the pixel detector as an additional layer, in order to reduce the distance from the IP to the first tracking layer. It consists of silicon pixel modules, which surround the beam pipe at a mean radius of 33 mm. The expected hit resolution with conventional clustering is $\sim 8\,\mu\text{m}$ $(R-\phi) \times 40\,\mu\text{m}$ (z) [42].

The SCT is a silicon microstrip detector with multiple layers, each consisting of two sets of strips glued together at the 40 mrad angle[1], thus allowing for a two-dimensional measurement. Four layers are used in the SCT barrel region and provide a spatial resolution of $17\,\mu\text{m}$ $(R-\phi) \times 580\,\mu\text{m}$ (z). Nine disks with one set of strips running radially are placed in the end-cap region. The SCT is able to distinguish tracks if they are separated by more than 200 µm.

---

[1] One set of strips in each layer is parallel to the direction of the beam.

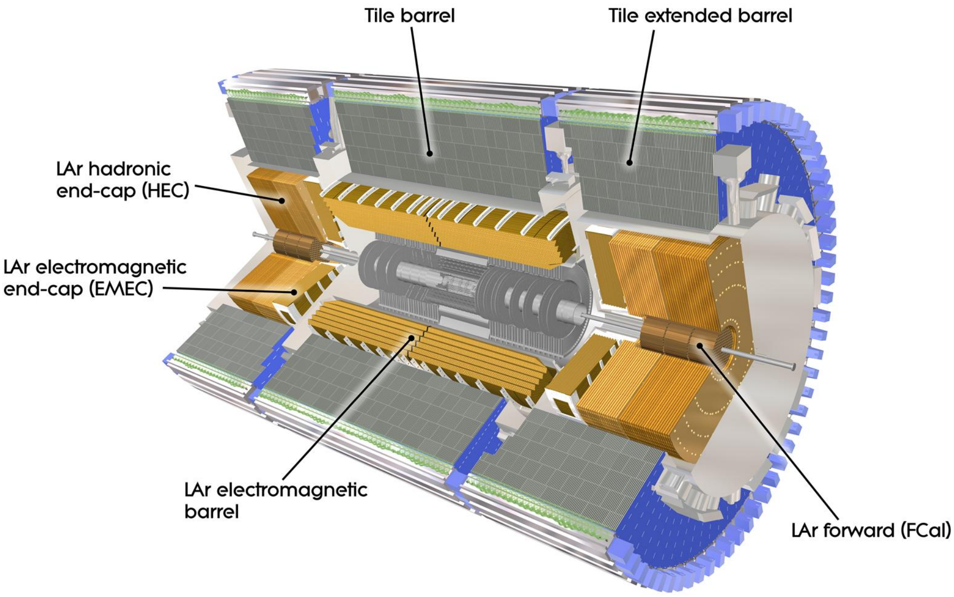

Figure 2.3: The calorimetry system of the ATLAS detector [43].

Both silicon detectors cover the pseudorapidity region up to $|\eta| < 2.5$ and they are complemented by 4 mm diameter straw tubes of the TRT, which provide track measurement in $R - \phi$ up to $|\eta| < 2.0$. The straw tubes are filled with a Xe-based gas mixture and have an unique ability to identify electrons by detecting the transition radiation photons. The TRT measures typically 36 hits per track with a hit position accuracy of 130 µm per straw.

A track is usually considered to be of good quality if it crosses three pixel layers and eight strip layers. The designed resolution of the tracking system is

$$\frac{\sigma_{p_\mathrm{T}}}{p_\mathrm{T}} = 0.05\% p_\mathrm{T} \oplus 1\%, \tag{2.3}$$

with p_T in GeV.

2.2.2 Calorimetry system

The calorimetry system, shown in Figure 2.3, embodies different types of sampling calorimeters covering the total pseudorapidity range $|\eta| < 4.9$. Its goal is to measure the energy and direction of the particles emerging from the collision. The fine granularity of the electromagnetic calorimeter [44, 45] in the region matched to the ID is necessary for electron and photon measurements. The coarser granularity of hadronic calorimeters [23, 44, 46] is sufficient for jet reconstruction and $E_\mathrm{T}^\mathrm{miss}$ measurement.

One of the key features of calorimeters is their depth, which determines their ability to absorb electromagnetic and hadronic showers. The total depth of electromagnetic calorimeters is at least 22 radiation lengths X_0 in the central region and 24 X_0 in the forward region.

The total thickness of electromagnetic and hadronic calorimeters combined amounts to approximately 10 interaction lengths. Sufficient thickness of the calorimeter together with the high $|\eta|$-coverage ensures a precise $E_{\mathrm{T}}^{\mathrm{miss}}$ measurement. This is important in many measurements of the SM particles properties, including the measurement presented in Chapter 5.

The designed resolution of the calorimeters is (with E in GeV) [2, 45, 23]:

- Electromagnetic calorimeter ($|\eta| < 3.2$): $\frac{\sigma}{E} = \frac{10\%}{\sqrt{E}} \oplus 0.7\%$.
- Hadronic calorimeter (jets):
  - Barrel and end-cap ($|\eta| < 3.2$): $\frac{\sigma}{E} = \frac{50\%}{\sqrt{E}} \oplus 3\%$.
  - Forward region ($3.1 < |\eta| < 4.9$): $\frac{\sigma}{E} = \frac{100\%}{\sqrt{E}} \oplus 10\%$.

Electromagnetic calorimeters

An electromagnetic calorimeter is a lead-LAr sampling calorimeter consisting of kapton electrodes interleaved with lead absorber plates. The electrodes have an accordion-shape and thus provide complete ϕ symmetry without any azimuthal cracks. In the region of $|\eta| < 2.5$, which is the most important for precision measurements, the calorimeter consists of three longitudinal segments.

The first layer allows for accurate positioning measurement because of its fine segmentation. The second layer collects the largest fraction of an electromagnetic shower. Usually, only the tail of the shower can reach the third layer, therefore its coarser segmentation is sufficient.

Electrons and photons lose energy as they enter the calorimeter. In order to measure the energy losses and correct for them, a presampler, which consists of an active 1.1 cm (0.5 cm) thick LAr layer in the barrel (end-cap) region, is placed in the region $|\eta| < 1.8$.

Hadronic calorimeters

The ATLAS detector accommodates three hadronic calorimeters: the TileCal [23], Hadronic End-cap Calorimeter (HEC) [44] and Forward Calorimeter (FCal) [46]. The TileCal, which uses scintillating tiles and steel absorber plates and covers the pseudorapidity range $|\eta| < 1.7$, is described in detail in Chapter 3. The HEC is a LAr sampling calorimeter with copper-plate absorber that covers the pseudorapidity range from $1.5 < |\eta| < 3.2$. The FCal covers the region of $|\eta| < 4.9$ and it uses LAr as the active medium. It is divided into three modules in each end-cap. The first one uses copper as an absorber and is optimised for electromagnetic measurements, while the other two modules use tungsten to measure mainly the deposition of hadronic energy.

2.2.3 Muon system

The muon system [47] uses the arrangement of toroidal magnets and gaseous detectors to identify muons and measure their momenta. It covers the region of $|\eta| < 2.7$ and consists of 8 superconducting toroidal coils in the central region as well as in each end-cap region. In addition, the muon system includes the trigger chambers that provide fast signals.

In the barrel region, the spectrometer chambers form three cylindrical layers around the beam axis, shown in Figure 2.4. In the transition and end-cap regions, the chambers are installed in three planes perpendicular to the beam axis.

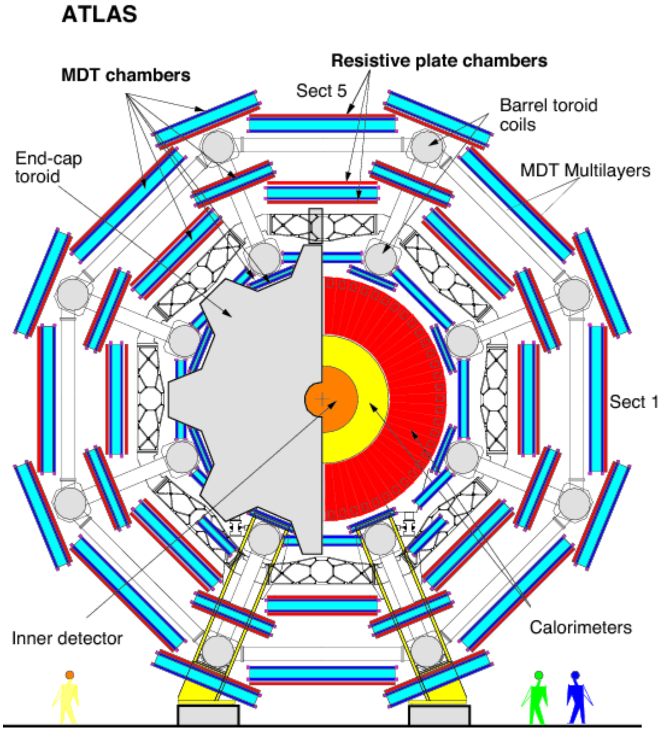

Figure 2.4: A schematic view of the muon spectrometer in the xy projection [47].

Two different types of muon chambers are used for the position measurement: the Monitored Drift Tube chambers (MDTs) and the Cathode Strip Chambers (CSCs). The MDTs provide a precision measurement of the muon tracks and they are used in most of the detector regions within $|\eta| < 2.7$. The CSCs with higher granularity are used in the forward regions ($2.0 < |\eta| < 2.7$).

The fast muon chambers are used for triggering and deliver the signal within 15-25 ns after the passage of the particle. For this purpose, the Resistive Plate Chambers (RPCs) are used in the barrel region while in the forward region the trigger information is provided by the Thin Gap Chambers (TGCs). The TGCs also measure the muon coordinate in the direction orthogonal to the precision-tracking chambers. The expected resolution of the muon spectrometer at $p_{\mathrm{T}} = 1$ TeV is

$$\frac{\sigma_{p_{\mathrm{T}}}}{p_{\mathrm{T}}} = 10\%. \tag{2.4}$$

2.2.4 Trigger system

In general, the trigger system is an essential component of any collider experiment, since it decides whether or not to keep an event from a given bunch-crossing interaction for later study. The ATLAS trigger system is responsible for selecting events of interest at the recording rate of approximately 1 kHz up to 40 MHz of collisions.

Between the LHC's Run 1 and Run 2 operations, the trigger needed an upgrade due to the increased centre-of-mass energy, higher luminosity and increased pileup expected in Run 2. Otherwise, if the trigger thresholds sufficient for the physics programme of Run 1 were used during Run 2, the trigger rates would have exceeded the maximum allowed rates. The Trigger and Data Acquisition (TDAQ) system used during Run 1 is described in detail in Reference [48], while here we briefly present the TDAQ system used in Run 2 [49].

The TDAQ system consists of the hardware-based first-level trigger (L1) and the software-based high-level trigger (HLT). The L1 trigger decision is formed by the Central Trigger Processor, which receives inputs from the L1 calorimeter, the L1Muon triggers and several other subsystems such as the Minimum Bias Trigger Scintillators (MBTS). After the L1 trigger acceptance, the events are buffered in the read-out system (ROS) and processed by the HLT. After the events are accepted by the HLT, they are transferred to a local storage at the experimental site and exported to the Tier-0 facility at CERN computing centre for offline reconstruction.

3. The Tile Calorimeter

The TileCal provides the crucial input for the measurement of jet energies and for the reconstruction of the missing transverse momentum. It is built from plastic scintillator tiles regularly spaced between low-carbon steel absorber plates, which surround the electromagnetic calorimeter. Usually, the thickness of the scintillator is 3 mm and the periodic structure is repeated every 18 mm along the beam axis as shown in Figure 3.1. Detailed description of the TileCal is provided in the dedicated Technical Design Report [23]; the construction, optical instrumentation and installation into the ATLAS detector are described in References [50, 51].

The calorimeter is divided into three parts: the central (long) barrel (LB) covering the region of $|\eta| < 1.0$, 5.8 m long and two extended barrels (EBs) in the region $0.8 < |\eta| < 1.7$, each 2.6 m long. Full azimuthal coverage around the beam axis is achieved with 64 modules, each covering $\Delta\phi = 0.1$ radians. Each module is segmented radially and in pseudorapidity.

3.1 Readout system

A particle traversing the detector generates light in the scintillators, which is collected on both sides of the tile and further transported to the photomultiplier tubes (PMTs) by wavelength shifting (WLS) fibres [51], see Figure 3.1. The read-out cell geometry is given by a group of WLS fibres from individual tiles coupled to PMTs, shown in Figure 3.2. Usually, a cell is read out by two PMTs, with each corresponding to a single channel. The cell energy is then reconstructed as the sum of energies measured by two channels. The radial segmentation divides the module into three parts, called layers. These layers comprise of cells with different dimensions. In the first two layers from the beam line, called A and BC (or just layer B in the EB), the dimensions of the cells are $\Delta\eta \times \Delta\phi = 0.1 \times 0.1$. In the outermost D layer the segmentation is $\Delta\eta \times \Delta\phi = 0.2 \times 0.1$.

For the reconstruction of the detected electrical signal, first, the signal from each PMT is shaped so that all pulses have the same width (full width at the half maximum, FWHM, is 50 ns). Thus the amount of energy deposited by a traversing particle in the cell is proportional to the height (amplitude) of the analogue pulse in the corresponding channel. Afterwards, the shaped signal is amplified in two separate gains, the high and the low gain, with the gain ratio of 64:1. Signals from both gains are sampled and digitised every 25 ns by 10-bit ADCs [52] resulting in a pulse represented by seven samples. By default, the high gain signal is used; however, if one of the seven samples saturates the ADC, then the low gain signal is sent. The sampled data are then temporarily stored in a pipeline memory waiting for the L1 trigger decision. After the positive trigger decision, all samples from one gain of each channel are read out and sent via optical fibres to the back-end electronics, located outside of the experimental hall.

The PMTs and front-end electronics are housed in the outermost part of each module, see Figure 3.1. Thus they can be fully extracted while leaving the remaining parts of the module in place.

A set of the so-called ITC cells is located between the LB and EB, namely D4, C10 and E-cells, which cover the pseudorapidity region of $0.8 < |\eta| < 1.6$. The

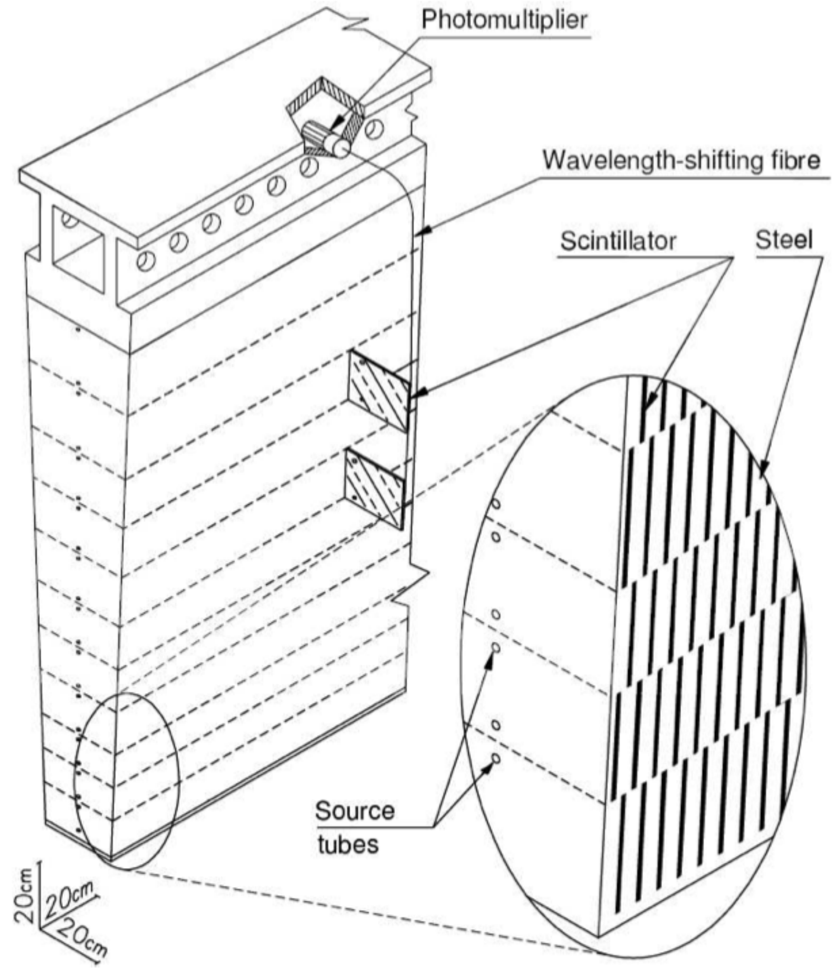

Figure 3.1: A sketch of a single Tile Calorimeter module [43].

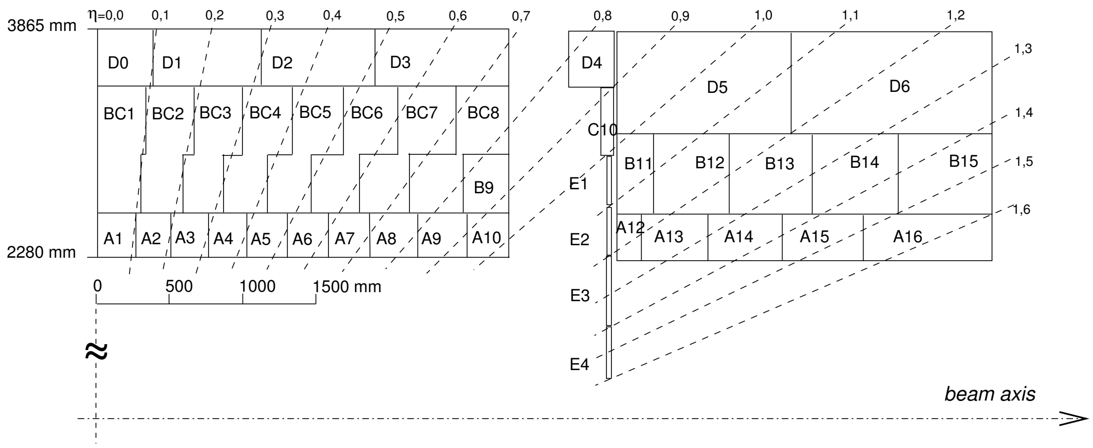

Figure 3.2: The layout of Tile Calorimeter cells, each denoted by a letter (A to E, with A-layer being closest to the beam pipe) and an integer. The naming convention is repeated on each side of $\eta = 0$ [43].

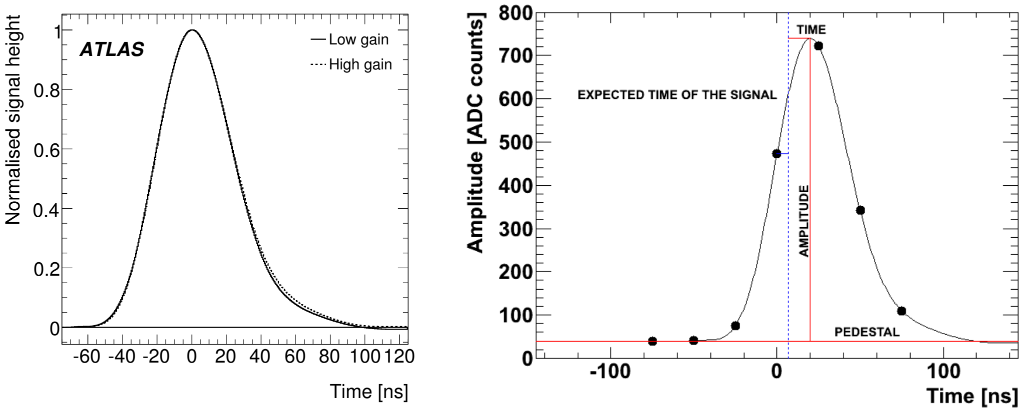

Figure 3.3: Left: Reference pulse shapes for high gain and low gain, shown in arbitrary units [53]. Right: An example of the reconstructed signal pulse with the non-zero time phase TIME (in the text labelled as τ).

gap (E1-E2) and crack (E3-E4) cells consist of one special scintillator and are read out by a single PMT. To trigger on events from colliding particles 16 MBTS are used.

3.2 Signal reconstruction

The signal pulse amplitude, time and pedestal for each channel are reconstructed using the Optimal Filtering (OF) technique [54]. The OF algorithm weights the measured samples in accordance with the reference pulse shape, which is shown in the left plot in Figure 3.3. The signal amplitude A and the time phase τ are calculated from the ADC count of each sample S_i obtained at the time t_i

$$A = \sum_{i=1}^{7} a_i S_i, \qquad A\tau = \sum_{i=1}^{7} b_i S_i, \tag{3.1}$$

where a_i and b_i are the weights derived to minimise the resolution of the amplitude and time.

Let us consider particles originating from collisions at the IP and traversing the detector at the speed of light. Then, the expected time of the reconstructed pulse peak is calibrated in such a way that the pulse peaks at the central sample. By definition, the central sample is at 0 ns. The value of τ represents the time phase in ns between the central sample (expected pulse peak) and the time of the actual reconstructed signal peak. An example of the reconstructed signal pulse with a non-zero time phase is shown in the right plot in Figure 3.3.

3.3 Channel time calibration and monitoring

To ensure the correct reconstruction of a signal pulse, we perform a channel time calibration [55], which is necessary because of the fluctuations in particle travel time, channel-to-channel differences in signal propagation time and uncertainties in the electronics read-out. Moreover, it is also essential for object selection and

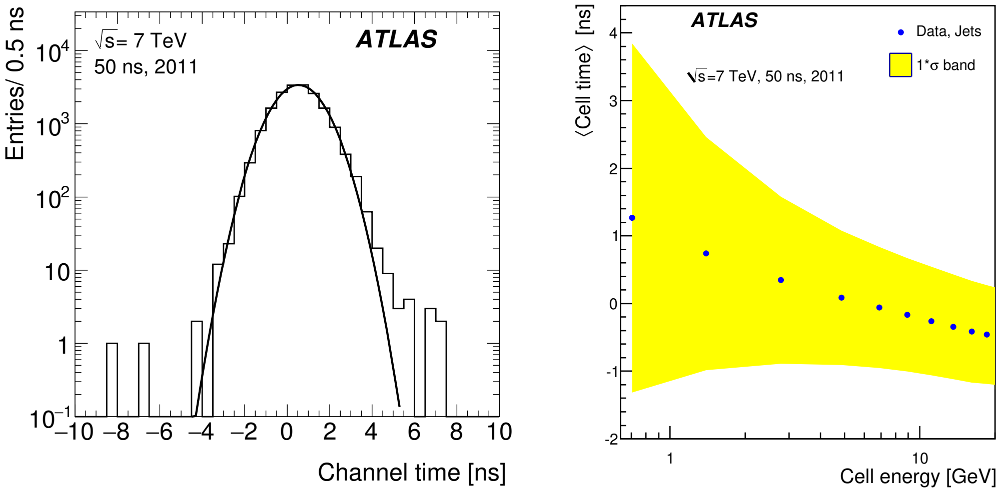

Figure 3.4: Left: An example of channel reconstructed time in jet events in 2011 data, with the channel energy between 2 and 4 GeV. Right: Mean cell reconstructed time (average of the times in the two channels associated with a given cell) as a function of the cell energy measured with jet events. The mean cell time decreases with the increase of cell energy because the energy fraction of the slow hadronic component of hadronic showers is reduced [55].

for time-of-flight analyses searching for hypothetical long-lived particles entering the calorimeter. An incorrect time calibration and consequently incorrect signal reconstruction may lead to an inaccurate energy reconstruction.

Each year, after the winter LHC shutdown and before the actual physics data taking, we perform the time calibration. We also monitor the time stability during the data taking, since for some channels, a sudden change in time settings might occur.

3.3.1 Time calibration

At this point, let us consider a situation before the time calibration. If we consider only a single reconstructed signal pulse of a single channel, the reconstructed time corresponds to the time phase τ of the reconstructed pulse peak. For several signal pulses, the reconstructed time in one channel follows Gaussian distribution with the mean corresponding to the time calibration constant, shown in the left plot in Figure 3.4. During the signal reconstruction, the time calibration constant is used as a correction in such a way that after the calibration, the mean channel time peaks at zero. Time calibration constants are saved in a database and applied as a correction in the offline data reconstruction.

The time calibration consists of two steps carried out in a sequence. First, the channel time calibration is performed with a laser system, which sends laser light directly to each PMT. This accounts for time delays caused by the different physical location of electronics. Then in the second step, we use collision data for the time calibration, considering in one event only channels belonging to the reconstructed jet.

The right plot in Figure 3.4 shows the dependence of the reconstructed time on

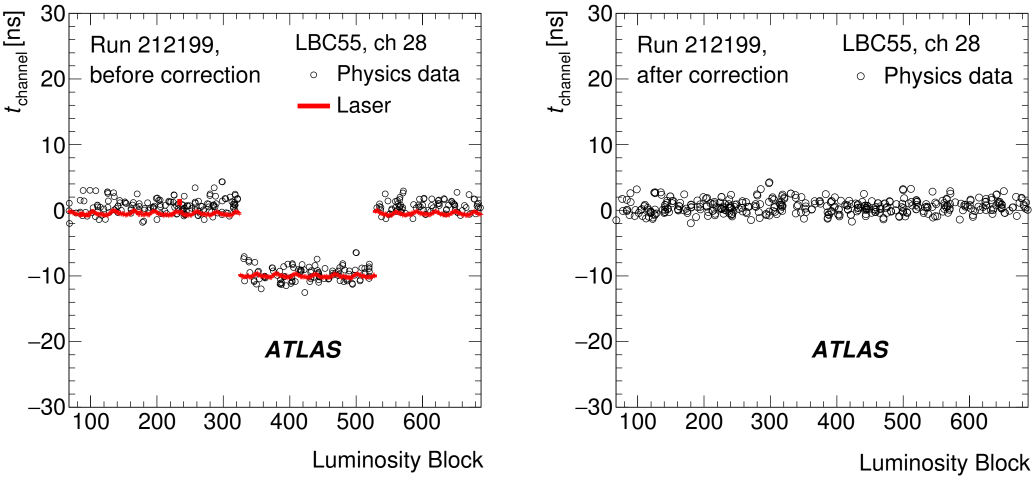

Figure 3.5: Left: An example of timing jumps detected using the laser (full red circles) and physics (open black circles) events before (left) and after (right) the correction. The small offset of about 2 ns in collision data is caused by the energy dependence of the reconstructed time in jet events. In these plots, events with arbitrary energies are accepted to accumulate enough statistics [55].

the energy deposited by a jet in a cell. A small fraction of events at the high-time tail of the distribution is mostly caused by the slow hadronic component of the shower development [56, 57] and these events are more evident for low energy bins. Symmetric high and low-time tails are caused by the out-of-time pileup. In order to avoid these tails, while still having a reasonable amount of data, we require the channel energy between 2 and 4 GeV for the time calibration. An example in the left plot in Figure 3.4 satisfies this condition.

The first step might be improved by using beam-splash events from a single LHC beam [53], during which a proton beam interacts with a closed collimator placed approximately 140 m before the nominal IP. However, we did not use beam-splash events for the time calibration in the years 2015 and 2016.

3.3.2 Time stability monitoring

The time stability monitoring during the data taking is necessary, because of a problem called ‘timing jump’. The timing jump happens when a set of six channels corresponding to one digitizer suddenly loses the time calibration settings and the reconstructed time phase of affected channels is not close to zero anymore. This always happens for all six channels of one digitizer and their observed time shift magnitude is always the same. An example of a timing jump is shown in the left plot in Figure 3.5. Althought the cause of the timing jumps was traced back to the TTCRx chip in the digitizer board, we are not able to prevent them.

Timing jumps might occur during the run (usually after a module reconfiguration) as well as at the beginning of the run. Sometimes, they recover themselves during the run and thus last only for several luminosity blocks (LBs), but they might be present during the whole run as well.

During the data taking, we monitor the time stability using both laser and collision events. Laser events are recorded in the empty bunch crossings and are later checked by the software for each channel and LB. Since the reconstructed time phase is expected to be close to zero, the monitoring algorithm looks for the shifts greater than 3 ns.

To verify timing jumps detected by the laser, or to identify them in the case when the laser is not operational, we use reconstructed jets from collision data. An example of the same timing jump, which shows a good agreement between laser events and jet collision data is shown in Figure 3.6.

Once a case is classified as a timing jump, the values of timing shifts for each channel and LB are saved in a database and are subsequently applied as a correction in the offline data reconstruction. The right plot in Figure 3.5 shows an example of a timing jump after the correction using laser and jet events. The same physics run with jet collision data before and after the time correction is applied, is shown in the left and right plot in Figure 3.7, respectively.

The correction to time constants can be applied during the so-called 'calibration loop' before the data are processed for the physics analyses. However, if we do not correct a time constant during the calibration loop, we provide the correct time constants for the data reprocessing at the end of each year.

In the years 2015 and 2016, I participated in the TileCal time calibration expert team, which is responsible for the time calibration and the time stability monitoring. In particular, we prepared the time calibration constants each year before the data taking and verified them. Furthermore, we monitored the time stability during the data taking and corrected the time calibration constants in case timing jumps were present. We also prepared the time calibration constant for the data reprocessing at the end of each year. These constants included the corrections for timing jumps which were not corrected during the calibration loop.

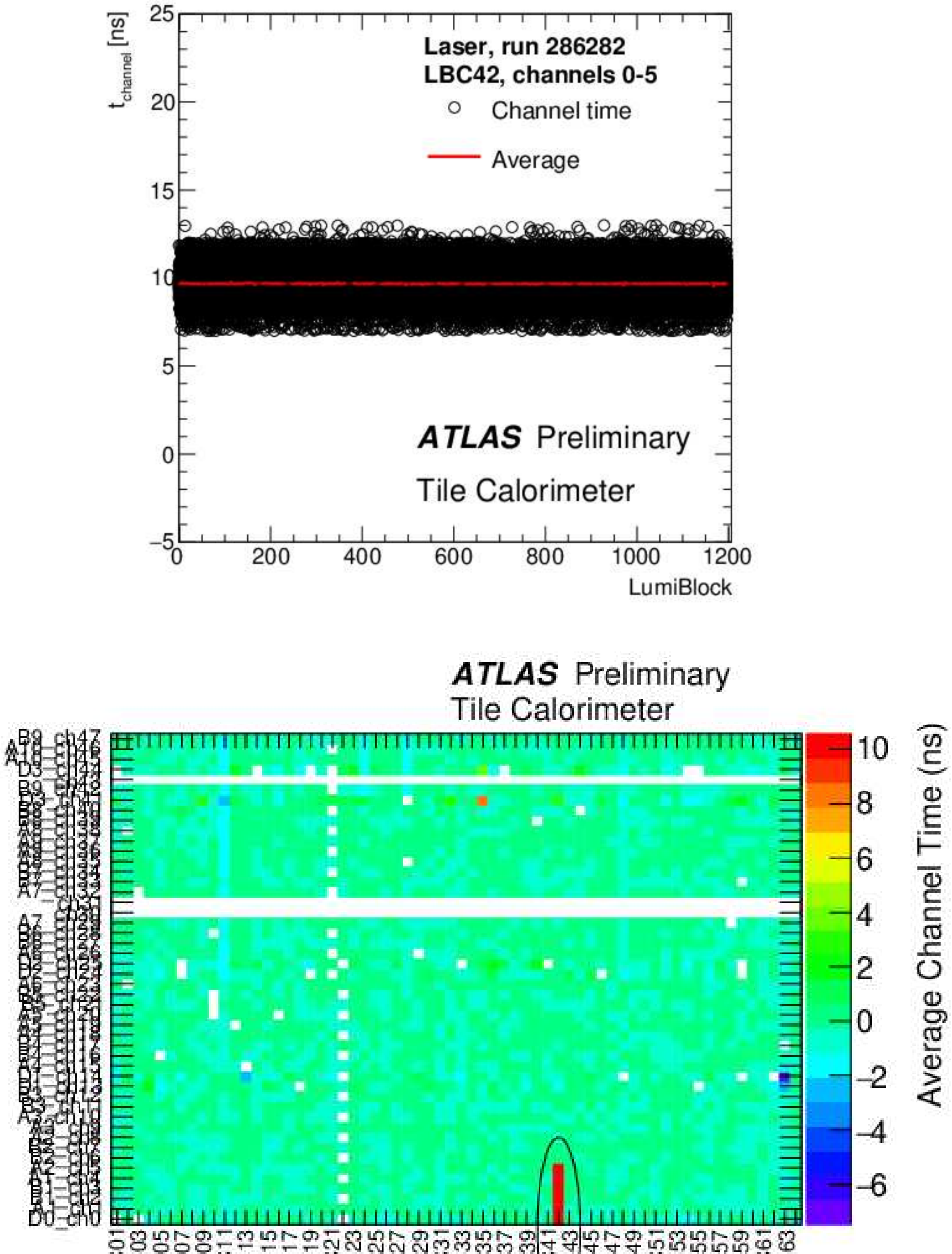

Figure 3.6: The reconstructed time in Tile Calorimeter channels is monitored during the physics runs with the laser calibration system (top) and with jet collision data (bottom). The sudden shifts are simultaneously detected by both monitoring systems. The plots show an example of a timing shift by ≈ 10 ns in a group of six channels of the LBC42 module. These results are available during the calibration loop and allow for time constants correction before the data are processed for physics analyses [58].

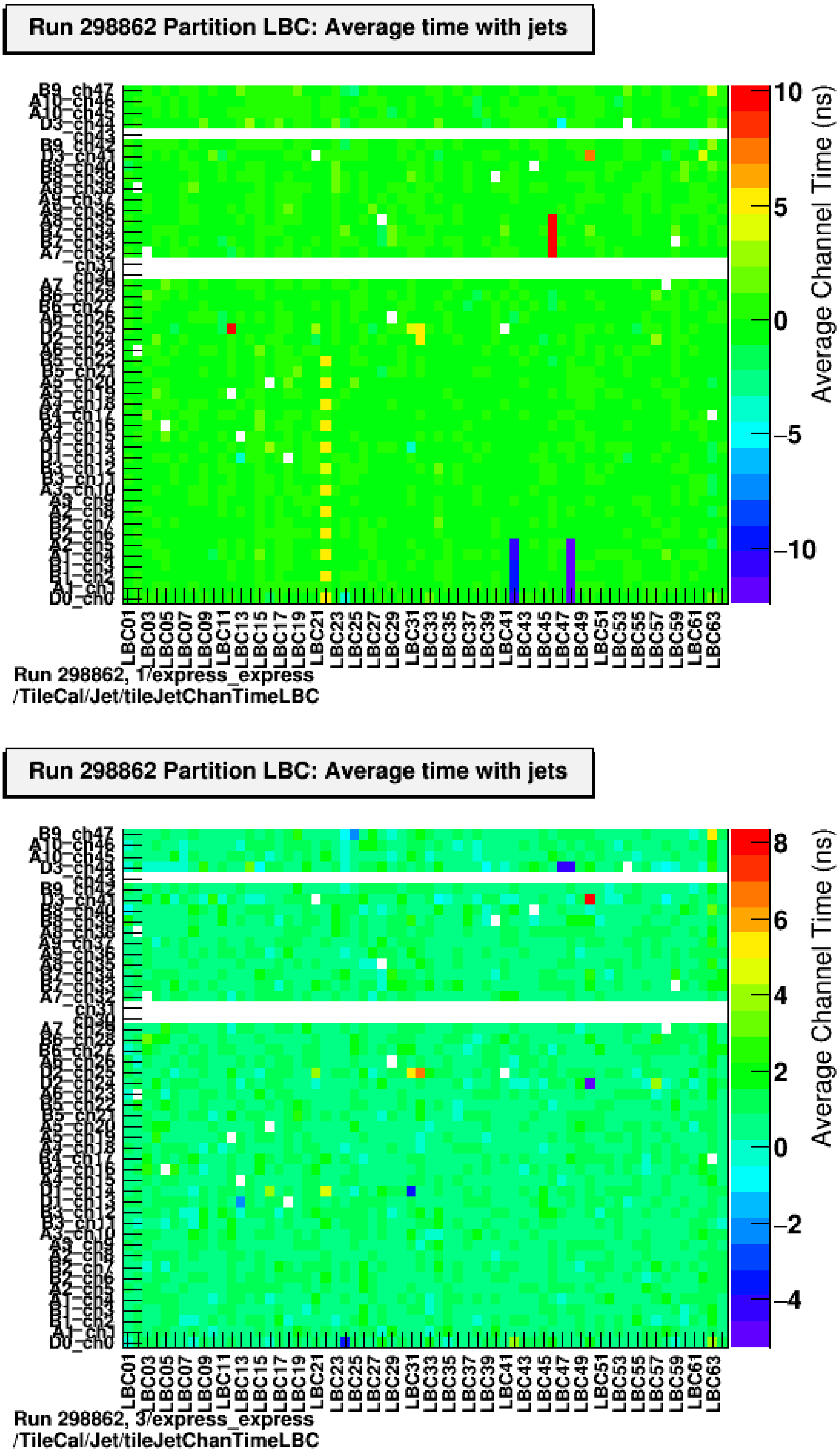

Figure 3.7: The reconstructed time in Tile Calorimeter channels is monitored during the physics runs with jet collision data. The plot shows the reconstructed time before (top) and after (bottom) the time constant correction is applied.

4. Statistical data analysis in high energy physics

4.1 Review of probability

First, we define probability in terms of set theory as formulated by Kolmogorov [59, 60]. Let us consider a set S called sample space, which contains subsets $A, B \subset S$. We can define the probability P as a real-valued function with the following properties:

1. For every subset $A \subset S$, $P(A) \geq 0$.
2. The probability assigned to the sample space is one, $P(S) = 1$.
3. If $A \cap B = \emptyset$, then $P(A \cup B) = P(A) + P(B)$.

If we consider the subsets $A, B \subset S$, such that $P(B) \neq 0$, we can define the conditional probability of A given B as

$$P(A|B) = \frac{P(A \cap B)}{P(B)}. \tag{4.1}$$

Since $A \cap B$ is the same as $B \cap A$ we can write

$$P(A \cap B) = P(A|B)P(B) = P(B|A)P(A), \tag{4.2}$$

from which follows

$$P(A|B) = \frac{P(B|A)P(A)}{P(B)}. \tag{4.3}$$

Equation (4.3) is called Bayes' theorem, which relates two conditional probabilities $P(A|B)$ and $P(B|A)$.

4.1.1 Interpretation of probability

Any function that satisfies the aforementioned axioms can represent the probability. However, one must specify the interpretation of probability values and the elements of the sample space. In data analyses, two interpretations of probability are mainly used: relative frequency and subjective probability.

Probability as a relative frequency

In particle physics, probability is most commonly interpreted as a limiting relative frequency. In this interpretation, the elements of a sample space S represent the possible outcomes of a repeatable measurement. We can define a subset $A \subset S$, such that $P(A)$ represents the fraction of times the outcome occurs in the subset A assuming that we repeat the measurement n times under the same conditions

$$P(A) = \lim_{n \to \infty} \frac{\#\text{ outcome is in } A}{n}. \tag{4.4}$$

Using the probability in repeatable measurements leads to so-called frequentist approach to statistics. Nevertheless, we can never determine experimentally the probabilities based on such a model with perfect precision, as it is not possible to repeat the measurement infinite number of times. The aim of classical statistics is to estimate the probabilities by using a finite amount of experimental data and to study their agreement with predictions based on a particular model.

Subjective probability

We can define the subjective probability by interpreting the elements of a sample space S as hypotheses or propositions, i.e. statements which are either true or false. Then, the probability is interpreted as a measure of degree of belief in a given theory or hypothesis

$$P(A) = \text{degree of belief that the hypothesis } A \text{ is true.} \tag{4.5}$$

In addition, we require the sample space to contain only the hypotheses which are mutually exclusive, i.e. only one of them is true. Use of subjective probability leads to Bayesian statistics.

If we consider the subset $A \subset S$, from Equation (4.3) to be the hypothesis that a certain theory is true and the subset $B \subset S$, to be the hypothesis that the experiment will yield a particular result (outcome of the experiment = data), then Bayes' theorem gets the following form

$$P(\text{theory}|\text{data}) \propto P(\text{data}|\text{theory})P(\text{theory}), \tag{4.6}$$

where $P(\text{data}|\text{theory})$ is the probability to measure the data actually obtained, given the theory (in the frequentist approach it is called the likelihood). $P(\text{theory})$ is the prior probability that a theory is true and it reflects the experimenter's degree of belief before carrying out the measurement. However, Bayesian statistics provides no fundamental rule for obtaining the prior probability, which in general, is subjective and may depend on previous measurements or theories. Once we specify the prior probability, we can get a posterior probability.

4.2 Statistics for particle physics

In this section, we present the strategies used in high-energy physics for developing a statistical model of data. The text is based on the following References [61, 62, 63, 64, 65, 66].

4.2.1 Probability densities and the likelihood function

Let us imagine a search for the Higgs boson, where we consider a contribution from a single channel labelled c. Different channels do not correspond to underlying physics processes, but rather to the disjoint regions of data defined by associated event selection criteria. Each channel may provide the number of selected events n_c, as well as some other measured quantity (observable) x_c, e.g. the invariant mass of the Higgs boson candidate. One should bear in mind that the observable x is frequentist in nature, thus by repeating an experiment many times, we measure different values of x, which give rise to a probability density function (pdf) of $f(x)$ for which holds

$$\int f(x)dx = 1.$$

A parametric family of pdfs, $f(x|\alpha)$, is often considered and in the following is referred to as the probability model. Parameters α usually represent parameters of a physics theory or a property of detector's response. These parameters are not frequentist in nature and thus any probability statement associated with them is Bayesian. However, we are usually interested only in one or a few parameters from the whole set called parameters of interest (POIs), while the remaining parameters are called nuisance parameters (NPs). Note that we must account for the NPs in the probability model, even though we have no particular interest in them.

The function $f(x)$ describes the probability density of the observable x for a single event. A more general case is to consider the dataset with many events $\mathcal{D} = \{x_1, \ldots, x_n\}$. Assuming that the individual events x_i follow the same underlying distribution, the probability density for the dataset $\mathcal{D}$ can be written as a product of probability densities for each event. Additionally, if we know the total number of expected events, we should include the overall Poisson probability for observing n events given ν events expected

$$\boldsymbol{f}(\mathcal{D}|\nu, \alpha) = \mathrm{Pois}(n|\nu) \prod_{e=1}^{n} f(x_e|\alpha), \tag{4.7}$$

where the bold $\boldsymbol{f}$ is used to distinguish the probability density function for the dataset $\mathcal{D}$ from an individual event probability density function $f(x)$, and e is the index running over events. The expected number of events may be parametrised as well, and these parameters can modify the expected rate and shape of the distribution, thus we write $\nu \to \nu(\alpha)$.

Further, we can define a likelihood function $L(\alpha)$ equivalent to $f(x|\alpha)$ or $\boldsymbol{f}(\mathcal{D}|\alpha)$ with fixed x or $\mathcal{D}$, respectively. We should remember that the likelihood function cannot be interpreted as a probability density for α, since it is not normalised.

To summarise, the probability density function refers to a value of f as a function of x given a fixed value of α, while the likelihood function refers to a value of f as a function of α given a fixed value of x and the probability model refers to the whole structure of $f(x|\alpha)$.

So far, we have considered the probability model for the Higgs boson search with only one channel. However, usually we have to combine several analysis channels in order to obtain statistically significant results. The combined (or simultaneous) model, which simultaneously describes several channels, can be constructed as

$$\boldsymbol{f}_{\mathrm{sim}}(\mathcal{D}_{\mathrm{sim}}|\alpha) = \prod_{c \in \mathrm{channels}} \left[\mathrm{Pois}(n_c|\nu_c(\alpha)) \prod_{e=1}^{n_c} f_c(x_{ce}|\alpha) \right], \tag{4.8}$$

where e is the index running over events, n_c is the number of events in the c^{th} channel, and x_{ce} is the value of the e^{th} event in the c^{th} channel.

A sketch of a typical particle physics probability model and dataset structure is shown in Figure 4.1.

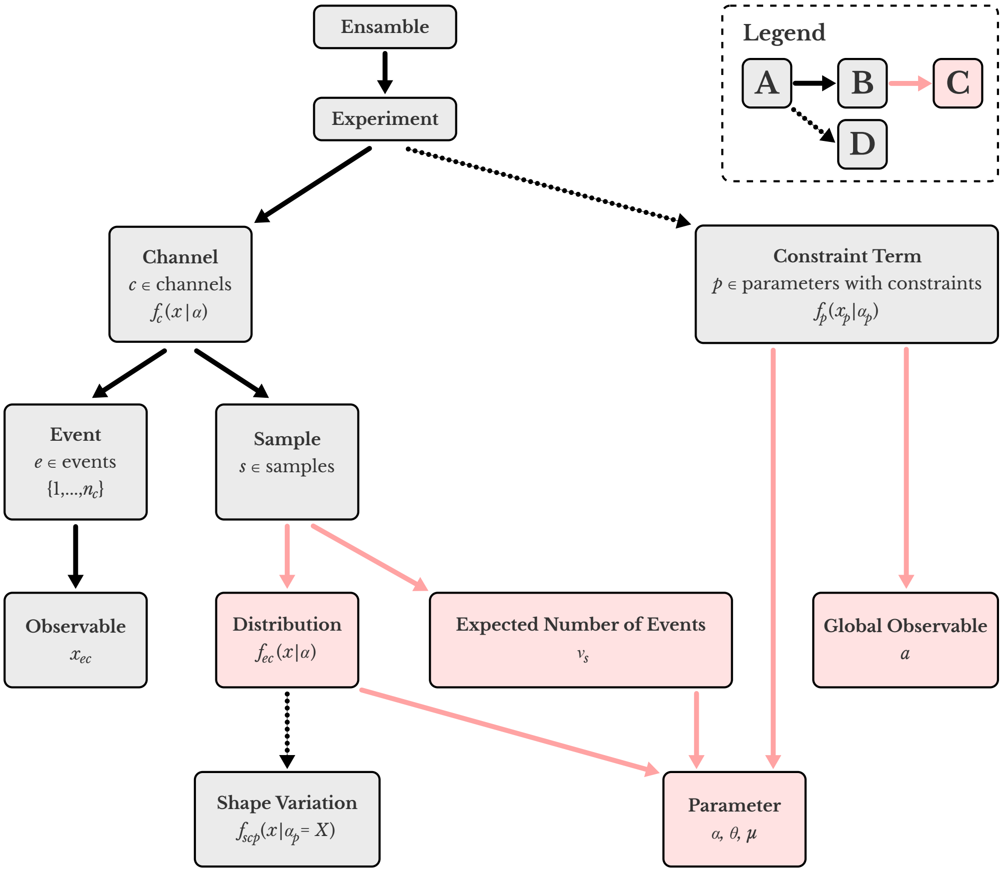

Figure 4.1: A schematic diagram of the logical structure of a typical particle physics probability model and dataset structure. The solid black line corresponds to the case when the set A has many subsets B. The solid red line corresponds to the case when the set B has a single subset C. The dashed line indicates that subsets D are optional [65].

4.2.2 Auxiliary measurements

To estimate or reduce the effect of systematic uncertainties, auxiliary measurements or control regions can be used. The control region and signal region are not fundamentally different, they can be considered just as two different channels in Equation (4.8).

We demonstrate the use of control region on an example of a simple counting experiment with an unknown signal ν_{S} and background ν_{B} contributions. The expected number of events in the signal region is n_{SR} and we can write down the model as $\mathrm{Pois}(n_{\mathrm{SR}}|\nu_{\mathrm{S}} + \nu_{\mathrm{B}})$, where we consider the unknown background contribution in the signal region to be an NP.

To get an estimate of the background contributions, we often use a control region or a control sample. It is chosen in such a way that it is populated by the same background processes as the signal region; however, it does not contain signal events. If we have a control region with n_{CR} events, we can write $\mathrm{Pois}(n_{\mathrm{CR}}|\tau\nu_{\mathrm{B}})$, where τ is a factor which extrapolates the background contribution from the signal region to the control region. Hence, the simultaneous probability model which describes both regions is

$$\boldsymbol{f}_{\text{sim}}(n_{\text{SR}}, n_{\text{CR}}|\nu_{\text{S}}, \nu_{\text{B}}) = \text{Pois}(n_{\text{SR}}|\nu_{\text{S}} + \nu_{\text{B}}) \cdot \text{Pois}(n_{\text{CR}}|\tau\nu_{\text{B}}).$$

This statistical model can be treated in the frequentist formalism. This means that if we repeat the experiment many times, both n_{CR} and estimate of ν_{B} will vary. If we consider only the control region, we would get an estimate $\nu_{\text{B}} = n_{\text{CR}}/\tau$ with an uncertainty of $\sqrt{n_{\text{CR}}}/\tau$. Auxiliary measurements or control regions can be utilised to statistically describe the uncertainty on the NP ν_{B} – we say that they 'constrain' the NPs.

Modelling of constraint terms

Usually, the statistical model does not include a detailed probability model for auxiliary measurements. More often, it includes an estimate, a 'central value', or the best guess for a parameter and its uncertainty for background and systematic uncertainties. A parameter α_p has an estimate a_p, which is included in the likelihood function as the constraint term $f(a_p|\alpha_p)$.

One should keep in mind that not all considered uncertainties come from auxiliary measurements. In particular, some theoretical uncertainties such as those associated with the choice of renormalisation and factorisation scales in theoretical calculations, are not statistical in nature and they always rely on a prior. In a Bayesian setting, we can include a prior on the parameters associated with theoretical uncertainties without any problems, but in a frequentist setting, we should not incorporate constraint terms on theoretical uncertainties that lack the frequentist interpretation. However, one can undo the Bayesian reasoning into an objective pdf or likelihood function and a prior, and write a model which can be used in the frequentist context

$$\pi(\alpha_p|a_p) \propto L(\alpha_p)\eta(\alpha_p) = f(a_p|\alpha_p)\eta(\alpha_p), \tag{4.9}$$

where $\pi(\alpha_p|a_p)$ is a Bayesian pdf with a prior $\pi(\alpha_p)$ based on some estimate a_p. The prior $\pi(\alpha_p)$ is actually a posterior from some previous measurement and $\eta(\alpha_p)$ is some more fundamental prior.

We can include the constraint terms explicitly in the model and get the total probability model

$$\boldsymbol{f}_{\text{tot}}(\mathcal{D}_{\text{sim}}, \mathcal{G}|\alpha) = \prod_{c \in \text{channels}} \left[\text{Pois}(n_c|\nu_c(\alpha)) \prod_{e=1}^{n_c} f_c(x_{ce}|\alpha) \right] \cdot \prod_{p \in \mathbb{C}} f_p(a_p|\alpha_p), \tag{4.10}$$

where e is the index running over events, n_c is the number of events in the c^{th} channel, and x_{ce} is the value of the e^{th} event in the c^{th} channel, $\mathbb{C}$ is a set of parameters with constraint terms and $\mathcal{G} = \{a_p\}$ are the global observables (with $p \in \mathbb{C}$).

4.2.3 Parameter estimation

Very often, scientists want to estimate parameters of some model. To make an estimate of the true value of the parameter α, we use an estimator $\hat{\alpha}(\mathcal{D})$, which is a function of data. The maximum likelihood estimator (MLE) is commonly used by experimental particle physicists. It is defined as the value $\hat{\alpha}$ that maximises the likelihood function $L(\alpha)$. Similarly, $\hat{\alpha}$ maximises $\ln L(\alpha)$ and thus minimises $-\ln L(\alpha)$, also referred to as the negative-log likelihood (NLL). In physics jargon, we 'fit' the likelihood function and the maximum likelihood estimate corresponds to 'the best fit value'.

Usually, we have a multi-parameter likelihood function $L(\mu, \boldsymbol{\theta})$, where μ is the POI, e.g. the signal strength and $\boldsymbol{\theta}$ are the NPs. The MLEs, $\hat{\mu}$ and $\hat{\boldsymbol{\theta}}$, are the values of the parameters μ and $\boldsymbol{\theta}$ which maximise the likelihood function. If all parameters are let free-floating during the fit, $\hat{\mu}$ and $\hat{\boldsymbol{\theta}}$ are called unconditional maximum likelihood estimates.

However, we might fix some of the parameters and ask about the estimate of the remaining NPs. A very common case is that we want to obtain the estimates of NPs for a fixed value of μ. Then, we get the conditional maximum likelihood estimates $\hat{\hat{\boldsymbol{\theta}}}(\mu)$ of $\boldsymbol{\theta}$, which maximise the likelihood function for a fixed μ. This procedure of choosing the specific values of the NPs for a given value of μ, $\mathcal{D}_{\text{sim}}$ and $\mathcal{G}$ is often called 'profiling' and $\hat{\hat{\boldsymbol{\theta}}}(\mu)$ is 'the profiled value of $\boldsymbol{\theta}$'.

4.2.4 Example: Fitting a straight line

This example is taken from [62] and it demonstrates how including a single NP with or without a prior measurement affects the fit results.

Let us consider independent data values y_i, $i = 1, \ldots, n$, each made at a given value x_i of a control variable x, as shown in Figure 4.2 (a). We assume that the measured values follow a Gaussian distribution with standard deviations σ_i and mean values μ_i. The data can be described by a function

$$\mu(x; \theta_0, \theta_1) = \theta_0 + \theta_1 x, \tag{4.11}$$

and we are interested in determining the value of the parameter θ_0, which makes it our POI. In order to achieve a good description of data, we have to include the slope parameter θ_1 in the fit model, even though we are not particularly interested in its value. If we do not know the value of the parameter θ_1, it is considered to be an NP of the model.

The probability density function for the i^{th} measurement y is

$$f(y_i, \theta) = \frac{1}{\sqrt{2\pi}\sigma_i} \exp\left[-\frac{(y_i - \mu(x_i, \theta))^2}{2\sigma_i^2}\right]. \tag{4.12}$$

For independent measurements, the likelihood function is then given by a product of pdfs for each measurement

$$L(\theta) = \prod_{i=1}^{n} f(y_i, \theta). \tag{4.13}$$

In the frequentist approach, estimators $\hat{\theta}$ of the NPs correspond to the values that maximise the likelihood function. In this example, it is equivalent to minimising the quantity

$$\chi^2(\theta) = \sum_{i=1}^{n} \frac{(y_i - \mu(x_i, \theta))^2}{\sigma_i^2} = -2 \ln L(\theta) + C, \tag{4.14}$$

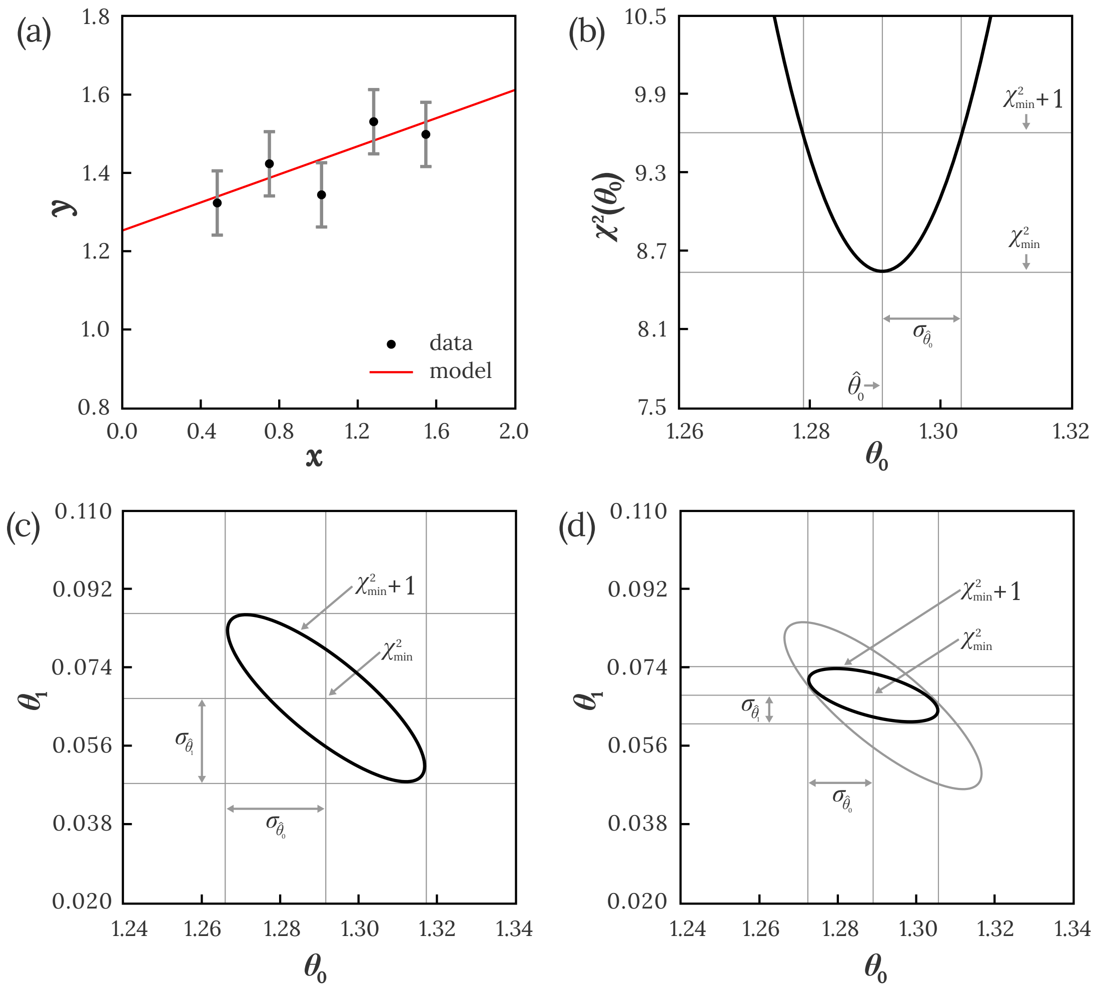

Figure 4.2: An example of (a) fitting a straight line to data; (b) χ^2 as a function of the parameter θ_0, illustrating the method to determine the estimator $\hat{\theta}_0$ and its standard deviation $\sigma_{\hat{\theta}_0}$; contour of $\chi^2(\theta) = \chi^2_{min} + 1$ centred about the estimated $(\hat{\theta}_0, \hat{\theta}_1)$ (c) with no prior measurement of θ_1, (d) including the prior measurement of θ_1.

where C represents parameter-independent terms. As we can see, for independent Gaussian measurements, the MLE for parameters coincide with those of the method of least squares. Figure 4.2 (b) shows χ^2 as a function of the parameter θ_0.

We consider three different scenarios for the parameter θ_1:

1. We know exactly its value, then we hold it fixed.
2. We do not know its value and we have to treat the parameter it as an additional parameter in the fit.
3. We have its prior measurement.

In the first scenario, illustrated in Figures 4.2 (a),(b), we assume that we know the exact value of the slope parameter θ_1, so it is not used to maximise the likelihood, but held fixed. Standard deviations of estimators are the statistical errors of the measured values. Methods for obtaining the standard deviations of estimators are described in Reference [61]. For a single fitted parameter, the rule is to move the parameter away from the estimated value $\hat{\theta}_0$ until χ^2 increases by one unit (equivalently $\ln L$ decreases from its maximum by 1/2).

In the second scenario, illustrated in Figure 4.2 (c), we do not know the value of the parameter θ_1 and we are not particularly interested in its value so we treat it as an NP in the fit. By minimising $\chi^2(\boldsymbol{\theta})$, we obtain the estimators $\hat{\boldsymbol{\theta}} = (\hat{\theta}_0, \hat{\theta}_1)$. However, compared to the case with fixed parameter θ_1, the statistical errors cannot be obtained simply by moving the parameter away from its estimated value $\hat{\theta}_0$ until χ^2 increases by one unit, we need to find the standard deviations from the tangent lines (or hyperlines for higher-dimensional problems) to the contour defined by $\chi^2(\boldsymbol{\theta}) = \chi^2_{min} + 1$.

The third scenario, shown in Figure 4.2 (d), corresponds to the case with a prior measurement of θ_1. Let us consider a measurement t_1 that follows a Gaussian distribution with the centre at θ_1 and the standard deviation σ_{t_1} as an example. If the measurements of θ_1 and y_1 are independent, we obtain a full likelihood function by multiplying a term in Equation (4.14) by a Gaussian term

$$\chi^2(\theta) = \sum_{i=1}^{n} \frac{(y_i - \mu(x_i, \theta))^2}{\sigma_i^2} + \frac{(\theta_1 - t_1)^2}{\sigma_{t_1}^2}. \tag{4.15}$$

The tilt of the contour in Figure 4.2 (c) demonstrates the correlation between the estimators $\hat{\theta}_0$ and $\hat{\theta}_1$. We can find an estimate for the inverse of the covariance matrix $V_{ij} = \mathrm{cov}[V_i, V_j]$ from the second derivative of the log-likelihood evaluated at its maximum

$$\hat{V}_{ij}^{-1} = -\left.\frac{\partial^2 \ln L}{\partial\theta_i \partial\theta_j}\right|_{\theta=\hat{\theta}}. \tag{4.16}$$

More information about the extraction of the full covariance matrix from the contour can be found in Reference [61]. We should note that the correlation between the estimators for the POI and the NP results in inflating the standard deviations of both parameters. For this reason, we aim to keep fit parameters uncorrelated in the physics analysis.

By comparing the values $\sigma_{\hat{\theta}_0}$ in Figure 4.2 (b) and in Figure 4.2 (c), we see that the uncertainty is smaller in the case when the exact value of θ_1 is known compared to the one obtained in the scenario, where θ_1 is considered to be an NP. This means that by inclusion of an additional NP we improve the model's ability to describe the data; however, it comes at the price of increased statistical errors.

The black contour in Figure 4.2 (d) corresponds to the third scenario, while the grey contour to the second one. The black contour of $\chi^2 = \chi^2_{min} + 1$ is squeezed in the θ_1 direction with respect to the grey contour due to the measurement on θ_1. For the same reason, a decrease in uncertainty of θ_0 is also apparent. This example demonstrates that well chosen constraints of the NPs can improve the statistical accuracy of the POI measurement.

4.2.5 Building a probability model

Very often, histograms are used to estimate a pdf based on a sample of events generated by Monte Carlo (MC) simulations. Yet, it is important to remember the limitations of using histograms as an estimate for a distribution $f(x)$, particularly, their discontinuity and dependence on the location of bin boundaries.

In general, in order to build a statistical model of selected data, we need to include all expected signal and background processes contributions, data-driven background measurements and all systematic uncertainties.

For the sake of simplicity, we will consider a single POI[1] – the signal strength defined as $\mu = \sigma_{H\to\tau\tau}/\sigma^{\mathrm{SM}}_{H\to\tau\tau}$, where $\sigma^{\mathrm{SM}}_{H\to\tau\tau}$ stands for the SM prediction. Thus, $\mu = 0$ corresponds to the background-only model and $\mu = 1$ to the signal as predicted by the SM. Additionally, the model incorporates NPs $\boldsymbol{\theta}$ related to statistical and systematic uncertainties and to the normalisation of background processes contributions measured in control regions.

For given values of global observables $\mathcal{G}$, parameters $\boldsymbol{\alpha} = (\mu, \boldsymbol{\theta})$ and a dataset $\mathcal{D}_{\mathrm{sim}}$, we derive an associated likelihood function over μ and θ from the combined model over all channels including all constraint terms in Equation (4.10)

$$L(\mu, \boldsymbol{\theta}; \mathcal{D}_{\mathrm{sim}}, \mathcal{G}) = \boldsymbol{f}_{\mathrm{tot}}(\mathcal{D}_{\mathrm{sim}}, \mathcal{G}|\mu, \boldsymbol{\theta}). \tag{4.17}$$

The set of parameters $\boldsymbol{\theta}$ can be written as $\boldsymbol{\theta} = \{\alpha_p, \phi_p, \gamma_p\}$, with $p \in \mathbb{C}$ as defined in Equation 4.10, to demonstrate that it includes three sets of NPs:

- parameters related to systematic uncertainties $\mathbb{S} = \{\alpha_p\}$,
- normalisation factors $\mathbb{N} = \{\phi_p\}$ which are determined directly from the fit,
- statistical uncertainties $\boldsymbol{\Gamma} = \{\gamma_p\}$ of the expected number of events in each histogram bin.

Then we can write the final statistical model as

$$L(\mu, \alpha_p, \phi_p, \gamma_p) = \prod_{c\in\mathrm{channels}} \prod_{b\in\mathrm{bins}} \mathrm{Pois}(n_{cb}|\nu_{cb}) \cdot \mathrm{G}(L_0|\lambda, \Delta_L) \cdot \prod_{p\in\mathbb{S},\mathbb{N}} f_p(a_p|\theta_p), \tag{4.18}$$

where $\mathrm{Pois}(n_{cb}|\nu_{cb})$ is the Poisson probability of observing n_{cb} events in the bin b of the channel c given the expected number of events ν_{cb}. One should bear in mind that the expected number of events $\nu_{cb}(\mu, \alpha_p, \phi_p, \gamma_p)$ might depend on the fit parameters, as will be discussed in more detail later. In comparison with Equation (4.10), we do not consider each event separately, but rather the bin contents b of binned invariant mass distribution in the channel c. Additionally, we include the term $\mathrm{G}(L_0|\lambda, \Delta_L)$, which corresponds to the Gaussian probability of measuring the integrated luminosity L_0, given the true integrated luminosity λ and the measurement uncertainty Δ_L. The pdf $f_p(a_p|\theta_p)$ determines the constraint on the NPs α_p and γ_p. The constraint on the parameter α_p is based either on auxiliary measurements or theoretical calculations.

The choice of the pdf for the NPs depends on the type of the corresponding associated uncertainty. Following the recommendations of the LHC Higgs Combination Group, we use three different classes of pdfs to distinguish between the experimental and theoretical systematic uncertainties and the statistical uncertainties.

Experimental systematic uncertainties are modelled with Gaussian distributions

$$\mathrm{G}(a_p|\alpha_p, \sigma_p) = \frac{1}{\sqrt{2\pi\sigma_p^2}} \exp\left[-\frac{(a_p - \alpha_p)^2}{2\sigma_p^2}\right], \tag{4.19}$$

---

[1] In the $H \to \tau\tau$ analysis, we have provided fits with two and three POIs as well, more details in Section 5.6.

where a_p corresponds to the nominal value and σ_p to the uncertainty of the NP obtained from an auxiliary measurement. These values are usually applied during the nominal event reconstruction, while α_p is the true value of the NP relative to the nominal value a_p.

Theoretical systematic uncertainties usually assume only positive values (e.g. of the cross-section), thus they are modelled with log-normal distribution

$$P_{LN}(a_p|\alpha_p, k_p) = \frac{1}{\sqrt{2\pi}\ln k_p}\frac{1}{a_p}\exp\left[-\frac{\ln(a_p/\alpha_p)^2}{2(\ln k_p)^2}\right], \tag{4.20}$$

which is related to the Gaussian function through $k_p = \exp(\sigma_p)$.

Statistical uncertainties are modelled by gamma distributions, which are the continuous generalisation of the Poisson distribution. The corresponding Poisson distribution is given by

$$\mathrm{Pois}(n_p|\tau_p\gamma_p) = \frac{(\tau_p\gamma_p)^{n_p}e^{-\tau_p\gamma_p}}{n_p!}, \tag{4.21}$$

where the number of expected events is composed of the nominal event yield τ_p and the relative parameter γ_p.

For statistical description of the observed data, we use the maximum likelihood estimator, defined as a set of parameter values $(\hat{\mu}, \hat{\boldsymbol{\theta}})$ that maximise the likelihood function $L(\mu, \boldsymbol{\theta}) = L(\mu, \alpha_p, \phi_p, \gamma_p)$. This maximisation is performed with the `Minuit` programme [67] which minimises the value of $-\ln L(\mu, \boldsymbol{\theta})$.

Incorporating fit parameters into a model

During the statistical model preparation, we need to estimate the expected number of events. For this purpose, we might use either simulations or a data-driven approach. Usually, analyses utilise multiple of these approaches.

As mentioned earlier, the total number of events ν_{tot} depends on the parameters $\boldsymbol{\theta}$ and it can be expressed as

$$\nu_{\mathrm{tot}} = \lambda \times \sigma \times \epsilon \times A, \tag{4.22}$$

where

- λ is the time-integrated luminosity, which is an accelerator property
- σ is the cross-section predicted by a theory
- ϵ is the efficiency, which is the property of a detector
- A is the acceptance, which is the property of event selection criteria

To estimate the efficiency and acceptance we use MC simulations and usually generate a large sample of events.

The parameters $\boldsymbol{\theta}$ in Equation (4.17) can be related to the parameters that either appear in the Lagrangian of the theory, or originate from the MC simulations. In the case of the latter, we obtain the parameters for the parton shower, hadronisation, and detector simulation components. To model these parameters,

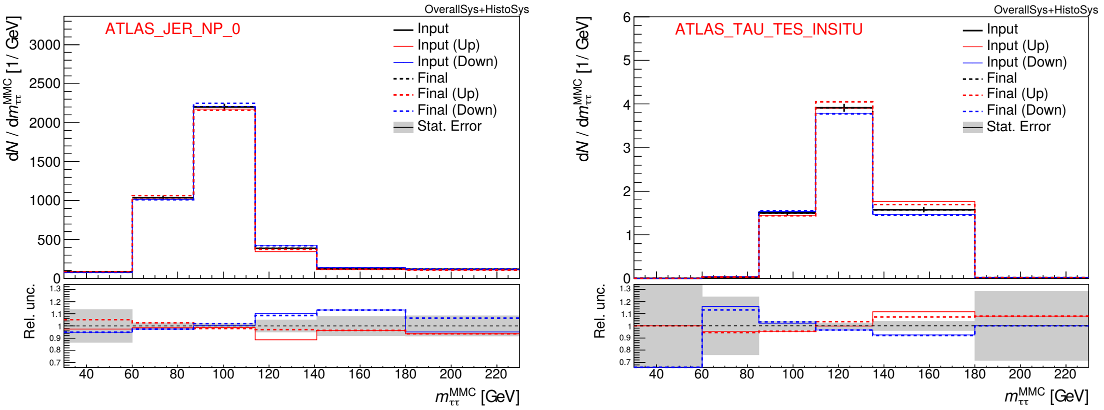

Figure 4.3: Examples of the input variations (solid lines) in distributions of the invariant mass of a pair of tau leptons $m_{\tau\tau}^{\text{MMC}}$ for one component of the jet energy resolution (JER) uncertainty (left) and the tau energy scale (TES) uncertainty (right) in the $H \to \tau\tau$ cross-section measurement.

we generate MC samples for several choices of $\boldsymbol{\theta}_i$ and then use some interpolation strategy to get a continuous parametrisation.

The changes in the distribution rates and shapes caused by parameters $\boldsymbol{\theta}$ result in systematic uncertainties and appear in the fit model as NPs. The impact of different sources of systematic uncertainties is expressed in terms of relative changes of the expected event yields and varying shapes of the discriminate variable. Usually, we have some nominal values for these parameters $\boldsymbol{\theta}^0$ and then vary each parameter 'upwards' and 'downwards' by $\theta_p^{\pm}$. These variations are obtained by varying a given experimental or theoretical quantity by adding or subtracting one standard deviation ($\pm 1\sigma$) around the nominal value. The nominal value, as well as the corresponding uncertainties, are usually obtained from auxiliary measurements. Figure 4.3 shows the examples of the input variations (solid lines) in distributions of the invariant mass of a pair of tau leptons $m_{\tau\tau}^{\text{MMC}}$ for one component of the jet energy resolution (JER) uncertainty (left) and the $\tau_{\text{had-vis}}$ energy scale (TES) uncertainty (right) in the $H \to \tau\tau$ cross-section measurement. The solid lines correspond to the output variations which are directly used by the fit. To obtain the output variations we use a specific treatment described in Section 5.6.

The statistical model built in this section was used for the $H \to \tau\tau$ cross-section measurement. The details are described in Section 5.6.

4.2.6 Discovery as hypothesis testing

In particle physics experiments, we often search for processes that have been predicted by the theory, but not yet observed. We can quantify the statistical significance of an observed signal by means of a p-value or its equivalent Gaussian significance, both defined below. It is also useful to characterise the sensitivity of an experiment by reporting the expected significance, which could be obtained for several signal hypotheses. To estimate the expected significance, we use an Asimov dataset, which is described in more detail later. In this section, we outline the procedure used to search for the $H \to \tau\tau$ decay in the context of the frequentist statistical test.

For the purpose of discovery, one defines a null hypothesis H_0, also called the

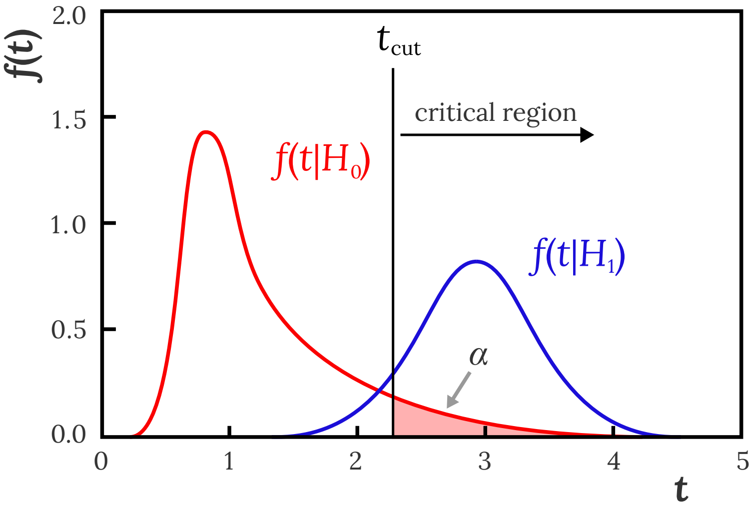

Figure 4.4: An illustration of the critical region of a statistical test. Probability densities $f(t|H_0)$ and $f(t|H_1)$ for the test statistic t under the assumption of hypotheses H_0 and H_1, respectively. H_0 is rejected if t is observed in the critical region, here defined as $t > t_{cut}$ [61].

background-only hypothesis, that describes only the known processes, which are here considered as background contributions. The hypothesis H_0 is tested against an alternative hypothesis H_1, which includes both background contributions and the sought after signal.

We can formulate a statement about the compatibility between the observed data and tested hypotheses in terms of a decision to accept or reject the null hypothesis by defining a critical region (or its complementary acceptance region) for a test statistic. We demonstrate this on an example shown in Figure 4.4, in which we use a test statistic $t(x)$ and pdfs for both hypotheses, $f(t|H_0)$ and $f(t|H_1)$. If the value of the observed t falls within the critical region, here defined as $t > t_{cut}$, we reject the hypothesis H_0; otherwise, it is accepted. The critical region is chosen in such a way that the probability for t to be observed there, under an assumption of H_0, is no more than some value α[2] called the size of the test, defined as

$$\alpha = \int_{t_{cut}}^{\infty} f(t|H_0)dt, \tag{4.23}$$

which is a constant specified before the test is performed, usually set to a small value such as 5%.

However, many of the possible subsets of the data space generally satisfy the aforementioned criterion, and it is not clear which region should be chosen as the critical region. That is why we consider also an alternative hypothesis H_1. In particular, we want to chose the critical region in such a way that it has the highest possible probability to find the data there if H_1 is true, while having only a fixed probability α assuming H_0.

Value of α corresponds to the probability that the null hypothesis will be rejected when it is true (a so-called Type-I error). On the other hand, β denotes

---

[2] Note, α is the conventional notation for the size of the test, and has nothing to do with the model parameters used in previous subsections.

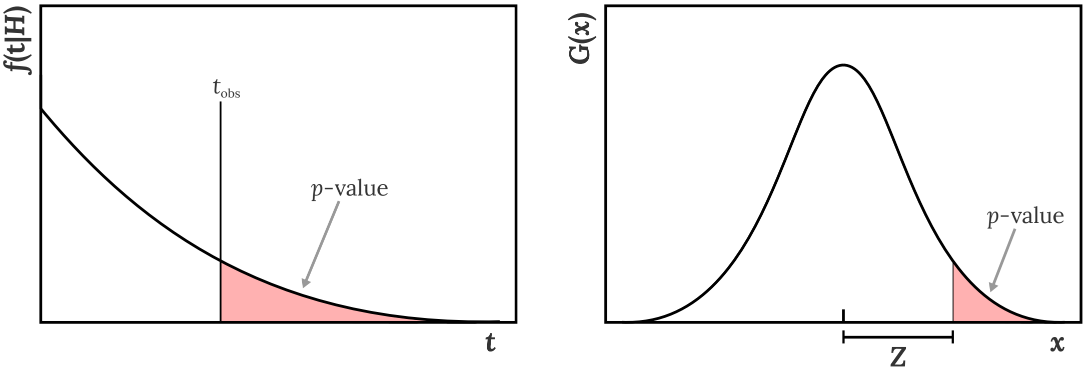

Figure 4.5: Left: An illustration of the p-value obtained from an observed value of the test statistic t. Right: The standard normal distribution $G(x) = (1/\sqrt{2\pi}\exp(-x^2/2))$ showing the relation between the significance Z and the p-value [62].

the probability to accept the null hypothesis when the alternative hypothesis is true (a so-called Type-II error). Then, the 'power' of the hypothesis test is defined as $1 - \beta$ and it corresponds to the probability to reject the null hypothesis if in fact the alternative hypothesis is true. Usually, one looks for a test statistic which maximises the power of the test for a fixed test size.

Furthermore, we can quantify the level of agreement between the observed data and a given hypothesis H_0, by computing the aforementioned p-value, defined as

$$p = \int_{t_{obs}}^{\infty} f(t|H_0)dt. \tag{4.24}$$

In this definition we consider the hypothesis H_0; however, the p-value can be calculated for any given hypothesis H.

The p-value corresponds to the probability, under the assumption of a hypothesis H_0, to find data in some region of equal or greater incompatibility with the predictions of H_0. The left plot in Figure 4.5 shows the definition of the p-value obtained from an observed value of the test statistic t.

In other words, to claim a discovery of some new phenomenon, we aim to demonstrate that what we observe is very unlikely under the assumption of H_0 and the probability to observe data even less compatible with H_0 is very small. The critical region for a test of H_0 of size α can be specified using the p-value as the set of data values that would have $p \leq \alpha$.

The p-value can be converted into an equivalent significance Z, defined such that a Gaussian distributed variable found Z standard deviations above[3] its mean has an upper-tail probability equal to p-value [63] (defined in Equation 4.24). The standard normal distribution in the right plot in Figure 4.5 demonstrates the relation between the significance Z and the p-value. The significance can be written as

$$Z = \Phi^{-1}(1 - p), \tag{4.25}$$

where Φ is the cumulative standard Gaussian distribution (zero mean, unit variance), and Φ^{-1} is its inverse function, the quantile of the standard Gaussian.

---

[3] Some authors define this relation using a two-sided fluctuation of a Gaussian distributed variable with 5σ significance corresponding to $p = 5.7 \times 10^{-7}$.

To claim a discovery of a new phenomenon, the significance of at least $Z = 5$ is often used by the particle physics community as the appropriate level to reject the background-only hypothesis. This value corresponds to the p-value of 2.9×10^{-7} for the background-only hypothesis. To exclude the signal hypothesis, the threshold $p = 0.05$ (corresponding to 95% confidence level) is used, which corresponds to $Z = 1.64$.

The commonly used procedure to establish the discovery in particle physics is based on the frequentist significance test using a likelihood ratio as the test statistic. It was proposed as the optimal test statistic by Neyman and Pearson [68] since it provides the highest power for a given size of the test α. However, this is only true in the case of two simple hypotheses (probability models without any parameters). The likelihood ratio is defined as

$$T = \frac{f(x|H_1)}{f(x|H_0)}, \tag{4.26}$$

and it is referred to as the Neyman-Pearson lemma.

Unfortunately, there is no equivalent to the Neyman-Pearson lemma for models with several free parameters. Nevertheless, its natural generalisation is based on the profile likelihood ratio [63], defined as

$$\lambda(\mu) = \frac{L(\mu, \hat{\hat{\boldsymbol{\theta}}}(\mu))}{L(\hat{\mu}, \hat{\boldsymbol{\theta}})}, \tag{4.27}$$

where $L(\mu, \boldsymbol{\theta})$ is defined in Equation (4.17). We use two different likelihood estimators to profile the NPs. Namely, $L(\hat{\mu}, \hat{\boldsymbol{\theta}})$, which is the unconditional maximum likelihood estimator that corresponds to the best fit result, and $L(\mu, \hat{\hat{\boldsymbol{\theta}}}(\mu))$, which is the conditional maximum likelihood estimator that provides an estimate of the NPs for a given value of μ. In the $H \to \tau\tau$ cross-section measurement, we follow the recommendations from the LHC Higgs Combination Working Group, and therefore we use the profile likelihood ratio as the test statistic.

In the large sample limit, the profile likelihood ratio is independent of the NPs, since they are absorbed (profiled) in the likelihood fit. As the result, $\lambda(\mu)$ depends only on the POI, the observed number of events and the auxiliary measurements. The profile likelihood ratio provides almost as powerful hypothesis testing as the optimal test statistic, the likelihood ratio. However, the disadvantage of the likelihood ratio is its dependance on the NPs.

Although in reality, the signal strength is always non-negative, in order to account for downward background fluctuations, one can allow for negative values in the fit by modifying $\lambda(\mu)$

$$\tilde{\lambda}(\mu) = \begin{cases} \frac{L(\mu, \hat{\hat{\boldsymbol{\theta}}}(\mu))}{L(\hat{\mu}, \hat{\boldsymbol{\theta}})} & \text{for } \hat{\mu} \geq 0, \\ \frac{L(\mu, \hat{\hat{\boldsymbol{\theta}}}(\mu))}{L(0, \hat{\hat{\boldsymbol{\theta}}}(0))} & \text{for } \hat{\mu} < 0, \end{cases} \tag{4.28}$$

where $\hat{\mu}$ is an effective estimator which is allowed to take on negative values. Moreover, the definition in Equation (4.28) allows to model $\hat{\mu}$ as a Gaussian distributed variable and thus enables to determine the distributions of the considered test statistics. Then the corresponding test statistic is

$$\tilde{t}_\mu = -2 \ln \tilde{\lambda}(\mu). \tag{4.29}$$

In the special case of discovery of a positive signal, we use the notation $q_0 = \tilde{t}_0$. As long as our signal models fit the description above, we can define the statistics q_0 for the discovery of a positive signal (used to test $\mu = 0$) as

$$q_0 = \begin{cases} -2\ln\lambda(0) & \text{for } \hat{\mu} \geq 0, \\ 0 & \text{for } \hat{\mu} < 0, \end{cases} \tag{4.30}$$

where $\lambda(0)$ is the profile likelihood ratio for $\mu = 0$ as defined in Equation (4.27). With this definition, we can see that the data show lack of agreement with H_0 hypothesis only if $\hat{\mu} > 0$. In this way higher values of q_0 correspond to increasing disagreement between data and H_0 hypothesis. If the data fluctuate such that we find fewer events than were predicted by the background processes alone, then $\hat{\mu} < 0$ and $q_0 = 0$. A value of $\hat{\mu}$ much below zero shows a discrepancy between the data and a hypothesis as well; however, it does not show that the data contain signal events, but rather points to some systematic error.

To quantify the level of disagreement between the data and H_0 using the observed value of q_0, we compute the p-value as

$$p_0 = \int\limits_{q_{0,obs}}^{\infty} f(q_0|0)dq_0, \tag{4.31}$$

where $f(q_0|0)$ denotes the pdf of the statistic q_0 under the assumption of the background-only hypothesis H_0.

To calculate the p-value one needs to know the distribution of the test statistic for the same μ as the one being tested. Using sufficiently large data samples these distributions reach an asymptotic form related to the χ^2 distribution, with the number of degrees of freedom being equal to the number of POIs. The asymptotic formulae are based on theorems due to Wilks [69] and Wald [70] and are described in more detail in Reference [63].

A big advantage of using profile likelihood ratio is that the asymptotic distribution does not depend on NPs and it is not necessary to choose their specific values to calculate the p-value. It means that if we reject $\mu = 0$ hypothesis, it remains rejected irrespective of the values of NPs. However, we know that in a real analyses the data samples are of finite size and thus the p-values for the POIs depend on the NPs to some extent. To confirm the dependence of the obtained results on the NPs, we can use their profiled values $\hat{\hat{\theta}}$ for the value of μ, which is actually tested. If the profiled values of the NPs are equal to their true values, then the p-value for μ is correct and also the confidence interval covers the true value. However, if the true values of θ are not equal to the profiled values, then the p-value and the confidence intervals might be wrong.

5. $H \to \tau\tau$ cross-section measurements

The measurement of the Higgs boson coupling to a pair of tau leptons is crucial in assessing the mechanism for fermion mass generation in the SM. A discovery of this coupling was established by combining ATLAS and CMS results, which used part of Run 1 dataset [9, 10, 11]. The combined result showed 5.5σ excess above the background-only hypothesis and thus confirmed the existence of the $H \to \tau\tau$ decay mode. Recently, $H \to \tau\tau$ decay was discovered by the CMS experiment combining the whole Run 1 dataset and $35.9\,\text{fb}^{-1}$ of Run 2 dataset [35]. This chapter outlines the measurement that verified this coupling with the ATLAS experiment.

We present cross-section measurements of the Higgs bosons decaying to a pair of tau leptons [22] using data collected at $\sqrt{s} = 13\,\text{TeV}$ by the ATLAS experiment, corresponding to an integrated luminosity of $36.1\,\text{fb}^{-1}$. We consider all combinations of leptonic ($\tau \to \ell\nu\bar{\nu}$)[1] and hadronic ($\tau \to$ hadrons ν) tau lepton decays, which result in three analysis channels. These channels are referred to as leptonic $\tau_{\text{lep}}\tau_{\text{lep}}$, semi-leptonic $\tau_{\text{lep}}\tau_{\text{had}}$ and hadronic $\tau_{\text{had}}\tau_{\text{had}}$. Furthermore, we define two analysis categories, namely VBF and boosted, in such a way that they are mainly sensitive to Higgs bosons produced via VBF and ggF production modes, respectively. To obtain the final results, we perform a maximum-likelihood fit on data using the distributions of reconstructed di-tau mass $m_{\tau\tau}$ in signal regions (SRs). Simultaneously, the event yields from the control regions (CRs) constrain the normalisations of major background components estimated from the simulations. The mass of the Higgs boson is assumed to be $125\,\text{GeV}$ [71].

In this analysis I had a role of a fit expert. I have scrutinised the fit model and using the Asimov dataset and low mass fit, implemented systematic uncertainties into the model and provided the final results using the measured data.

5.1 Data and simulation samples

The samples used for this measurement consist of $3.2\,\text{fb}^{-1}$ and $32.9\,\text{fb}^{-1}$ of pp collision data recorded by the ATLAS detector in 2015 and 2016, respectively. To record analysed data, ATLAS used a combination of triggers, in particular the trigger for single light leptons, two light leptons and two hadronically decaying tau leptons. MC generators utilised to simulate signal and background processes are summarised in Table 5.1.

Considered signal contributions include the following Higgs boson production processes: ggF, VBF, VH and $t\bar{t}H$, since the contributions from other Higgs boson production modes such as the associated production with a bottom-antibottom quark pair or with a single top quark are negligible.

Considered background processes are the electroweak (EW) production of W/Z bosons from VBF, the W/Z boson production with associated jets, the di-boson production processes, the generation of top-antitop quark pair $t\bar{t}$ and the

---

[1] The symbol ℓ denotes electrons and muons, also referred to as 'light leptons'.

Table 5.1: Monte Carlo generators used to simulate all signal and background processes, including the corresponding PDF set and the model of underlying event, hadronisation and parton shower (UEPS). Furthermore, the order of the total cross-section calculation is listed. The total cross-section for VBF is calculated at approximately next-to-next-to-leading order (NNLO) QCD.

Process	Monte Carlo generator	PDF	UEPS	Cross-section order
ggF	Powheg-Box v2	PDF4LHC15 NNLO	Pythia 8.212	N^{3}LO QCD + NLO EW
VBF	Powheg-Box v2	PDF4LHC15 NLO	Pythia 8.212	$\sim$NNLO QCD + NLO EW
VH	Powheg-Box v2	PDF4LHC15 NLO	Pythia 8.212	NNLO QCD + NLO EW
$t\bar{t}H$	MG5_aMC@NLO v2.2.2	NNPDF30LO	Pythia 8.212	NLO QCD + NLO EW
$W/Z+$jets	Sherpa 2.2.1	NNPDF30NNLO	Sherpa 2.2.1	NNLO
$VV/V\gamma^*$	Sherpa 2.2.1	NNPDF30NNLO	Sherpa 2.2.1	NLO
$t\bar{t}$	Powheg-Box v2	CT10	Pythia 6.428	NNLO+NNLL
Wt	Powheg-Box v1	CT10F4	Pythia 6.428	NLO

single-top quark production Wt. The Higgs boson decays to a pair of W bosons are considered as a background in the $\tau_{\text{lep}}\tau_{\text{lep}}$ channel.

For all simulated signal and background samples, we performed a full simulation of the ATLAS detector response [72] using the Geant4 program [73].

5.2 Object reconstruction and identification

A tau lepton with a mass of $1776.82 \pm 0.16\,\text{MeV}$ [33] decays into lighter leptons or hadrons and at least one neutrino. Thus for this measurement, it is necessary to reconstruct electrons, muons, jets, visible decays products of hadronic tau lepton decays $\tau_{\text{had-vis}}$ and missing transverse energy $E_{\text{T}}^{\text{miss}}$. We use additional jets in order to classify events into the VBF and boosted categories, and to suppress contributions from the background processes.

Leptonic tau lepton decays are reconstructed as electrons and muons, while hadronic tau lepton decays consist of a mixture of charged and neutral hadrons and one neutrino, and we can only reconstruct their visible decay products. In general, we are able to distinguish the jets originating from tau leptons (tau-jets) from the jets initiated by quarks or gluons (QCD jets). Usually, a tau-jet originates from one or three charged hadrons and none, one or two neutral pions emitted close to the direction of the tau lepton. On the other hand, a QCD jet has on average higher multiplicity of hadrons than a tau-jet and it is emitted in a wider cone around the jet axis.

In this measurement, object reconstruction and identification is the following. First, the physics objects which traverse the detector are reconstructed with the criteria summarised below. After the object reconstruction, we apply the so-called overlap removal (ORL) procedure between the objects whose $\Delta R = \sqrt{\Delta\phi^2 + \Delta\eta^2}$ is smaller than a certain threshold. The ORL removes ambiguities in the case that the same object is reconstructed by several algorithms. Since the three analysis channels have different event topologies and background contributions, after the ORL, we apply additional criteria for each analysis channel to select signal events and suppress background events.

For the reconstruction of muon candidates, the inner detector track has to match the track reconstructed in the muon spectrometer [74]. Furthermore, we require muon candidates to have $p_{\mathrm{T}} > 10\,\mathrm{GeV}$ and $|\eta| < 2.5$, and to pass the 'loose' muon identification requirements of the Reference [74]. The trigger efficiency for single muon candidates selected in the analysis is nearly 80% (70%) in the barrel region and 90% in the end-cap regions in the 2016 (2015) dataset [75]. We ignore the muon candidates if the angular distance between the muon and a jet is $\Delta R < 0.4$. However, we ignore the jet instead of the muon, if the muon track is associated with the jet or $\Delta R < 0.2$ and at the same time the jet has either less than twice p_{T} of the muon candidate or less than three tracks.

For the reconstruction of electron candidates, we require the energy deposits in the electromagnetic calorimeter to match the charged-particle tracks measured in the inner detector. Furthermore, the electron candidates have to have $p_{\mathrm{T}} > 15\,\mathrm{GeV}$ and $|\eta| < 2.47$ (to be in the fiducial volume of the inner detector), and to pass the 'loose' likelihood-based identification selection of the References [76, 77]. We ignore the events from the transition region between the barrel and the end-cap calorimeters corresponding to $1.37 < |\eta| < 1.52$. For single electrons considered in the analysis, the trigger efficiency varies between 90% and 95% [75]. The ORL requires to ignore the electron candidates which share the reconstructed track with a muon candidate or if the angular distance between the electron candidates and a jet is within $0.2 < \Delta R < 0.4$.

Jets are reconstructed from topological clusters of energy deposits in the calorimeter. We use the anti-k_t algorithm [78, 79] with the radius parameter value $R = 0.4$. Only jets with $p_{\mathrm{T}} > 20\,\mathrm{GeV}$ and $|\eta| < 4.9$ are considered in the analysis. To reject jets from pileup in the central region ($|\eta| < 2.4$) we use Jet Vertex Tagger (JVT) algorithm [80], applied to jets with $p_{\mathrm{T}} < 50\,\mathrm{GeV}$. To reject jets from pileup in the forward region, forward JVT [81] algorithm is applied to jets with $p_{\mathrm{T}} < 50\,\mathrm{GeV}$ and $|\eta| > 2.5$. Jets within $\Delta R = 0.2$ of an electron or hadronically decaying tau candidate are removed.

The reconstruction of $\tau_{\text{had-vis}}$ starts with a reconstructed jet which has $p_{\mathrm{T}} > 10\,\mathrm{GeV}$ and $|\eta| < 2.5$. To distinguish $\tau_{\text{had-vis}}$ from the jets initiated by light-quarks or gluons, we apply an identification algorithm which uses multivariate techniques and requires $\tau_{\text{had-vis}}$ candidates to pass 'loose' identification criterion of the Reference [82]. Furthermore, $\tau_{\text{had-vis}}$ candidates must have $p_{\mathrm{T}} > 20\,\mathrm{GeV}$, the absolute electric charge equal to one, and one or three associated tracks. The trigger efficiency is 95% for 1-prong tau leptons and 85% for 3-prong tau leptons selected in the analysis [83]. We remove $\tau_{\text{had-vis}}$ which are within $\Delta R = 0.2$ of an electron or muon candidate.

Furthermore, in the $\tau_{\text{lep}}\tau_{\text{lep}}$ and $\tau_{\text{lep}}\tau_{\text{had}}$ SRs, we consider only events with electron or muon candidates passing their respective 'medium' identification criteria. The reconstruction and identification efficiency for muons with the 'medium' identification requirement has been measured in $Z \to \mu\mu$ events [74]. The measured efficiency is above 98% across the full phase space, except for the region of $|\eta| < 0.1$, where it amounts to about 70%. The efficiency for electrons with the 'medium' identification requirement has been measured in $Z \to ee$ events and varies between 80% and 90% in the p_{T} range of $10\,\mathrm{GeV}$ to $80\,\mathrm{GeV}$. Furthermore, both electrons and muons have to meet the 'gradient' isolation criterion. It requires the cone around the track not to contain additional high-p_{T} tracks and the cone around the calorimeter clusters of the object not to contain significant energy deposits (after correcting for pileup) [74, 77].

The $\tau_{\text{had-vis}}$ candidates are required to pass different identification criteria in the $\tau_{\text{lep}}\tau_{\text{had}}$ and $\tau_{\text{had}}\tau_{\text{had}}$ SRs. In the $\tau_{\text{lep}}\tau_{\text{had}}$ channel, $\tau_{\text{had-vis}}$ candidates have to pass the 'medium' identification requirement, which corresponds to the efficiency of 55% for a real 1-prong and 40% for a real 3-prong $\tau_{\text{had-vis}}$ [82]. Moreover, if an electron candidate and a 1-prong $\tau_{\text{had-vis}}$ candidate are selected, we apply a dedicated multivariate algorithm to reject the electrons misidentified as $\tau_{\text{had-vis}}$ and thus suppress $Z \to ee$ events. In the $\tau_{\text{had}}\tau_{\text{had}}$ channel, we require $\tau_{\text{had-vis}}$ to pass the 'tight' identification criterion, which results in the efficiency of 45% for a real 1-prong $\tau_{\text{had-vis}}$ and 30% for a real 3-prong $\tau_{\text{had-vis}}$ [82].

The Higgs boson candidate is reconstructed from the $\tau_{\text{had-vis}}$ and the $E_{\text{T}}^{\text{miss}}$. Its p_{T} is calculated as the vector sum of the tau visible decay products p_{T} and the $E_{\text{T}}^{\text{miss}}$. The latter is assumed to originate from the final state neutrinos and it is defined as the magnitude of the missing transverse momentum vector. This vector is calculated as the negative vectorial sum of p_{T} of the fully calibrated and reconstructed physics objects [84]. We use two approaches to compute the invariant mass of a pair of tau leptons $m_{\tau\tau}$, in particular the missing-mass calculator (MMC) [85] and the collinear approximation [86]. The $m_{\tau\tau}$ calculated using the MMC is labelled as $m_{\tau\tau}^{\text{MMC}}$ and the one obtained from the collinear approximation as $m_{\tau\tau}^{\text{coll}}$. These methods are discussed in more detail in Appendix A.

5.3 Event selection and categorisation

We reject events which contain reconstructed jets associated with energy deposited in the calorimeter that might arise from hardware problems, beam-halo events or cosmic-ray showers. Furthermore, we require the presence of one reconstructed primary vertex, which is defined as the vertex with the highest sum of the transverse momenta squared of all associated tracks, and we require presence of at least two associated tracks with $p_{\text{T}} > 0.5\,\text{GeV}$. These requirements reject the non-collision events originating from cosmic rays or beam-halo events.

5.3.1 Event selection

We use several triggers to select electron, muon and $\tau_{\text{had-vis}}$ candidates, with additional requirements applied to their transverse momentum, summarised in Table 5.2.

We require all considered events to have at least one jet j_1 with $p_{\text{T}}^{j_1} > 40\,\text{GeV}$. Then, the two tau leptons originating from the Higgs boson decay recoil against one or more high-p_{T} jets, while the background processes are usually produced nearly at rest. Hence, the background processes tend to have softer di-tau transverse momenta $p_{\text{T}}^{\tau\tau}$ then the Higgs boson candidate, what makes the selection of interesting events easier.

The event selection of the three analysis channels is summarised in Table 5.3. In order to reject the events without neutrinos we select only the events with $E_{\text{T}}^{\text{miss}} > 20\,\text{GeV}$. To suppress the background contribution from $Z \to \ell\ell$ processes, the tighter requirement on $E_{\text{T}}^{\text{miss}}$ and on the invariant mass of two light leptons $m_{\ell\ell}$ is applied in the final state with two same-flavour (SF) leptons. In the $\tau_{\text{lep}}\tau_{\text{had}}$ channel, we reject the events with leptonic W decays by requiring low transverse

Table 5.2: The summary of the triggers used to select events for the three analysis channels during 2015 and 2016 data taking and the corresponding p_T requirements applied in the analysis. For the electron+muon trigger, the first number corresponds to the electron p_T requirement, the second to the muon p_T requirement. For the $\tau_\mathrm{had}\tau_\mathrm{had}$ channel, at least one high-p_T jet in addition to the two $\tau_\text{had-vis}$ candidates is required for the 2016 dataset.

Analysis channel	Trigger	Analysis p_T requirement [GeV] 2015	2016
$\tau_\mathrm{lep}\tau_\mathrm{lep}$ & $\tau_\mathrm{lep}\tau_\mathrm{had}$	Single electron	25	27
	Single muon	21	27
$\tau_\mathrm{lep}\tau_\mathrm{lep}$	Dielectron	15 / 15	18 / 18
	Dimuon	19 / 10	24 / 10
	Electron+muon	18 / 15	18 / 15
$\tau_\mathrm{had}\tau_\mathrm{had}$	Di-$\tau_\text{had-vis}$	40 / 30	40 / 30

Table 5.3: The summary of the event selection requirements for the three analysis channels that are applied in addition to the respective lepton p_T requirements listed in Table 5.2. $E_\mathrm{T}^\text{miss, hard}$ is an alternative E_T^miss calculated only from the physics objects without the soft-track term. The transverse mass m_T is calculated from E_T^miss and the momentum of the selected light lepton. The visible momentum fractions x_1 and x_2 of the respective tau lepton and the collinear di-tau mass $m_{\tau\tau}^\text{coll}$ are calculated in the collinear approximation [86].

$\tau_\mathrm{lep}\tau_\mathrm{lep}$ $ee/\mu\mu$	$e\mu$	$\tau_\mathrm{lep}\tau_\mathrm{had}$	$\tau_\mathrm{had}\tau_\mathrm{had}$
$N_{e/\mu}^\text{loose} = 2$, $N_{\tau_\text{had-vis}}^\text{loose} = 0$		$N_{e/\mu}^\text{loose} = 1$, $N_{\tau_\text{had-vis}}^\text{loose} = 1$	$N_{e/\mu}^\text{loose} = 0$, $N_{\tau_\text{had-vis}}^\text{loose} = 2$
e/μ : Medium, gradient iso.		e/μ : Medium, gradient iso.	
		$\tau_\text{had-vis}$: Medium	$\tau_\text{had-vis}$: Tight
Opposite charge		Opposite charge	Opposite charge
$m_{\tau\tau}^\text{coll} > m_Z - 25\,\text{GeV}$		$m_\mathrm{T} < 70\,\text{GeV}$	
$30 < m_{\ell\ell} < 75\,\text{GeV}$	$30 < m_{\ell\ell} < 100\,\text{GeV}$		
$E_\mathrm{T}^\text{miss} > 55\,\text{GeV}$	$E_\mathrm{T}^\text{miss} > 20\,\text{GeV}$	$E_\mathrm{T}^\text{miss} > 20\,\text{GeV}$	$E_\mathrm{T}^\text{miss} > 20\,\text{GeV}$
$E_\mathrm{T}^\text{miss, hard} > 55\,\text{GeV}$			
$\Delta R_{\tau\tau} < 2.0$		$\Delta R_{\tau\tau} < 2.5$	$0.8 < \Delta R_{\tau\tau} < 2.5$
$\lvert\Delta\eta_{\tau\tau}\rvert < 1.5$		$\lvert\Delta\eta_{\tau\tau}\rvert < 1.5$	$\lvert\Delta\eta_{\tau\tau}\rvert < 1.5$
$0.1 < x_1 < 1.0$		$0.1 < x_1 < 1.4$	$0.1 < x_1 < 1.4$
$0.1 < x_2 < 1.0$		$0.1 < x_2 < 1.2$	$0.1 < x_2 < 1.4$
$p_\mathrm{T}^{j_1} > 40\,\text{GeV}$		$p_\mathrm{T}^{j_1} > 40\,\text{GeV}$	$p_\mathrm{T}^{j_1} > 70\,\text{GeV}, \lvert\eta^{j_1}\rvert < 3.2$
$N_\text{b-jets} = 0$		$N_\text{b-jets} = 0$	

mass m_T, calculated from the momentum of the selected light lepton and $E_\mathrm{T}^\mathrm{miss}$. Moreover, in the $\tau_\mathrm{lep}\tau_\mathrm{lep}$ and $\tau_\mathrm{lep}\tau_\mathrm{had}$ channels we use b-tagging information to suppress background events originating from top quark decays.

To suppress events from $Z \to \ell\ell$ background and to ensure the orthogonality between our measurement and the measurement with a similar final state $H \to WW^* \to \ell\nu\ell\nu$ [87], we introduce the requirement of $m_{\tau\tau}^\mathrm{coll} > m_Z - 25\,\mathrm{GeV}$ in the $\tau_\mathrm{lep}\tau_\mathrm{lep}$ channel.

To suppress events with $E_\mathrm{T}^\mathrm{miss}$ not compatible with the $H \to \tau\tau$ decays, we apply requirements on x_i, which stands for the fraction of the i^th tau lepton (ordered in descending p_T) momentum carried by each visible decay product. It is defined as

$$x_i = \frac{p_i^\mathrm{vis}}{p_i^\mathrm{vis} + p_i^\mathrm{miss}},$$

where p_i^vis and p_i^miss are the visible and missing momenta, respectively, calculated in the collinear approximation [86]. Since non-resonant background events might occur in all analysis channels, we apply the requirements on the angular distance $\Delta R_{\tau\tau}$ between the visible decay products of the two selected tau lepton decays and their pseudorapidity difference $|\Delta\eta_{\tau\tau}|$.

5.3.2 Signal and control regions

We define two analysis categories VBF and boosted, in order to get signal-sensitive event topologies. The definition of these categories is summarised in Table 5.4. The two categories are referred to as ‘inclusive’ categories and they fill two independent phase spaces without an overlap.

The VBF category targets the events with the Higgs boson produced by VBF production mode; however, it also includes contributions from the ggF production mode, which amounts up to 30% of the total expected Higgs boson signal. The VBF category requires the presence of a second high-p_T jet ($p_\mathrm{T}^{j_2} > 30\,\mathrm{GeV}$) and the invariant mass of the two jets to be $m_{jj} > 400\,\mathrm{GeV}$. Furthermore, these jets are required to lie in opposite hemispheres of the detector, thus we select the jets with large pseudorapidity separation $\Delta\eta_{jj} > 3$ and the light leptons with η-values lying between the η-values of the two jets.

The boosted category is predominantly sensitive to the events with the Higgs bosons produced through ggF production mode. The presence of additional jets results in a harder p_T spectrum of the Higgs boson signal compared to the $Z \to \tau\tau$ events. All events which fail the VBF selection and have $p_\mathrm{T}^{\tau\tau}$ greater than 100 GeV end up in the boosted category. The contributions from the VBF and VH production processes in the boosted category is $10 - 20\%$ of the expected signal. We ignore events which do not fall into the VBF or boosted categories.

To improve the sensitivity of the measurement, we further split inclusive VBF and boosted categories into 13 exclusive SRs with different signal to background ratios. These regions are selected by applying the requirements on $p_\mathrm{T}^{\tau\tau}$, $\Delta R_{\tau\tau}$ and m_{jj} which are summarised in Table 5.4.

The CRs are defined as the regions of the phase space, in which a specific background process is dominant. Therefore, they are used to adjust the simulated prediction of a background contribution to match the observed data. The CRs

Table 5.4: The definition of the VBF and boosted analysis categories and their respective signal regions. The selection criteria, which are applied in addition to those described in Table 5.3, are listed for each analysis channel. The VBF high-$p_{\mathrm{T}}^{\tau\tau}$ signal region is only defined for the $\tau_{\mathrm{had}}\tau_{\mathrm{had}}$ channel, resulting in seven VBF signal regions and six boosted signal regions. All signal regions are exclusive and their yields add up to those of the corresponding VBF and boosted inclusive regions.

Signal Region		Inclusive	$\tau_{\mathrm{lep}}\tau_{\mathrm{lep}}$	$\tau_{\mathrm{lep}}\tau_{\mathrm{had}}$	$\tau_{\mathrm{had}}\tau_{\mathrm{had}}$
VBF	High-$p_{\mathrm{T}}^{\tau\tau}$	$p_{\mathrm{T}}^{j_2} > 30\,\mathrm{GeV}$ $\lvert\Delta\eta_{jj}\rvert > 3$ $m_{jj} > 400\,\mathrm{GeV}$ $\eta_{j_1} \cdot \eta_{j_2} < 0$ Central leptons	—		$p_{\mathrm{T}}^{\tau\tau} > 140\,\mathrm{GeV}$ $\Delta R_{\tau\tau} < 1.5$
	Tight		$m_{jj} > 800\,\mathrm{GeV}$	$m_{jj} > 500\,\mathrm{GeV}$ $p_{\mathrm{T}}^{\tau\tau} > 100\,\mathrm{GeV}$	Not VBF high-$p_{\mathrm{T}}^{\tau\tau}$ $m_{jj} > (1550 - 250 \cdot \lvert\Delta\eta_{jj}\rvert)\,\mathrm{GeV}$
	Loose		Not VBF tight		Not VBF high-$p_{\mathrm{T}}^{\tau\tau}$ and not VBF tight
Boosted	High-$p_{\mathrm{T}}^{\tau\tau}$	Not VBF $p_{\mathrm{T}}^{\tau\tau} > 100\,\mathrm{GeV}$	$p_{\mathrm{T}}^{\tau\tau} > 140\,\mathrm{GeV}$ $\Delta R_{\tau\tau} < 1.5$		
	Low-$p_{\mathrm{T}}^{\tau\tau}$		Not boosted high-$p_{\mathrm{T}}^{\tau\tau}$		

Table 5.5: The definition of the six control regions (CRs) used to constrain the $Z \to \ell\ell$ and top backgrounds to the event yield in data in the $\tau_{\mathrm{lep}}\tau_{\mathrm{lep}}$ and $\tau_{\mathrm{lep}}\tau_{\mathrm{had}}$ channels. SF denotes a selection of same-flavour light leptons.

Region	Selection
$\tau_{\mathrm{lep}}\tau_{\mathrm{lep}}$ VBF $Z \to \ell\ell$ CR	$\tau_{\mathrm{lep}}\tau_{\mathrm{lep}}$ VBF incl. selection, $80 < m_{\ell\ell} < 100\,\mathrm{GeV}$, SF
$\tau_{\mathrm{lep}}\tau_{\mathrm{lep}}$ boosted $Z \to \ell\ell$ CR	$\tau_{\mathrm{lep}}\tau_{\mathrm{lep}}$ boosted incl. selection, $80 < m_{\ell\ell} < 100\,\mathrm{GeV}$, SF
$\tau_{\mathrm{lep}}\tau_{\mathrm{lep}}$ VBF top CR	$\tau_{\mathrm{lep}}\tau_{\mathrm{lep}}$ VBF incl. selection, inverted b-jet veto
$\tau_{\mathrm{lep}}\tau_{\mathrm{lep}}$ boosted top CR	$\tau_{\mathrm{lep}}\tau_{\mathrm{lep}}$ boosted incl. selection, inverted b-jet veto
$\tau_{\mathrm{lep}}\tau_{\mathrm{had}}$ VBF top CR	$\tau_{\mathrm{lep}}\tau_{\mathrm{had}}$ VBF incl. selection, inverted b-jet veto, $m_{\mathrm{T}} > 40\,\mathrm{GeV}$
$\tau_{\mathrm{lep}}\tau_{\mathrm{had}}$ boosted top CR	$\tau_{\mathrm{lep}}\tau_{\mathrm{had}}$ boosted incl. selection, inverted b-jet veto, $m_{\mathrm{T}} > 40\,\mathrm{GeV}$

follow almost identical selection criteria as the SRs, but usually, one or several SRs criteria are inverted. The definition of the CRs is summarised in Table 5.5.

In the $\tau_{\mathrm{lep}}\tau_{\mathrm{lep}}$ channel, we introduce two $Z \to \ell\ell$ CRs by applying the same selection as for the SF events in the SRs; however, we require $80 < m_{\ell\ell} < 100\,\mathrm{GeV}$. The resulting CRs are 90% pure in $Z \to \ell\ell$ events.

Since a top quark decays to a W boson and a bottom quark, its background is characterised by the presence of b-jets. We define the top quark CRs by inverting the b-jet veto requirement in both inclusive categories for the $\tau_{\mathrm{lep}}\tau_{\mathrm{lep}}$ and $\tau_{\mathrm{lep}}\tau_{\mathrm{had}}$ channels. In the $\tau_{\mathrm{lep}}\tau_{\mathrm{lep}}$ channel, the purity of the top CR is about 80%, while in the $\tau_{\mathrm{lep}}\tau_{\mathrm{had}}$ channel it amounts to 70% and 60% in the VBF and boosted category, respectively.

In the $\tau_{\mathrm{had}}\tau_{\mathrm{had}}$ channel, the $Z \to \ell\ell$ and top quark processes have negligible contributions, and thus we do not define corresponding CRs.

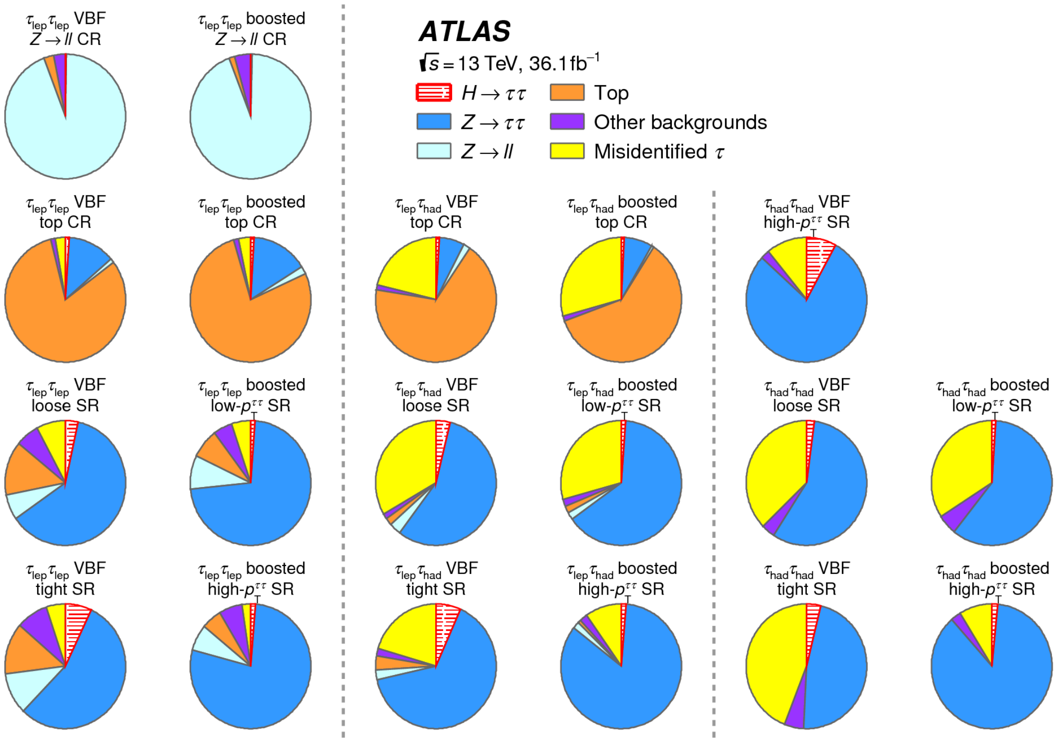

Figure 5.1: The expected signal and background composition in 6 control regions (CRs) and 13 signal regions (SRs) used in the analysis.

5.4 Background estimation

The expected signal and background compositions in all SRs and CRs are summarised in Figure 5.1. Various final-state topologies of the three analysis channels have different background compositions, thus we need to use different strategies for their background estimation. We use both data-driven methods and MC simulations to derive the expected number of background events and kinematic distributions in each SR.

5.4.1 $Z \to \tau\tau$ background

The dominant background component in all analysis channels is the Drell-Yan process $pp \to Z/\gamma^* \to \tau\tau$. Its contribution varies between 50% and 90% of the total background depending on the SR. Our ability to distinguish between the Drell-Yan and the $H \to \tau\tau$ signal processes is limited by the $m_{\tau\tau}^{\mathrm{MMC}}$ resolution.

We use MC simulations to model the $Z \to \tau\tau$ background, in particular, the Sherpa generator. This is different from the search for $H \to \tau\tau$ decays in Run 1 [9], which used the embedding technique [88]. We verify the modelling of this important background by using $Z \to \tau\tau$ validation regions (VRs). They consist of $Z \to \ell\ell$ events as their kinematics is similar to the $Z \to \tau\tau$ background in the respective SRs. More details about the $Z \to \tau\tau$ VRs can be found in Appendix B.

5.4.2 $Z \to \ell\ell$ background

$Z \to \ell\ell$ events form a significant background for the $\tau_{\text{lep}}\tau_{\text{lep}}$ and $\tau_{\text{lep}}\tau_{\text{had}}$ channels, in which mismeasured $E_{\text{T}}^{\text{miss}}$ can bias the reconstructed $m_{\tau\tau}^{\text{MMC}}$ of light-lepton pairs towards values similar to those expected for the signal. In the $\tau_{\text{lep}}\tau_{\text{had}}$ channel, this background contributes mainly through $Z \to ee$ events, where an electron is misidentified as $\tau_{\text{had-vis}}$ candidate [82]. To suppress these events we use the dedicated electron veto algorithm which selects 1-prong $\tau_{\text{had-vis}}$ candidates and this background results in negligible contribution. Therefore, we consider $Z \to \ell\ell$ CRs only in the $\tau_{\text{lep}}\tau_{\text{lep}}$ channel, with a significant contribution of $Z \to \ell\ell$ events in the final state with two SF leptons.

5.4.3 Top quark background

In the top quark decays $t \to Wb$, followed by the $W \to \ell\nu$ decay, the prompt light leptons are produced with associated $E_{\text{T}}^{\text{miss}}$. Thus the events originating from both the top-antitop quark pairs and a single top quark production, form a significant background in the $\tau_{\text{lep}}\tau_{\text{lep}}$ and $\tau_{\text{lep}}\tau_{\text{had}}$ channels, labelled as 'top background'. For its estimation, we use MC simulations. To select the events including the top quark, we apply the same selection criteria as for the SR; however, we invert the b-jet veto requirement to get at least one b-tagged jet and in the $\tau_{\text{lep}}\tau_{\text{had}}$ channel, we additionally require $m_{\text{T}} > 40\,\text{GeV}$.

5.4.4 Background from misidentified tau leptons

Contributions from light leptons and hadronic jets might be misidentified as prompt, light leptons or $\tau_{\text{had-vis}}$. In particular, light leptons can be misidentified as $\tau_{\text{had-vis}}$, labelled as 'fake-ℓ', while hadronic jets can be misidentified as $\tau_{\text{had-vis}}$, electrons or muons, labelled as 'fake-$\tau_{\text{had-vis}}$ '. Collectively, we label these processes as 'misidentified taus' or 'fakes'. We estimate fakes using data-driven techniques, applying specific methods in each analysis channel and they contribute up to a half of the total background depending on the SR.

To estimate the fake background in the $\tau_{\text{lep}}\tau_{\text{lep}}$ and $\tau_{\text{had}}\tau_{\text{had}}$ channels, we use fake templates, while in the $\tau_{\text{lep}}\tau_{\text{had}}$ channel we use the fake-factor method. Since the fake estimation is difficult in this measurement, we provide just its simplified explanation based on Reference [22], in which more detailed information can be found.

In the $\tau_{\text{lep}}\tau_{\text{lep}}$ channel, the main sources of the fake-ℓ background are multijets, W bosons in associated production with jets, and semileptonically decaying $t\bar{t}$ events. All these background sources are treated together. We define fake-ℓ regions in data by requiring the light lepton with the second-highest p_{T} to fail the 'gradient' isolation criterion, referred to as 'inverted' isolation. We create fake-ℓ templates from these samples by subtracting the simulated $Z \to \ell\ell$ and top backgrounds, which produce real light leptons. The normalisation of each template is then scaled by the factor which corrects for the inverted-isolation requirement.

The dominant contribution to the uncertainties in the fake-ℓ background in the $\tau_{\text{lep}}\tau_{\text{lep}}$ channel arises from the non-closure uncertainty and the uncertainty in the heavy-flavor content. Minor contributions come from the uncertainty in the fractional composition of the fake-ℓ background in top quark decays, W boson production and multijet events.

In the $\tau_{\text{had}}\tau_{\text{had}}$ channel, the multijet background is modelled using the template, built from the data which passed the SR selections, but we require the $\tau_{\text{had-vis}}$ candidates to have two tracks and to fail the opposite-charge requirement (nOC region). Then, simulated events with the true tau leptons from other SM processes are subtracted from the template. Afterwards, the template is reweighted using the scale factors which are derived by comparing the template from an nOC selection with a region obtained by requiring the $\tau_{\text{had-vis}}$ pair to have the opposite charge and the second-highest-p_{T} $\tau_{\text{had-vis}}$ to fail the 'tight', but pass the 'medium' identification requirements. In the $\tau_{\text{had}}\tau_{\text{had}}$ channel, the normalisation of the fake background is constrained in the fit by data in the $m_{\tau\tau}^{\text{MMC}}$ distribution in the SRs and the corresponding normalisation factor (NF) is correlated across all $\tau_{\text{had}}\tau_{\text{had}}$ SRs.

The dominant contribution to the uncertainties in the fake-$\tau_{\text{had-vis}}$ background in the $\tau_{\text{had}}\tau_{\text{had}}$ channel arises from the statistical uncertainties in scale factors. Minor contributions originate from the uncertainty in the extrapolation from the nOC region and the uncertainty from the subtraction of simulated backgrounds.

In the $\tau_{\text{lep}}\tau_{\text{had}}$ channel, fake-$\tau_{\text{had-vis}}$ background is composed mostly of multijet events and W boson production associated with jets. The fake-factor method utilises a fake-factor, which is defined as the ratio of the number of events where the highest-p_{T} jet is identified as a 'medium' $\tau_{\text{had-vis}}$ candidate to the number of events with the highest-p_{T} jet that passes a 'very loose' $\tau_{\text{had-vis}}$ identification, but fails the 'medium' one (anti-ID regions). Fake-factors depend on the track multiplicity, p_{T} of the $\tau_{\text{had-vis}}$ candidate and on the type of parton initiating the jet. For this reason, they are calculated separately in quark-jet-dominated 'W-enhanced' and gluon-jet-dominated 'multijet-enhanced' regions. The W-enhanced regions are defined by inverting the $m_{\text{T}} < 70\,\text{GeV}$ requirement and the multijet-enhanced regions are defined by inverting the light lepton isolation, relative to the inclusive boosted and VBF selections. To obtain the fake-$\tau_{\text{had-vis}}$ background estimate for the SRs, these fake-factors are weighted by the factor which corresponds to the ratio between the number of events in multijet-enhanced region and W-enhanced region. The weighted fake-factors are then applied to events in the corresponding SRs.

The dominant contribution to the uncertainties in the fake-$\tau_{\text{had-vis}}$ background in the $\tau_{\text{lep}}\tau_{\text{had}}$ channel originates from the statistical uncertainty in the individual fake-factors. Minor contributions arise from uncertainties in the fractional size of the multijet contribution to the fake-$\tau_{\text{had-vis}}$ background and the statistical uncertainty in the anti-ID regions.

5.5 Systematic uncertainties

Before the fit to obtain final results is performed, we need to introduce systematic uncertainties, which affect our measurement. They can be grouped into three main categories: theoretical uncertainties in signal, theoretical uncertainties in background, and experimental uncertainties.

The theoretical uncertainties are related to the cross-section predictions and the event modelling with MC generators. The experimental uncertainties are related to the simulation of the detector response and to the measurement of background contributions from CRs. A non-negligible source of the systematic uncertainty in this measurement is the MC statistical uncertainty, as the simulated samples are of limited size. In general, the systematic uncertainties affect both the expected signal yields and the shape of $m_{\tau\tau}^{\mathrm{MMC}}$ distributions in the SRs as well as the expected background yields the CRs. All systematic uncertainties are included in the fit model described in the section 5.6.

5.5.1 Theoretical uncertainties in signal

In the fit model, the uncertainty is based on the variation of the number of events predicted per bin in the final $m_{\tau\tau}^{\mathrm{MMC}}$ distribution

$$n_{\mathrm{bin}} = \sigma_{\mathrm{tot}} \times \mathcal{L} \times A \times f_{\mathrm{bin}}, \tag{5.1}$$

where σ_{tot} is the total cross-section, $\mathcal{L}$ is the luminosity, A is the acceptance of the total sample in a SR, f_{bin} is the fraction of events in a certain bin in the resulting distribution.

The theoretical uncertainties for signal processes are evaluated separately for their impact on the total cross-section, on the acceptance in different SRs and on the shape of the $m_{\tau\tau}^{\mathrm{MMC}}$ distribution in each SR. The uncertainty of the total cross-section is treated as uncorrelated to shape and acceptance uncertainties, while shape and acceptance uncertainties from a given source are treated as correlated.

The most important theoretical uncertainties of the SM predictions arise from three sources:

- QCD scale uncertainties due to the missing higher orders in perturbation theory.
- Experimental input parameters uncertainties such as PDFs and the value of the strong interaction coupling constant α_S.
- Non-perturbative parts of the calculation (underlying event and hadronisation).

We follow the recommendations provided by the LHC Higgs Cross-Section Working Group (LHCHXSWG) [31] to estimate uncertainties in the Higgs boson production cross-sections, in particular, QCD scale uncertainties, PDF and α_S uncertainties.

For the VBF and VH production cross-sections, the QCD scale uncertainties are estimated by varying the renormalisation μ_R and factorisation μ_F scales by the factor of two around the nominal value.

For ggF production, a trivial variation of the factorisation and renormalisation scales is not sufficient. This approach underestimates the final uncertainties due to the accidental cancellations. Therefore, QCD scale uncertainties for ggF need a specific treatment. Following the LHCHXSWG recommendations, we introduce 9 sources of uncertainties related to the truncation of the perturbative series.
Four sources account for uncertainties in the jet multiplicities due to the missing higher-order corrections:

- 2 sources account for the yield uncertainty due to the factorisation and renormalisation scale variations.
- 2 sources account for the migration uncertainties of ($0 \leftrightarrow 1$) and ($1 \leftrightarrow$ at least 2) jets in the event.

Three sources parameterise the modelling uncertainty in the p_{T}^{H}:

- 2 sources account for the migration uncertainty between the intermediate and high-p_{T} regions of events with at least one jet.
- 1 uncertainty accounts for the top quark mass in the loop corrections, where the difference between the leading order (LO) and next-to-leading order (NLO) predictions is taken as an uncertainty due to missing higher-order corrections.

Two uncertainty sources account for the acceptance uncertainty of the ggF production in the VBF phase space (using an extension of the Stewart–Tackmann method [89, 90]):

- Selecting exactly two jets.
- Selecting at least three jets.

The dominant uncertainties arise from the modelling of the p_{T}^{H} distribution in all SRs, scale variations in the boosted SRs and acceptance uncertainties in the VBF SRs.

The PDF uncertainties are estimated using 30 eigenvector variations and two α_S variations [91]. We estimate the uncertainties related to the simulation of the underlying event, hadronisation and parton shower (UEPS) by comparing the acceptance from two models. In particular, we use the default UEPS model from Pythia and an alternative UEPS model from Herwig. An uncertainty of the branching ratio of the $H \to \tau\tau$ decay is 1% [92] and it affects the signal rates. All theoretical uncertainties are correlated across SRs.

5.5.2 Theoretical uncertainties in backgrounds

Except for the $Z \to \tau\tau$ background, we do not consider theoretical uncertainties of other simulated background processes, as their impact is small compared to the uncertainties of the $Z \to \tau\tau$ and fake background.

For the $Z \to \tau\tau$ background, we consider the uncertainties from the missing higher-order QCD corrections, the PDF parametrisation, parton-shower modelling and underlying-event modelling. $Z \to \tau\tau$ overall normalisation is correlated across the three analysis channels and constrained separately in the VBF and boosted SRs, more details in Section 5.6.

We consider the variations related to the aforementioned uncertainties in the event migration within an analysis channel ('loose' ↔ 'tight'), in the $m_{\tau\tau}^{\mathrm{MMC}}$ shape and in the relative acceptance changes between the three analysis channels. All these uncertainties are uncorrelated between the VBF and boosted SRs. Additionally, we treat uncertainties arising from the missing higher-order QCD corrections and the PDF parametrisation as uncorrelated between the three analysis channels. The largest contribution arises from the uncertainties related to the jet-to-parton matching uncertainty (CKKW matching uncertainties) [93].

The parton-shower and underlying-event modelling uncertainties are evaluated by the SHERPA generator. The impact of these and other modelling uncertainties such, as LO/NLO precision comparison for leading jets on the $Z \to \tau\tau$ background, is studied in an alternative sample. This sample is simulated using MADGRAPH generator [94] at the leading order interfaced to the PYTHIA UEPS model.

5.5.3 Experimental uncertainties

Particle candidate reconstruction includes several stages of calibration which result in a number of sources of experimental systematic uncertainties. We estimate these uncertainties following the recommendations provided by the combined performance groups.

The dominant experimental uncertainties in this measurement are related to the jet and $\tau_{\text{had-vis}}$ reconstruction, while the impact of the electron- and muon-related uncertainties [74, 95, 75] is small.

Luminosity and pileup uncertainties

The uncertainty of the measured integrated luminosity [96, 97] is determined by dedicated luminosity detectors adjacent to the ATLAS detector. This uncertainty affects the number of predicted signal and background events, except for the processes which are normalised to data. In this measurement, we combine 2015 and 2016 datasets with $\sqrt{s} = 13\,\text{TeV}$, so we need to consider the uncertainty due to the pileup reweighting process as well.

Energy scale and resolution uncertainties

In general, the measurement and correction of the energy and momentum scales for reconstructed particles provides a source of uncertainty.

To obtain the jet energy scale (JES) and its uncertainty we combine the information from test-beam data, LHC collision data and simulation [98]. We factorise the uncertainties from the JES measurements into eight components. Additionally, we consider the uncertainties related to jet flavour, pileup corrections, η-dependence and high-p_{T} jets.

The JER [99] uncertainty is particularly important for this measurement. The low resolution of jets leads to the large smearing of $E_{\text{T}}^{\text{miss}}$, which is further propagated to the $m_{\tau\tau}^{\text{MMC}}$ distribution. In order to improve the ability of our fit model to describe the data, we parametrise JER into 11 uncorrelated components rather than a single uncertainty.

The uncertainties of the TES [82] are determined by fitting the Z boson mass in $Z \to \tau\tau$ events, which are reconstructed using the $\tau_{\text{had-vis}}$. For $\tau_{\text{had-vis}}$ with $p_{\text{T}} > 50\,\text{GeV}$, we also consider the uncertainties based on the modelling of the calorimeter response to single particles [100]. The uncertainties of electron [101] and muon [74] energy scales are considered as well.

Systematic uncertainties of the energy scales of all objects influence the reconstructed $E_{\text{T}}^{\text{miss}}$ and we need to recalculate the $E_{\text{T}}^{\text{miss}}$ after applying each variation. We take into account the scale uncertainty of $E_{\text{T}}^{\text{miss}}$ caused by the energy in the calorimeter cells not associated with physics objects [84]. The $E_{\text{T}}^{\text{miss}}$ resolution uncertainty is derived from the energy resolution uncertainties of each of the $E_{\mathrm{T}}^{\mathrm{miss}}$ terms and the modelling of the pileup and its impact on the soft term.

Efficiency uncertainties

Efficiency uncertainties incorporate the uncertainties in efficiencies for triggering, object reconstruction and identification. We correct simulated events for differences in efficiencies between the data and the simulationm and propagate the associated uncertainties through the analysis.

The main contribution arises from the uncertainties of the $\tau_{\text{had-vis}}$ identification and reconstruction efficiency [102], the trigger efficiency and the uncertainty of the rate at which an electron is misidentified as $\tau_{\text{had-vis}}$ [82]. The uncertainties for identification and reconstruction for electrons [101] and muons [74] are considered as well; however, their impact is rather small. We also consider uncertainties in the efficiency to pass the JVT and forward JVT requirements [103, 81]. Efficiencies of the flavour tagging uncertainties are measured in dedicated calibration analyses [104] and result in uncorrelated components.

5.6 Statistical model and fit procedure

After the optimisation of the signal event selection, estimation of the background contributions and systematic uncertainties, we want to look at the final fit results. However, first we have to build a model for statistical hypothesis testing. The overview of the statistical analysis techniques used in the high-energy physics was provided in Section 4. In this section, we describe some specifications of the statistical model and the fit procedure used in $H \to \tau\tau$ cross-section measurement.

The statistical model is built with the `HistFactory` software package in the `RooFit/RooStat` framework [105]. It is determined by the probability density functions of the binned $m_{\tau\tau}^{\mathrm{MMC}}$ distributions expected in each event category. The $m_{\tau\tau}^{\mathrm{MMC}}$ is chosen as it provides a good discrimination power between the signal and the background processes and it is sensitive to the Higgs boson mass as well.

The histograms of the expected $m_{\tau\tau}^{\mathrm{MMC}}$ distributions are composed of the individual contributions from the ggF, VBF, VH and $t\bar{t}H$ signal processes and the $Z \to \tau\tau$, fake and other remaining background processes. These individual contributions are called samples.

The fit model encodes the three analysis channels and two categories as well as the correlations between signal and background processes and systematic uncertainties. It incorporates more than 200 NPs related to the statistical and systematic uncertainties and to the normalisation of the background contributions measured in the CRs. The maximum-likelihood fit on data is performed using the $m_{\tau\tau}^{\mathrm{MMC}}$ distributions in 13 SRs and the event yields in 6 CRs, in order to extract POI which probe the $H \to \tau\tau$ production.

The fit with a single POI measures either the total cross-section of the $H \to \tau\tau$ production or its signal strength. In this case, we measure the contribution from the four Higgs boson production processes, with their relative contributions assumed to be as predicted by the SM. The total cross-section of the $H \to \tau\tau$ production processes is defined as $\sigma_{H\to\tau\tau} = \sigma_H \times \mathcal{B}(H \to \tau\tau)$, where $\mathcal{B}(H \to \tau\tau)$ is the $H \to \tau\tau$ branching fraction. Signal strength is defined as $\mu_{H\to\tau\tau} = \sigma_{H\to\tau\tau}/\sigma_{H\to\tau\tau}^{\mathrm{SM}}$, where $\sigma^{\mathrm{SM}}_{H\to\tau\tau}$ stands for the SM prediction. The value $\mu_{H\to\tau\tau} = 0$ corresponds to the absence of signal, whereas the value $\mu_{H\to\tau\tau} = 1$ corresponds to the signal as predicted by the SM.

In the cross-section measurement with two POIs, we measure separately the ggF and VBF production modes and the VH and $t\bar{t}H$ production cross-sections are set to their SM predicted values.

For the small contribution from the $H \to WW^*$ decays in our measurement, we assume the SM predictions for the production cross-section and branching ratio.

The CRs are employed to constrain normalisations of the major background contributions. For this purpose, we use single-bin histograms containing the number of events in the corresponding CRs. In the case of simulated background components, the NFs compare the background normalisation with values determined from their theoretical cross-sections. The background normalisations are considered either free-floating with constraints given by the corresponding CRs or fixed to their MC predictions.

The $Z \to \tau\tau$ background is correlated across the three analysis channels resulting in two NFs, one per inclusive category. The $Z \to \tau\tau$ normalisation is constrained by data in the $m^{\mathrm{MMC}}_{\tau\tau}$ distribution of the SRs. The absolute event yields of the $Z \to \ell\ell$ CRs constrain the normalisation of simulated $Z \to \ell\ell$ events in the $\tau_{\mathrm{lep}}\tau_{\mathrm{lep}}$ channel using two NFs in the fit (one per inclusive category). The normalisation of the simulated top background is constrained by the absolute event yields in the respective CRs in the $\tau_{\mathrm{lep}}\tau_{\mathrm{lep}}$ and $\tau_{\mathrm{lep}}\tau_{\mathrm{had}}$ channels, using in total four NFs in the fit. Furthermore, we introduce one NF for the data-driven fake-$\tau_{\text{had-vis}}$ background in the $\tau_{\mathrm{had}}\tau_{\mathrm{had}}$ channel, which scales the event yield of the template of events that fail the opposite-charge requirement (see Section 5.4.4).

After applying all selection criteria many of the samples have low statistics, which may cause issues in dealing with the shape component of the NPs. For example, in the case of small systematic variations, the corresponding upward ($+1\sigma$) and downward (-1σ) systematic variations or varied $m^{\mathrm{MMC}}_{\tau\tau}$ shapes might be dominated by statistical noise. Inserting such noise into the fit could cause instabilities and allow for incorrect and unintentional variation of the NPs. For this reason, we developed methods to systematically prune and smooth the shape component of the systematic uncertainties in order to suppress the noisy components without accidentally removing genuine and significant shape variations, all happening before they enter the fit.

To simplify the fit model and ensure its stability, we apply several criteria to reduce the number of NPs (for each shape systematic considered), which do not impact the likelihood model:

- *Symmetrisation:* The histograms entering the fit might contain bins with both the upward and downward systematic variations lying in the same direction (up or down) with respect to the nominal value. This effect might cause incorrect behaviour of the fit. Thus, the larger of the two variations (with respect to the nominal) is mirrored about the nominal in order to produce a symmetric variation (in that particular bin). An example of the input variation on which the symmetrisation is applied is shown in the left plot in Figure 5.2.

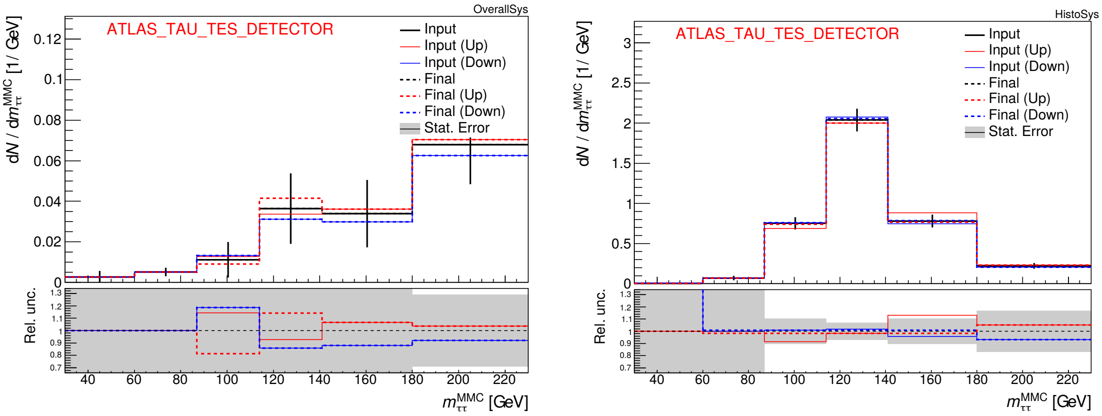

Figure 5.2: Examples of the systematic uncertainties where the symmetrization (left) and smoothing (right) procedure is applied. The solid (dashed) lines correspond to the input (output) variations in the invariant mass of a pair of tau leptons $m_{\tau\tau}^{\rm MMC}$ distribution for one component of tau energy scale (TES) uncertainty in $t\bar{t}H$ (left) and WH (right) sample in the boosted signal region of the $\tau_{\rm lep}\tau_{\rm had}$ channel.

- *Smoothing:* We use smoothing procedure [106] to remove the occasional large local fluctuations in the $m_{\tau\tau}^{\rm MMC}$ distributions. It is performed on the ratio between the variation and the nominal as this minimises the artefacts which can be created by the smoothing. An example of the input variation on which the smoothing is applied is shown in the right plot in Figure 5.2.

Similarly, we define four pruning criteria:

- *Overall normalisation:* We consider the NPs affecting the normalisation only if the total integral of either the upward or the downward variation differs from the integral of the nominal histogram by more than 0.5%.
- *Statistical uncertainty:* The shape variation of a nominal histogram with the large statistical uncertainty tends to make falsely large shape variation due to the statistical fluctuation (especially bin-to-bin migration). Therefore, we prune away the shape systematics if the statistical uncertainty of the integral (total yield) is greater than 0.1.
- χ^2 *test:* We perform a χ^2 test between the upward and the downward variations with respect to the nominal. This test is done separately for each potential shape systematic NP and for each sample. The statistical uncertainty considered in this calculation is only the largest of the nominal or varied one, rather than both (since they are typically very strongly correlated). We keep the shape component of the NP if the result of the reduced χ^2 test is greater than 0.1, for at least one of the upward or downward fluctuated shapes. Otherwise, the shape variation is considered as non-significant for the given background sample, and the shape component of the NP is not used in the fit. However, the corresponding normalisation component of a given NP is still considered.
- *Significance testing:* For the shape systematic of background processes we further consider whether the variation has a significant effect in at least one bin. We define a variation significance as $S_i = |u_i - d_i|/\sigma_i^{tot}$, with u_i (d_i)

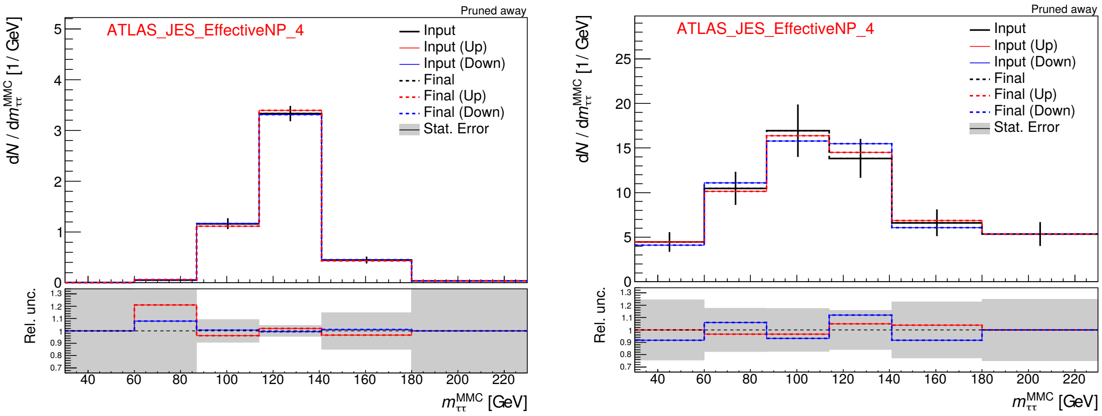

Figure 5.3: Examples of the systematic uncertainties which are pruned away and thus not included in the fit. The solid (dashed) lines correspond to the input (output) variations in the invariant mass of a pair of tau leptons $m_{\tau\tau}^{\mathrm{MMC}}$ distribution for one component of jet energy scale (JES) uncertainty in WH (left) and Top (right) sample in the boosted signal region of the $\tau_{\mathrm{lep}}\tau_{\mathrm{had}}$ channel.

being the upward (downward) variation in the bin i and σ_i^{tot} is the statistical uncertainty on the nominal value. If no bin has $S_i > 0.1$, we remove the shape component of the NP.

We optimised the pruning thresholds mentioned above in such a way that they do not prune genuine variations. The examples of the systematic uncertainties which are pruned away and thus not included in the fit are shown in in Figure 5.3. We checked the signal significance by scanning each threshold and made sure that the significance does not artificially increase due to the pruning procedure removing the real shape systematics. If the variation is negative then the value of the variation is set to a tiny positive value (10^{-6}).

The full fit model is summarised in Figure 5.4. It should be noted that we use both 2015 and 2016 data, and common merged histograms are used for these two datasets.

The fit model cross checks, the final fit results, the uncertainty breakdowns and postfit figures, are obtained with the `WSMaker` script collection [107].

Initially, the fit is tested against an Asimov dataset [63], which is built from the sum of the expected signal and background contributions in place of the observed data and therefore the estimators for all NPs are equal to their true values. This dataset is used to assess the stability of the fit model and it provides an expected sensitivity of the measurement as well. The input variations of some NPs might be overestimated and if the observed data have power to constrain them, we observe smaller $\pm 1\sigma$ band than the one expected in the negative-log likelihood distribution from the fit to an Asimov dataset. We have performed several fit tests using the Asimov dataset to scrutinise the constrained NPs. Furthermore, to study the behaviour of the fit model in real data before looking at the region where we expect the Higgs boson's signal, we have provided a fit of the $m_{\tau\tau}^{\mathrm{MMC}}$ distribution restricting its range below 100 GeV in all SRs (low mass fit). The fit model scrutiny using the aforementioned approaches is described in Section 5.8.

Following the validation of the fit to Asimov data and the fit in the low mass region, the fit to the real data is performed and the obtained results are presented in the next section.

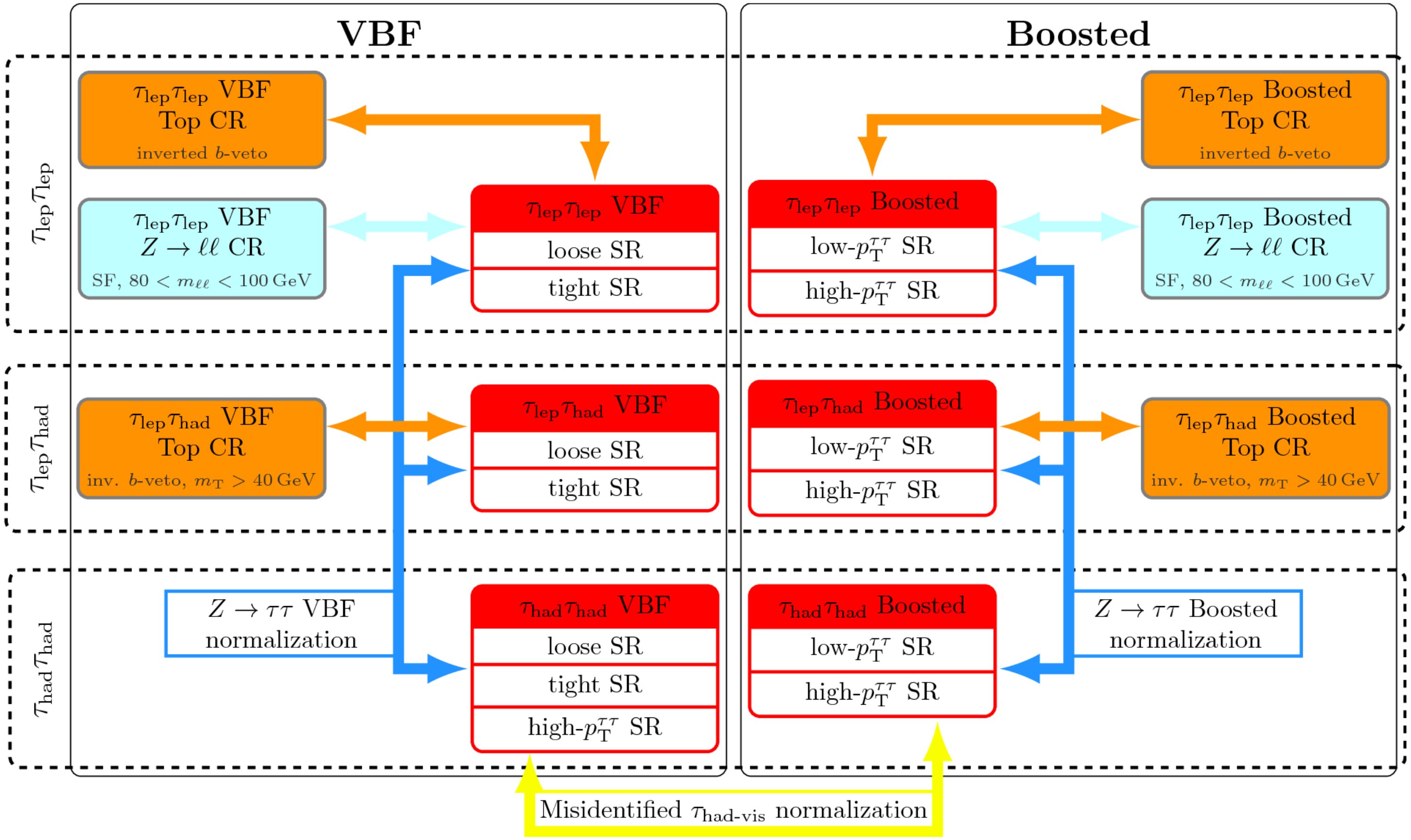

Figure 5.4: A schematic summary of the fit model. All regions which are used directly in the combined fit are indicated. They are grouped by topology (VBF and boosted) and analysis category ($\tau_{lep}\tau_{lep}$, $\tau_{lep}\tau_{had}$, $\tau_{had}\tau_{had}$). The arrows indicate the free-floating normalisation factors which are acting on various regions. The colour indicates which background component normalisation they represent: top (orange), $Z \to \ell\ell$ (light blue), $Z \to \tau\tau$ (blue) and fakes in the $\tau_{had}\tau_{had}$ channel (yellow). Other background components are using the normalisation as predicted by MC. The data-driven fake estimates in the $\tau_{lep}\tau_{lep}$ and $\tau_{lep}\tau_{had}$ channels come with an absolute prediction of their yield and thus do not have free-floating normalisation factor in the fit.

5.7 Results

The aim of the analysis presented in this thesis is to measure the signal strength and the production cross-section of the Higgs boson in $H \to \tau\tau$ decay channel. Furthemore, we determine total cross-sections in the $H \to \tau\tau$ decay channel separately for the VBF and ggF production.

For all measurements we consider the same set of the systematic uncertainties; however, for the cross-section measurements we do not include theoretical uncertainties related to the measured signal cross-sections.

Theoretical uncertainties are kept correlated as described in Section 5.5. The experimental uncertainties are fully correlated and the background modelling uncertainties uncorrelated across the two categories, with the exception of the NFs as described in Section 5.4.

In figures in this section, the analsysis channels $\tau_{\mathrm{lep}}\tau_{\mathrm{lep}}$, $\tau_{\mathrm{lep}}\tau_{\mathrm{had}}$ and $\tau_{\mathrm{had}}\tau_{\mathrm{had}}$ are labelled as ‘ll’, ‘lh’ and ‘hh’, respectively.

5.7.1 Observed and expected significance

The analysis selection as well as the binning of the $m_{\tau\tau}^{\mathrm{MMC}}$ distribution in the SRs were optimised using the Asimov dataset to provide the best expected significance.

The observed (expected) significance of the signal excess relative to the background-only hypothesis computed from the likelihood fit is 4.4 (4.1) standard deviations, compatible with a SM Higgs boson with a mass of 125 GeV. The expected significances are obtained from the fit to an Asimov dataset, which was created during the fit by the fitting program.

Table 5.6: The observed and expected signal significance obtained from the combined fit with the three analysis channels and the two categories is labelled as ‘Combination’. The combination of all VBF (boosted) signal regions across all channels is indicated by ‘VBF’ (‘Boosted’). Obtained results from the individual fit in each channel and category are shown as well.

Fitted region	Observed significance [σ]	Expected significance [σ]
Combination	4.40	4.14
VBF	2.57	2.75
Boosted	3.21	2.85
$\tau_{\mathrm{lep}}\tau_{\mathrm{lep}}$	2.20	1.20
$\tau_{\mathrm{lep}}\tau_{\mathrm{had}}$	2.44	2.63
$\tau_{\mathrm{had}}\tau_{\mathrm{had}}$	2.21	2.88
$\tau_{\mathrm{lep}}\tau_{\mathrm{lep}}$ VBF	1.29	0.83
$\tau_{\mathrm{lep}}\tau_{\mathrm{had}}$ VBF	1.64	1.68
$\tau_{\mathrm{had}}\tau_{\mathrm{had}}$ VBF	1.39	1.78
$\tau_{\mathrm{lep}}\tau_{\mathrm{lep}}$ BST	1.48	0.68
$\tau_{\mathrm{lep}}\tau_{\mathrm{had}}$ BST	1.91	1.86
$\tau_{\mathrm{had}}\tau_{\mathrm{had}}$ BST	1.25	1.83

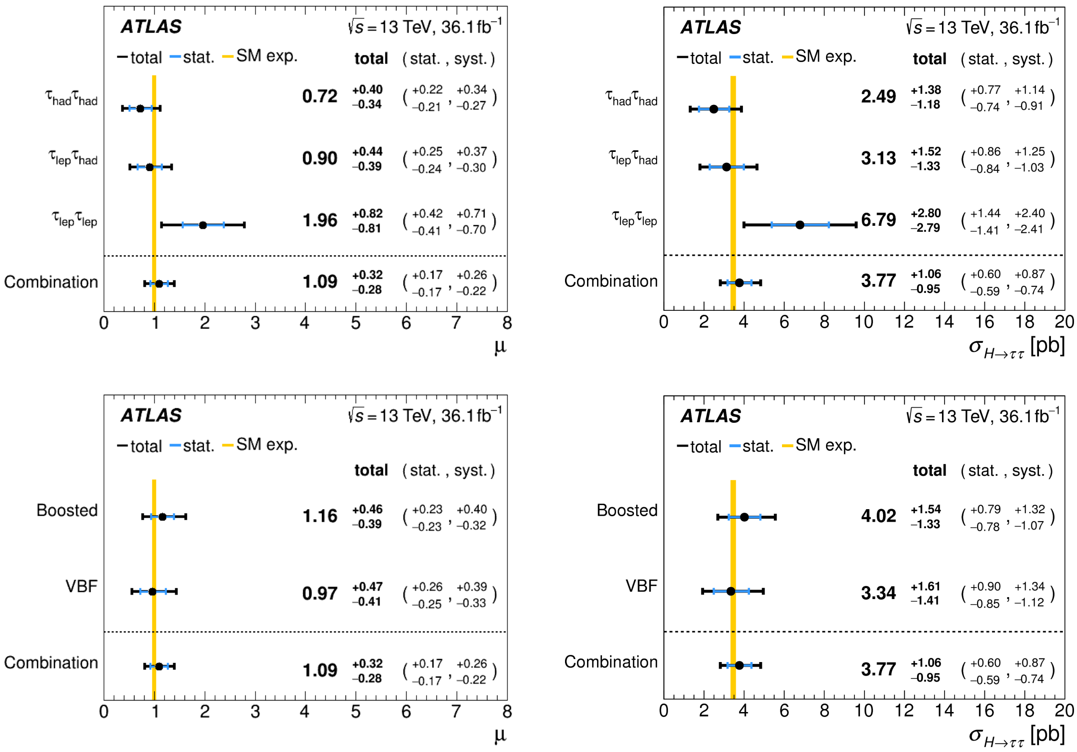

Figure 5.5: The measured values for $\mu_{H\to\tau\tau}$ (left) and $\sigma_{H\to\tau\tau}$ (right) when only the data of individual channels (top) or individual categories (bottom) are used. The result from the combined fit is shown as well. The total $\pm1\sigma$ uncertainty in the measurement is indicated by the black error bars, with the individual contribution from the statistical uncertainty in blue. The theory uncertainty in the predicted signal strength (cross-section) is shown by the yellow band.

Table 5.6 shows the expected and observed signal significances for the combined fit and fits per individual channels and categories.

Combination with Run 1 dataset

We combine the aforementioned result with the result of the search for $H \to \tau\tau$ decay using Run 1 dataset [9]. The observed (expected) significance amounts to 6.4 (5.4) standard deviations. In this combination, all NPs are treated as uncorrelated between the two analyses as they used different techniques for the dominant $Z \to \tau\tau$ background estimation. In particular, in the measurement presented in this thesis $Z \to \tau\tau$ is estimated from MC simulation, while in the Run 1 analysis [9], the embedding technique [88] was used.

5.7.2 Measured signal strength and cross-section

As mentioned earlier, we consider four Higgs boson production processes: VBF, ggF, VH and $t\bar{t}H$, whose relative contributions are assumed as predicted by the SM. The signal strength calculated by the fit is evaluated to be

$$\mu_{H\to\tau\tau} = 1.09\,^{+0.17}_{-0.17}\,(\text{stat.})\,^{+0.26}_{-0.22}\,(\text{syst.})\,^{+0.16}_{-0.11}\,(\text{theory syst.}).$$

Table 5.7: Summary of different sources of uncertainty on the signal strength $\mu_{H\to\tau\tau}$ and cross-section $\sigma_{H\to\tau\tau}$ measurement in terms of absolute values. The uncertainties are grouped to individual categories according to their origin. 'All but normalisations' correspond to the fit in which all experimental and theoretical uncertainties are included, but the normalisation factors are excluded.

Parameter of interest Central value	$\mu_{H\to\tau\tau}$ 1.091	$\sigma_{H\to\tau\tau}/\sigma^{\mathrm{SM}}_{H\to\tau\tau}$ 1.089
Set of nuisance parameters	Uncertainty	Uncertainty
Total	$+0.315/-0.279$	$+0.307/-0.275$
DataStat	$+0.175/-0.171$	$+0.174/-0.171$
FullSyst	$+0.263/-0.220$	$+0.253/-0.215$
All normalisations	$+0.069/-0.050$	$+0.069/-0.048$
Ztt normalisation	$+0.056/-0.036$	$+0.055/-0.033$
All but normalisations	$+0.250/-0.206$	$+0.240/-0.201$
Jets MET	$+0.124/-0.100$	$+0.122/-0.100$
BTag	$+0.037/-0.030$	$+0.037/-0.027$
Electron / Muon	$+0.013/-0.010$	$+0.013/-0.010$
Tau	$+0.048/-0.033$	$+0.048/-0.032$
Pileup reweighting	$+0.013/-0.004$	$+0.012/-0.003$
Fake estimation	$+0.045/-0.041$	$+0.045/-0.041$
Luminosity	$+0.036/-0.026$	$+0.036/-0.026$
Theory unc. (Signal)	$+0.161/-0.106$	$+0.146/-0.095$
Theory unc. (Ztautau)	$+0.044/-0.035$	$+0.043/-0.035$
MC stat	$+0.120/-0.109$	$+0.118/-0.108$

The measured value of the total cross-section is

$$\sigma_{H\to\tau\tau} = 3.77\,^{+0.60}_{-0.59}\,(\mathrm{stat.})\,^{+0.87}_{-0.74}\,(\mathrm{syst.})\,\mathrm{pb},$$

which is consistent with the SM prediction of $\sigma^{\mathrm{SM}}_{H\to\tau\tau} = 3.46 \pm 0.13\,\mathrm{pb}$ [92]. Results of the fit when only the data of an individual channel or of an individual category are used, are shown in Figure 5.5. Also shown is the result from the combined fit and the theoretical uncertainty in predicted signal strength or cross-section.

Table 5.7 shows the best-fit value for the signal strength (top) and cross-section (bottom) and the breakdown of uncertainties on these measurements in terms of absolute values. In the breakdown tables the NPs are grouped to several categories according to their origin.

The main contribution to the final uncertainty originates in the systematic uncertainties. The biggest contribution among the systematic uncertainties arises from the jet related uncertainties and signal theoretical uncertainties.

5.7.3 Nuisance parameters constraints

The NPs are profiled in order to minimise the negative-log likelihood function. After the fit, the NPs can end up constrained or pulled from their expected

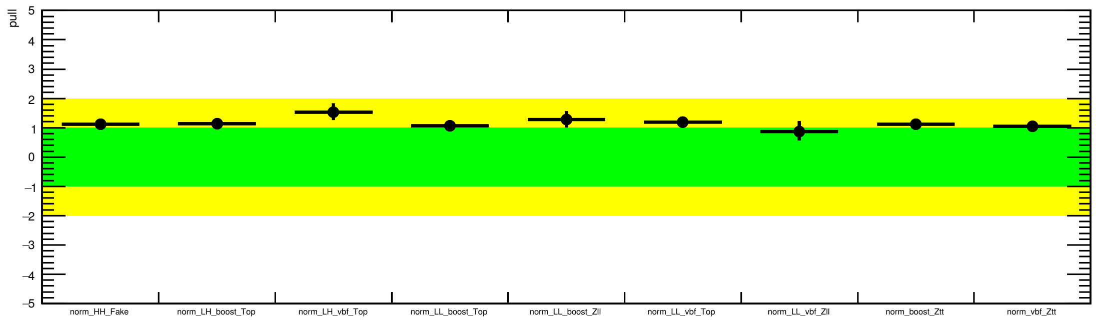

Figure 5.6: Postfit values of all normalisation factors entering the combined fit.

(central) value. Constraints indicate the favourability of data to be able to assess the size of the variation. Pulls indicate that the data is distributed closer to the $\pm 1\sigma$ variation rather than to the nominal value.

The postfit values of NFs are shown in Figure 5.6 and listed in Table 5.8. The postfit constraint of $Z \to \tau\tau$ NF is ±9% in the VBF category and ±5% in the boosted category. The normalization of top background is constrained to ±30% in the $\tau_{\mathrm{lep}}\tau_{\mathrm{had}}$ VBF top CR and less than ±10% in the other top CRs. For $Z \to \ell\ell$ NF the constraint in the $\tau_{\mathrm{lep}}\tau_{\mathrm{lep}}$ channel amounts to ±40% in the VBF category and to ±25% in the boosted category. In other channels the contribution from $Z \to \ell\ell$ events is not significant and it is normalised to its theoretical cross-section. The event yield of multijet background in the $\tau_{\mathrm{had}}\tau_{\mathrm{had}}$ channel is constrained by data to ±15% in the SRs.

Figure 5.7 shows constraints and pulls of all NFs and NPs, except for the MC statistical uncertainties. Table which enumerates the postfit value for each NP can be found in Appendix C. The set of NPs with the postfit constraint less than 0.75 of the prefit uncertainty or pulls from the central value greater than 0.5 are shown in Figure 5.8. We can group NPs with significant constraints or pulls into several categories: $Z \to \tau\tau$ theory, $E_{\mathrm{T}}^{\mathrm{miss}}$, jet and tau-related NPs, and misidentified tau related NPs. We have carefully scrutinised NPs with significant constraints (pulls) and investigated their origin using the Asimov dataset (low mass fit) before actually looking at measured data. Several of these investigations are described in Section 5.8.

Study of the jet related uncertainties

The ATLAS jet energy resolution (JER) measurement is performed in well-balanced dijet events. The results of the comparison between data and MC simulations are used in the analyses performed by the ATLAS collaboration. They can be parametrised in two ways:

- A single NP encapsulating all the mismodelling effects.
- 11 NPs resulting from a principle component analysis.

As the analysis presented in this thesis is highly sensitive to the JER uncertainties, the two proposed strategies were investigated. The 11 NPs approach is preferred as it provides a more accurate parameterisation of the observed difference between data and MC simulation.

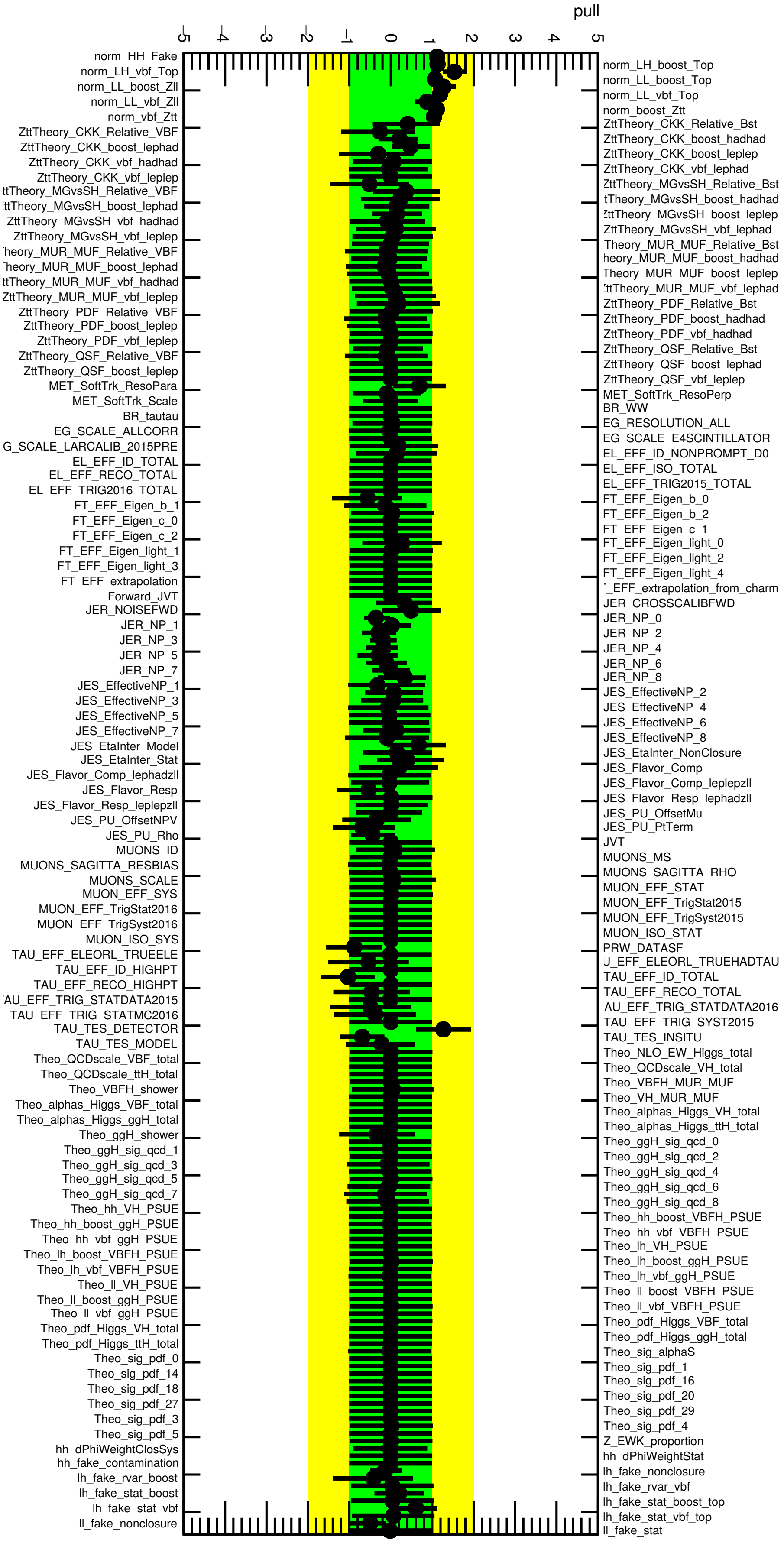

Figure 5.7: Constraints and pulls of all the nuisance parameters except for those related to MC statistics.

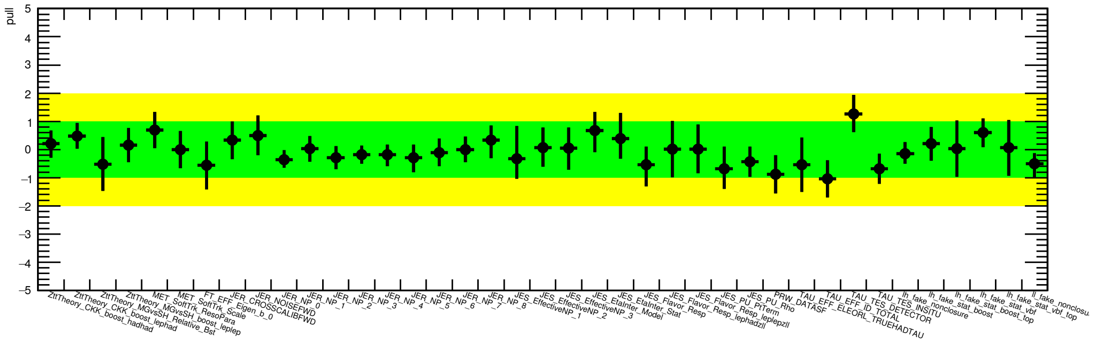

Figure 5.8: Constraints and pulls of the nuisance parameters for which the constraint is less than 0.75 of the prefit uncertainty or pulls greater than 0.5.

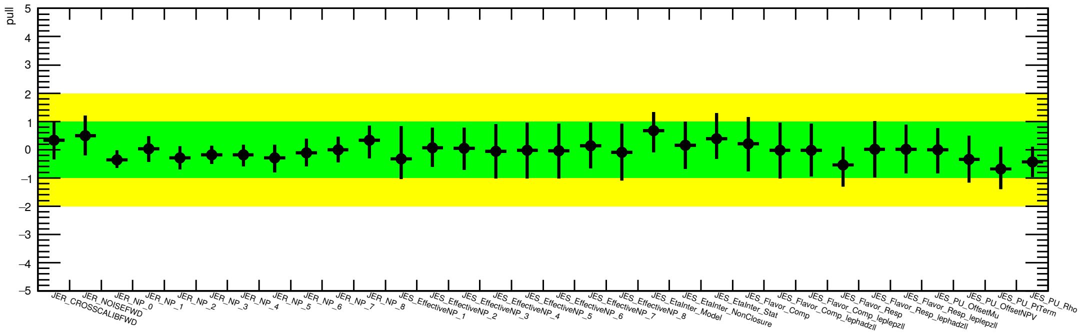

Figure 5.9: Constraints and pulls of the jet related nuisance parameters.

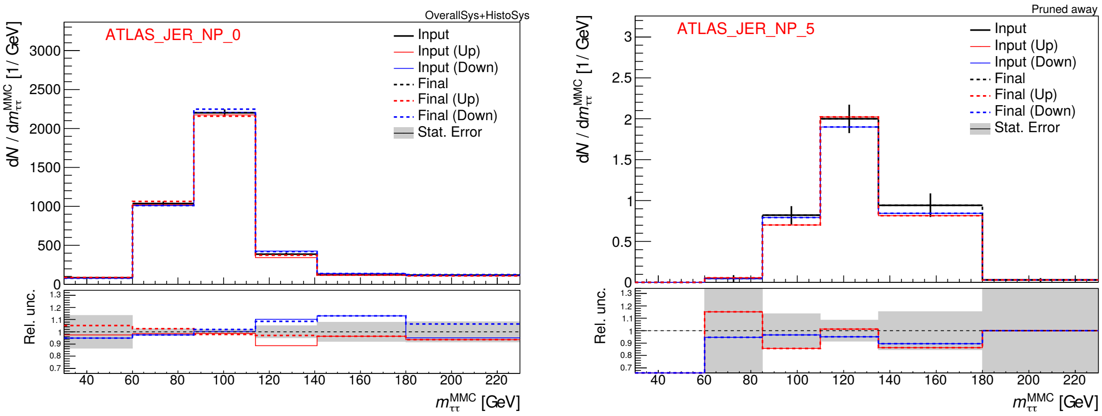

Figure 5.10: Examples of input and output variations for one component of the jet energy resolution (JER) uncertainty. The solid (dashed) line corresponds to the input (output) variations in the invariant mass of a pair of tau leptons $m_{\tau\tau}^{\mathrm{MMC}}$ distribution in $Z \to \tau\tau$ sample in the boosted signal region (left) and ggH sample in the VBF signal region (right) of the $\tau_{\mathrm{lep}}\tau_{\mathrm{had}}$ channel.

Table 5.8: Normalisation factors for the background components which have their normalisation constrained using data in the fit, including all statistical and systematic uncertainties, but without uncertainties in total simulated cross-sections extrapolated to the selected phase space. Systematic uncertainties are the dominant contribution to the normalisation factor uncertainties. Also shown are the analysis channels to which the normalisation factors are applied.

Background	Channel	Normalisation factors	
		VBF	Boosted
$Z \to \ell\ell$ (CR)	$\tau_{\text{lep}}\tau_{\text{lep}}$	$0.88^{+0.34}_{-0.30}$	$1.27^{+0.30}_{-0.25}$
Top (CR)	$\tau_{\text{lep}}\tau_{\text{lep}}$	1.19 ± 0.09	1.07 ± 0.05
Top (CR)	$\tau_{\text{lep}}\tau_{\text{had}}$	$1.53^{+0.30}_{-0.27}$	1.13 ± 0.07
Fake-$\tau_{\text{had-vis}}$ (data-driven)	$\tau_{\text{had}}\tau_{\text{had}}$	1.12 ± 0.12	
$Z \to \tau\tau$ (fit in each SR)	$\tau_{\text{lep}}\tau_{\text{lep}}$,$\tau_{\text{lep}}\tau_{\text{had}}$,$\tau_{\text{had}}\tau_{\text{had}}$	$1.04^{+0.10}_{-0.09}$	1.11 ± 0.05

We studied the behaviour of the analysis categorisation and the $m_{\tau\tau}^{\text{MMC}}$ variable when we vary the jet energy resolution following the recommendations of the ATLAS JetEtmiss working group.

The calculation of the $m_{\tau\tau}^{\text{MMC}}$ variable depends explicitely on the $E_{\text{T}}^{\text{miss}}$ reconstruction and on the number of jets with $p_{\text{T}} > 25\,\text{GeV}$. Consequently, one expects to see an impact from a variation of the JER uncertainty on the $m_{\tau\tau}^{\text{MMC}}$ calculation. Especially in the boosted $Z \to \tau\tau$ topology with at least one additional jet, a variation of the jet p_{T} translates directly in $E_{\text{T}}^{\text{miss}}$. This results in two effects:

- The $E_{\text{T}}^{\text{miss}}$ acts as an input to the $m_{\tau\tau}^{\text{MMC}}$ calculation and thus the shift of the $E_{\text{T}}^{\text{miss}}$ towards higher values, leads to a shift of the $m_{\tau\tau}^{\text{MMC}}$ distribution towards higher values and it shifts the Z boson peak.

- Moreover, since we apply a cut on $E_{\text{T}}^{\text{miss}}$, the JER leads to an increase of accepted events with lower nominal $E_{\text{T}}^{\text{miss}}$ values. This translates into a shift of the $m_{\tau\tau}^{\text{MMC}}$ distribution to higher values.

The NPs related to the jet energy resolution are significantly constrained, as shown in Figure 5.9. Figure 5.10 shows the examples of the input and output variations for the JER_NP_0 (left) and JER_NP_5 (right) component of the JER uncertainty.

Figure 5.11 illustrates the profile negative-log likelihood scans of the 9 JER NPs in the combined fit as well as in the individual fit per analysis channel. As shown, the constraints and the pulls do not come from a single channel.

The constraints of the JER NPs in the combined fit are driven by the measurement of the Z boson peak position, which is apparently more sensitive than the standard ATLAS recommendations (at least in the studied phase space region). The same conclusion is true for the jet energy scale (JES) uncertainties. This analysis would benefit from updated recommendations with reduced jet uncertainties.

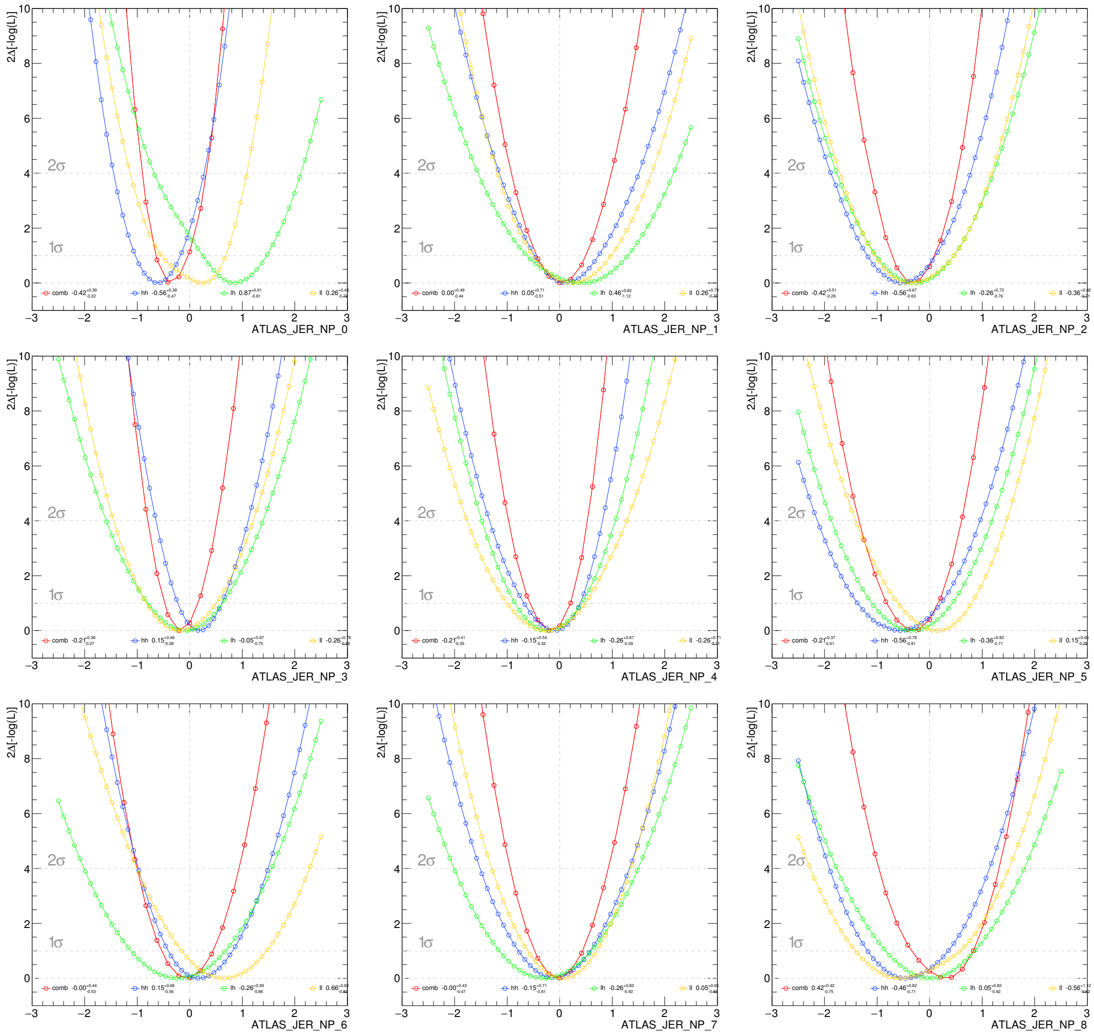

Figure 5.11: ATLAS_JER nuisance parameters profile scans. Red curve corresponds to the combination of the analysis channels, while blue, green and yellow curves correspond to $\tau_{\rm had}\tau_{\rm had}$, $\tau_{\rm lep}\tau_{\rm had}$ and $\tau_{\rm lep}\tau_{\rm lep}$ channels, respectively.

Study of the uncertainties on the hadronic tau efficiency and energy scale

As illustrated in Figure 5.12 and shown in Table 5.9, NPs related to the uncertainties on the hadronic tau efficiency and energy scale (labelled as TAU_EFF_ID, TAU_TES) are pulled in the fit of the full $m_{\tau\tau}^{\rm MMC}$ spectrum. Similar behaviour of these NPs is observed in the fit of the low $m_{\tau\tau}^{\rm MMC}$ range described in Section 5.8.2.

TAU_EFF_ID_TOTAL, TAU_TES_DETECTOR and TAU_TES_INSITU NPs exhibit the most severe pulls. However, these NPs have a limited impact on the POI as they are ranked 28th, 95 and 67 respectively, see section about the NPs ranking below. The first two of these NPs are significantly more pulled in the combined fit than in the individual fit performed in the $\tau_{\rm lep}\tau_{\rm had}$ and $\tau_{\rm had}\tau_{\rm had}$ channels. In addition, the $Z \rightarrow \tau\tau$ NFs differ by $\approx 1.5\sigma$ between the $\tau_{\rm lep}\tau_{\rm had}$ and $\tau_{\rm had}\tau_{\rm had}$ channel fits. In the combined fit, we consider a single $Z \rightarrow \tau\tau$ NF per category across the three decay channels. The difference in the NFs noticed in the fit on the individual channel is absorbed by TAU_EFF_ID_TOTAL and

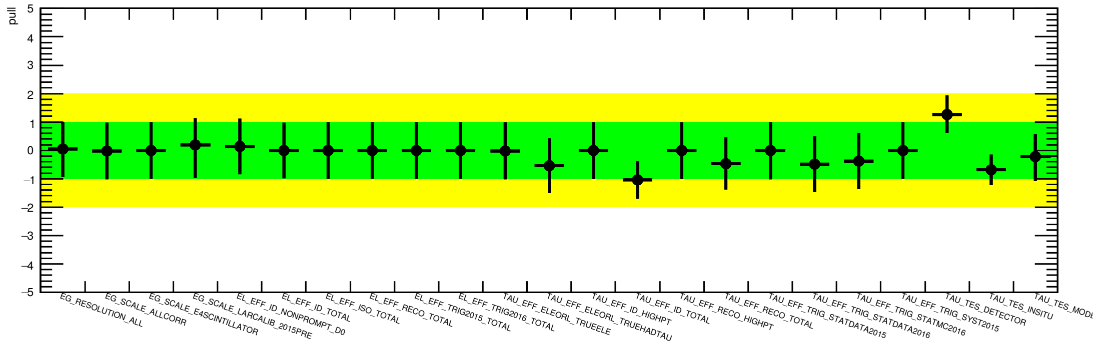

Figure 5.12: Constraints and pulls of nuisance parameters related to lepton uncertainties.

Table 5.9: Observed and expected ranking and postfit value and uncertainties of the hadronic tau nuisance parameters and the $Z \to \tau\tau$ normalisation factors. This table is made with a $\tau_{\mathrm{had}}\tau_{\mathrm{had}}$ workspace inputs with a wrong implementation of the ggH parton shower uncertainty. The impact of this uncertainty is marginal and the conclusions drawn in this section does not change in any way after its correct implementation.

Ranking Obs.	Ranking Exp.	Nuisance parameter	Combined	Standalone	
			$\tau_{\mathrm{lep}}\tau_{\mathrm{lep}}+\tau_{\mathrm{lep}}\tau_{\mathrm{had}}+\tau_{\mathrm{had}}\tau_{\mathrm{had}}$	$\tau_{\mathrm{lep}}\tau_{\mathrm{had}}$	$\tau_{\mathrm{had}}\tau_{\mathrm{had}}$
16	16	TAU_EFF_ID_TOTAL	$-1.07^{+0.66}_{-0.67}$	$-0.09^{+0.99}_{-0.99}$	$-0.03^{+0.84}_{-0.84}$
38	40	TAU_TES_DETECTOR	$1.25^{+0.67}_{-0.65}$	$0.02^{+1.02}_{-1.02}$	$0.54^{+0.77}_{-0.91}$
45	44	TAU_EFF_RECO_TOTAL	$-0.49^{+0.93}_{-0.92}$	$-0.05^{+0.99}_{-0.99}$	$-0.01^{+0.96}_{-0.96}$
62	25	TAU_TES_INSITU	$-0.72^{+0.53}_{-0.53}$	$-0.04^{+0.78}_{-0.82}$	$-0.59^{+1.02}_{-0.63}$
64	54	TAU_TES_MODEL	$-0.19^{+0.81}_{-0.85}$	$-0.01^{+1.00}_{-1.00}$	$-0.32^{+0.93}_{-0.91}$
87	105	TAU_EFF_ELEORL_TRUEH	$-0.52^{+0.97}_{-0.97}$	$0.01^{+1.00}_{-1.00}$	$0.03^{+0.99}_{-0.99}$
3	3	norm_boost_Ztt	$1.11^{+0.05}_{-0.05}$	$1.04^{+0.09}_{-0.08}$	$0.88^{+0.12}_{-0.10}$
47	52	norm_vbf_Ztt	$1.04^{+0.10}_{-0.09}$	$1.06^{+0.19}_{-0.16}$	$0.81^{+0.17}_{-0.14}$

TAU_TES_DETECTOR NPs. The pull of TAU_TES_INSITU is similar in the combined fit and in the $\tau_{\mathrm{had}}\tau_{\mathrm{had}}$ channel. This parameter is essentially unpulled in the $\tau_{\mathrm{lep}}\tau_{\mathrm{had}}$ channel; however, it is constrained by a factor ≈ 1.5.

In order to understand more the nature of these pulls, we perform two tests in which we split the TAU_EFF_ID_TOTAL NPs:

1. Split into two uncorrelated NPs depending on the p_{T}. The first one affecting hadronic taus with p_{T} below 40 GeV and the second one above 40 GeV;
2. Split into two uncorrelated NPs depending on prongness. One NP for 1-prong taus and one NP for 3-prong taus.

Table 5.10 summarises the result of these tests. The pull of TAU_EFF_ID_TOTAL NP origins in hadronic taus with a p_{T} above 40 GeV. This effect is expected, since the $\tau_{\mathrm{had}}\tau_{\mathrm{had}}$ channel have a very small population of hadronic taus below 40 GeV. Moreover, the pull seems to origin in 1-prong taus which dominates the sample in both $\tau_{\mathrm{lep}}\tau_{\mathrm{had}}$ and $\tau_{\mathrm{had}}\tau_{\mathrm{had}}$ channels. In all the studied scenarios, the pulls and constraints on the TES NPs are similar.

Table 5.10: Postfit values and uncertainties of the hadronic tau nuisance parameters and $Z \to \tau\tau$ normalisation factors when TAU_EFF_ID_TOTAL is split in two NPs probing different p_{T} regime or different prongness. This table is made with a $\tau_{\mathrm{had}}\tau_{\mathrm{had}}$ workspace inputs with a wrong implementation of the ggH parton shower uncertainty. The impact of this uncertainty is marginal and the conclusions drawn in this section does not change in any way after its correct implementation.

Nuisance parameter	Nominal	Split in p_{T}	Split in prongness
TAU_EFF_ELEORL_TRUEELE	$-0.02^{+1.00}_{-1.00}$	$-0.03^{+0.99}_{-0.99}$	$-0.03^{+0.99}_{-0.99}$
TAU_EFF_ELEORL_TRUEHADTAU	$-0.52^{+0.97}_{-0.97}$	$-0.52^{+0.97}_{-0.97}$	$-0.54^{+0.97}_{-0.97}$
TAU_EFF_ID_HIGHPT	$0.00^{+1.00}_{-1.00}$	$0.00^{+1.00}_{-1.00}$	$0.00^{+1.00}_{-1.00}$
TAU_EFF_RECO_HIGHPT	$0.00^{+1.00}_{-1.00}$	$0.00^{+1.00}_{-1.00}$	$0.00^{+1.00}_{-1.00}$
TAU_EFF_RECO_TOTAL	$-0.49^{+0.93}_{-0.92}$	$-0.56^{+0.91}_{-0.90}$	$-0.60^{+0.91}_{-0.90}$
TAU_EFF_TRIG_STATDATA2015	$-0.01^{+1.00}_{-1.00}$	$-0.02^{+1.01}_{-1.00}$	$-0.02^{+1.01}_{-1.00}$
TAU_EFF_TRIG_STATDATA2016	$-0.48^{+0.98}_{-0.98}$	$-0.49^{+0.98}_{-0.98}$	$-0.50^{+0.98}_{-0.98}$
TAU_EFF_TRIG_STATMC2016	$-0.37^{+0.99}_{-0.99}$	$-0.38^{+0.99}_{-0.99}$	$-0.39^{+0.99}_{-0.99}$
TAU_EFF_TRIG_SYST2015	$0.00^{+1.00}_{-1.00}$	$0.00^{+1.00}_{-1.00}$	$0.00^{+1.00}_{-1.00}$
TAU_TES_MODEL	$-0.19^{+0.81}_{-0.85}$	$-0.18^{+0.78}_{-0.84}$	$-0.21^{+0.77}_{-0.85}$
TAU_TES_DETECTOR	$1.25^{+0.67}_{-0.65}$	$1.28^{+0.67}_{-0.66}$	$1.29^{+0.67}_{-0.66}$
TAU_TES_INSITU	$-0.72^{+0.53}_{-0.53}$	$-0.79^{+0.51}_{-0.52}$	$-0.81^{+0.51}_{-0.52}$
TAU_EFF_ID_TOTAL	$-1.07^{+0.66}_{-0.67}$	-	-
TAU_EFF_ID_TOTAL_PTHIGH	-	$-1.13^{+0.74}_{-0.74}$	-
TAU_EFF_ID_TOTAL_PTLOW	-	$-0.07^{+0.98}_{-0.98}$	-
TAU_EFF_ID_TOTAL_1P	-	-	$-1.04^{+0.75}_{-0.76}$
TAU_EFF_ID_TOTAL_3P	-	-	$-0.15^{+0.98}_{-0.98}$
norm_boost_Ztt	$1.11^{+0.05}_{-0.05}$	$1.11^{+0.05}_{-0.04}$	$1.11^{+0.05}_{-0.04}$
norm_vbf_Ztt	$1.04^{+0.10}_{-0.09}$	$1.04^{+0.09}_{-0.09}$	$1.03^{+0.09}_{-0.09}$

5.7.4 Nuisance parameters correlations

The two NPs result (anti-)correlated in the fit when the corresponding variations have similar effect on the $m_{\tau\tau}^{\mathrm{MMC}}$ shape or normalisation. We build the fit model in such a way, that we aim to minimise correlations between the NPs; however, it is not possible to remove them completely. As the fit model includes over 200 NPs, we do not show the full correlation matrix. Figure 5.13 shows a part of the correlation matrix, which consists of the NPs which have a correlation of absolute value of at least 25% with any other NP.

The biggest correlations are observed between the two $Z \to \ell\ell$ NFs in the $\tau_{\mathrm{lep}}\tau_{\mathrm{lep}}$ channel, each of them acting on one analysis category. Similarly, for the two Top NFs acting separately on the two categories in the $\tau_{\mathrm{lep}}\tau_{\mathrm{lep}}$ channel and the two $Z \to \tau\tau$ NFs, which are correlated across all the analysis channels. The correlations between the NFs are caused by the migration of events between the VBF and boosted categories and also by the fact that all the experimental and some of the theory NPs acting on these backgrounds are correlated between the analysis categories (not separated per category). ZttTheory_QSF_Relative_Bst NP is correlated with Ztt_CKK_Relative_Bst NP. Both of these NPs control the event migration between the three analysis channels in the boosted category.

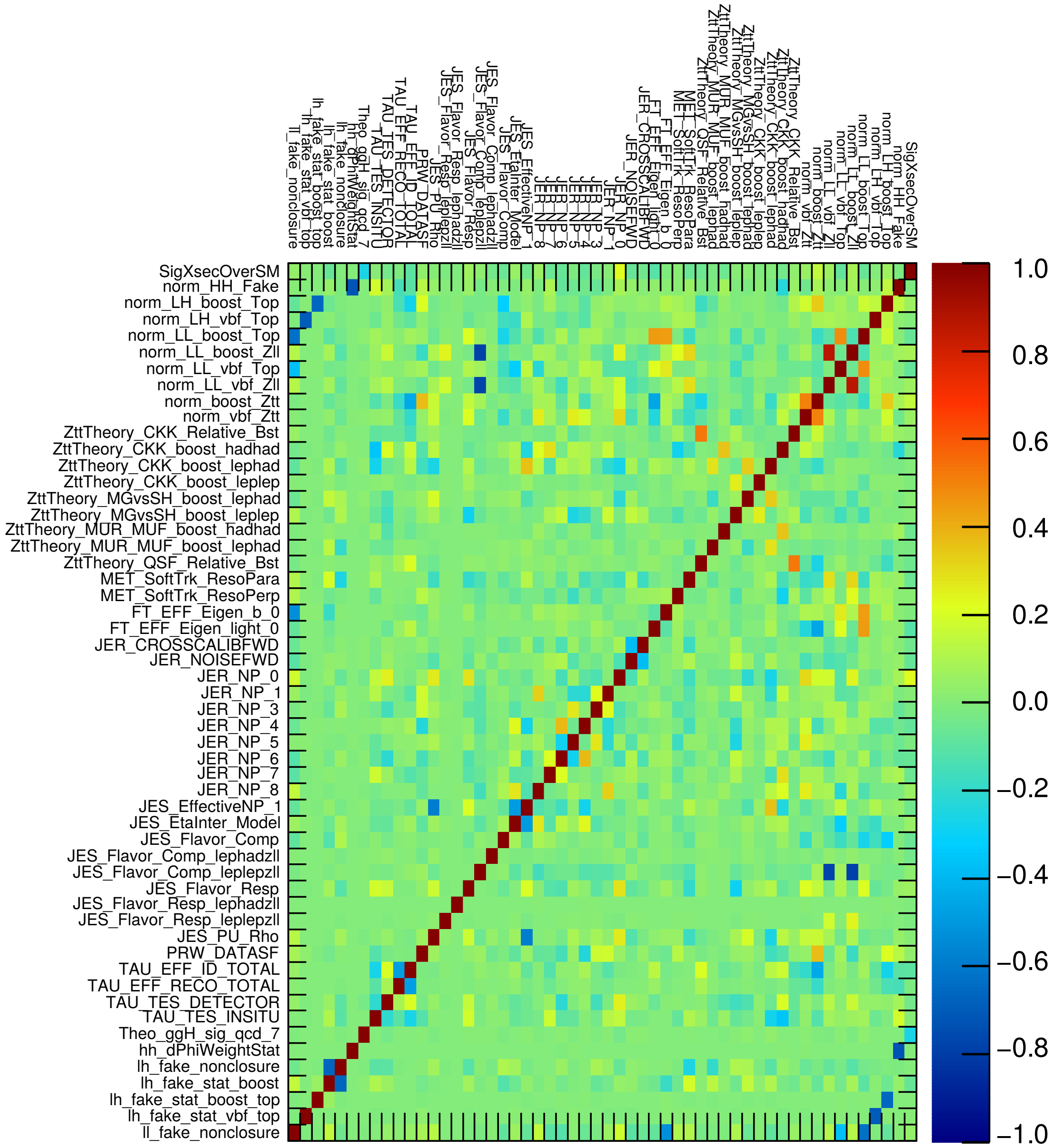

Figure 5.13: The correlation matrix obtained from the combined fit. The matrix contains only the nuisance parameters with correlations whose absolute value is higher than 0.25.

Both FT_EFF_Eigen_b_0 and FT_EFF_Eigen_light_0 NPs are correlated with the Top NF acting on the $\tau_{\text{lep}}\tau_{\text{lep}}$ channel. We understand this effect such that if the b-tagging efficiency changes, yield of the top quark background changes as well and as a result the fit adjusts the corresponding NF.

We observe the biggest anti-correlations between the fake NFs and fake NPs. This effect is expected, since these NFs and NPs act on the fake background and they can change its normalisation. Furthermore, JES_Flavour_Comp_leplepzll NP is anti-correlated with two NFs acting on $Z \to \ell\ell$ background. This anti-correlation is expected, as for the jet flavour composition uncertainty estimation in the $Z \to \ell\ell$ background we used conservative approach. Due to the limited statistics in this sample, we assumed that this background sample contains 50% of quark-originate jets and 50% of gluon-originate jets with 100% uncertainty. For better understanding of the origin of these anti-correlations, we introduce two NPs for the jet flavour composition uncertainty in the $\tau_{\text{lep}}\tau_{\text{lep}}$ and $\tau_{\text{lep}}\tau_{\text{had}}$ channels only acting on the $Z \to \ell\ell$ sample and another NP which acts simultaneously on the other samples of the $\tau_{\text{lep}}\tau_{\text{lep}}$ and $\tau_{\text{lep}}\tau_{\text{had}}$ channel.

5.7.5 Nuisance parameters ranking

To evaluate which NPs have the biggest impact on the POI, we provide so-called NP ranking. We obtain NP ranking from the fit by first minimising the likelihood function with all the NPs free-floating and thus getting the best-fit values for all of them. Then, we provide the fit again with all the NPs fixed to their best-fit values while varying one NP at the time by $\pm 1\sigma$ and check how the value of the POI changes. We repeat the fit for all the NPs.

NP ranking plots show the impact (fractional impact) of systematic uncertainties on $\mu_{H\to\tau\tau}$ ($\sigma_{H\to\tau\tau}$) as computed by the fit. The systematic uncertainties are listed in decreasing order of their impact on POI on the y-axis. The hatched blue and open blue boxes show the variations of POI referring to the top x-axis ($\pm 1\sigma$ impact on the POI). The filled circles, referring to the bottom x-axis, show the pulls of the fitted NPs, i.e. the deviations of the fitted parameters $\hat{\theta}$ from their nominal values θ_0, normalised to their nominal uncertainties $\Delta\theta$. The black lines show the uncertainties of the NPs resulting from the fit. The open circles, also referring to the bottom x-axis, show the values of the fitted normalisation factors.

Ten highly ranked NPs together with their postfit values and impact on the signal strength and total cross-section measurements, are shown in Figure 5.14 and Figure 5.15, respectively. The left plot shows ranking for the combined fit of all analysis channels and SRs, the middle plot for the fit of all channels in the VBF SRs and the right plot for the fit of all channels in the boosted SRs.

The dominant uncertainties are related to the limited number of events in the simulated samples, the jet energy resolution, the $\tau_{\text{had-vis}}$ identification, the missing higher-order QCD corrections to the signal process cross-sections and the normalisations of the $Z \to \tau\tau$ and $Z \to \ell\ell$ backgrounds.

Plots in Figures 5.16 and 5.17 show the ranking for the signal strength and cross-section measurement, respectively. The left, middle and right plot shows the ranking of the NPs with respect to the impact on the POI for a fit on all the SRs in the $\tau_{\text{lep}}\tau_{\text{lep}}$, $\tau_{\text{lep}}\tau_{\text{had}}$ and $\tau_{\text{had}}\tau_{\text{had}}$ channels, respectively.

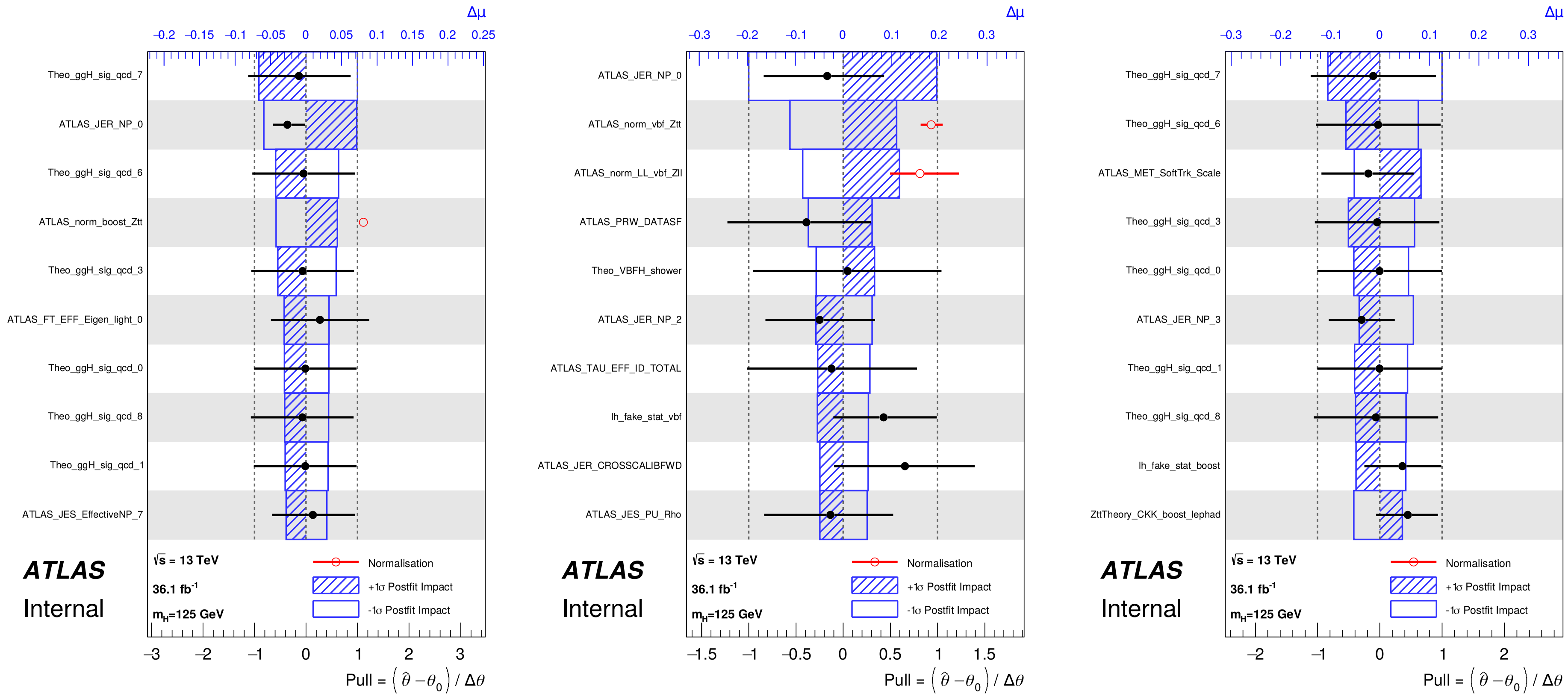

Figure 5.14: Impact of systematic uncertainties on $\mu_{H\to\tau\tau}$ as computed by the fit. Left plot shows the outcome of the combined fit of all channels and signal regions. Middle plot shows the outcome of the fit of all channels in the VBF signal regions. Right plot shows the outcome of the fit of all channels in the Boosted signal regions. The systematic uncertainties are listed in decreasing order of their impact on the parameter of interest (POI) on the y-axis. The hatched blue and open blue boxes show the variations of POI referring to the top x-axis ($\pm 1\sigma$ impact on the POI). The filled circles, referring to the bottom x-axis, show the pulls of the fitted NPs, i.e. the deviations of the fitted parameters $\hat{\theta}$ from their nominal values θ_0, normalised to their nominal uncertainties $\Delta\theta$. The black lines show the uncertainties of the NPs resulting from the fit. The open circles, also referring to the bottom x-axis, show the values of the fitted normalisation factors.

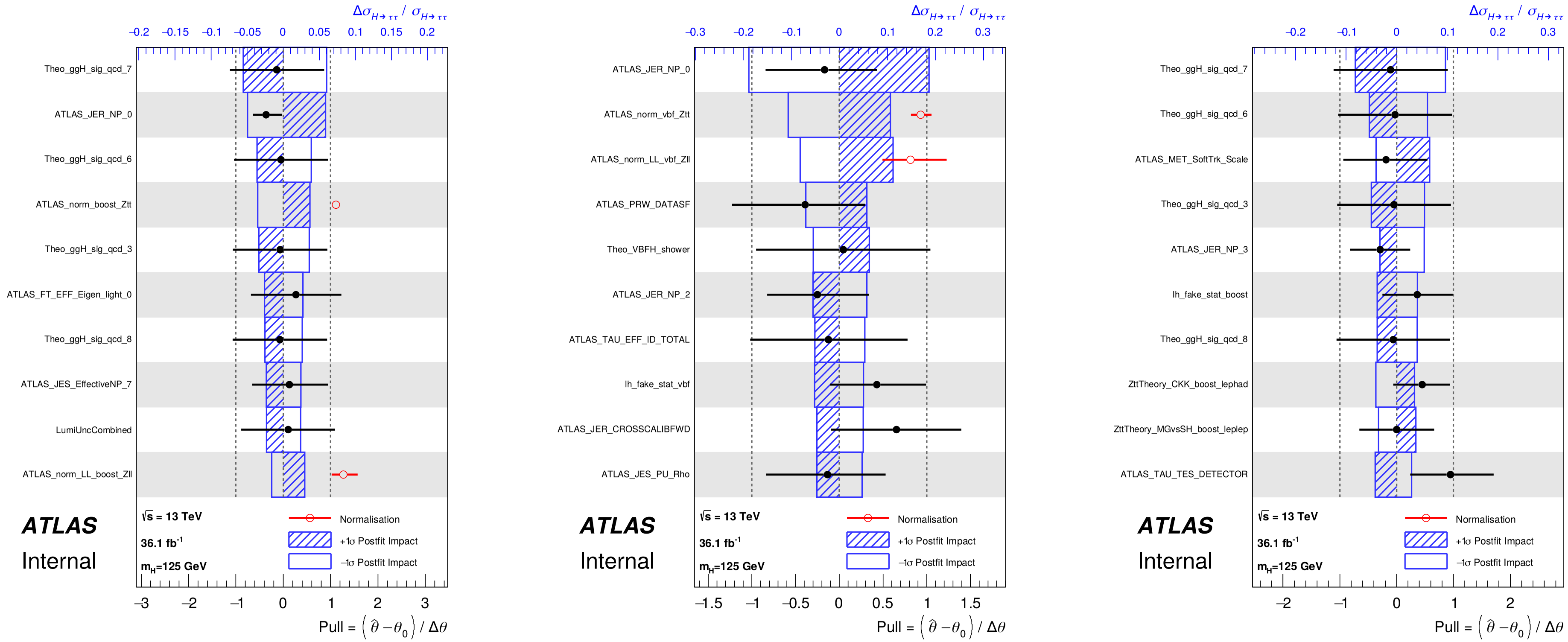

Figure 5.15: Fractional impact of systematic uncertainties on $\sigma_{H\to\tau\tau}$ as computed by the fit. Left plot shows the outcome of the combined fit of all channels and signal regions. Middle plot shows the outcome of the fit of all channels in the VBF signal regions. Right plot shows the outcome of the fit of all channels in the Boosted signal regions. The systematic uncertainties are listed in decreasing order of their impact on the parameter of interest (POI) on the y-axis. The hatched blue and open blue boxes show the variations of POI referring to the top x-axis ($\pm 1\sigma$ impact on the POI). The filled circles, referring to the bottom x-axis, show the pulls of the fitted NPs, i.e. the deviations of the fitted parameters $\hat{\theta}$ from their nominal values θ_0, normalised to their nominal uncertainties $\Delta\theta$. The black lines show the uncertainties of the NPs resulting from the fit. The open circles, also referring to the bottom x-axis, show the values of the fitted normalisation factors.

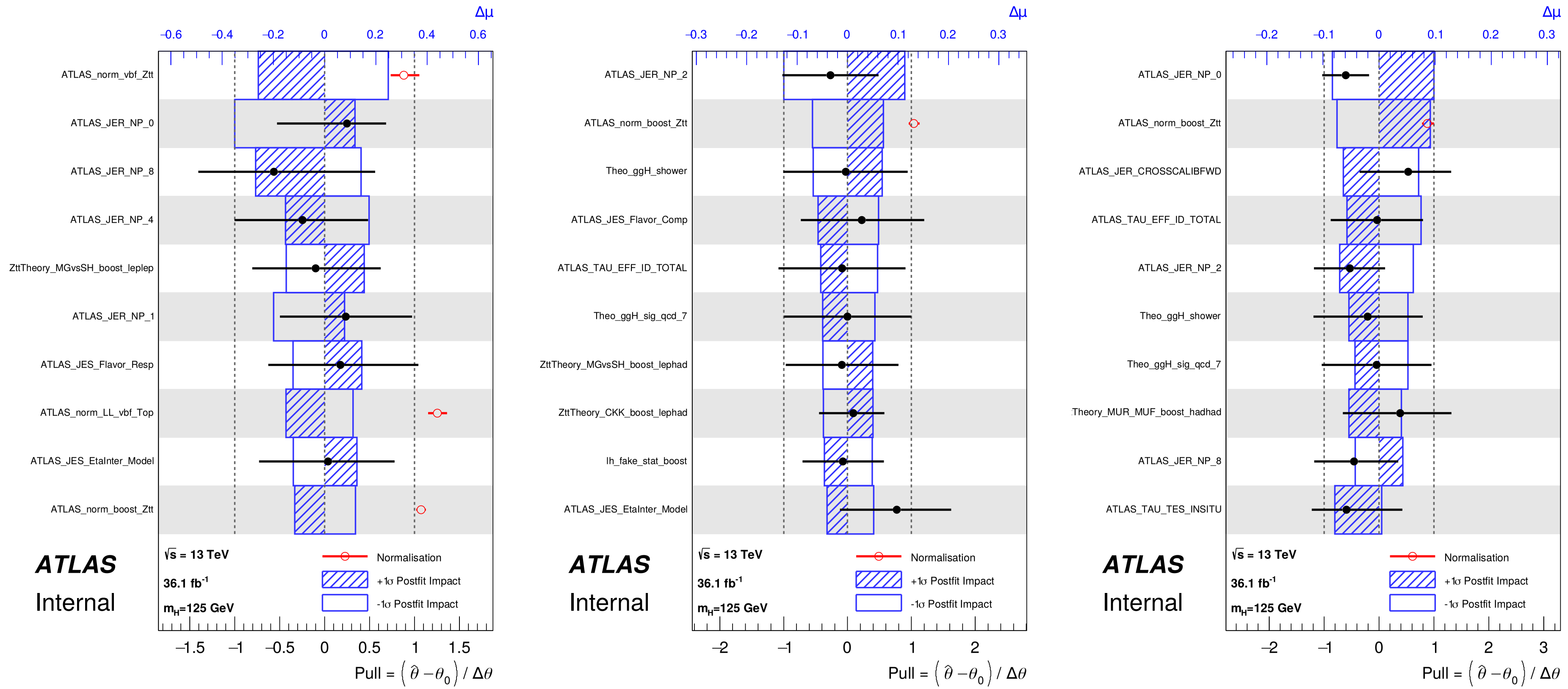

Figure 5.16: Impact of systematic uncertainties on $\mu_{H\to\tau\tau}$ as computed by the fit. Left plot shows the outcome of the fit of all signal regions in the $\tau_{\text{lep}}\tau_{\text{lep}}$ channel. Middle plot shows the outcome of the fit of all signal regions in the $\tau_{\text{lep}}\tau_{\text{had}}$ channel. Right plot shows the outcome of the fit of all signal regions in the $\tau_{\text{had}}\tau_{\text{had}}$ channel. The systematic uncertainties are listed in decreasing order of their impact on the parameter of interest (POI) on the y-axis. The hatched blue and open blue boxes show the variations of POI referring to the top x-axis ($\pm 1\sigma$ impact on the POI). The filled circles, referring to the bottom x-axis, show the pulls of the fitted NPs, i.e. the deviations of the fitted parameters $\hat{\theta}$ from their nominal values θ_0, normalised to their nominal uncertainties $\Delta\theta$. The black lines show the uncertainties of the NPs resulting from the fit. The open circles, also referring to the bottom x-axis, show the values of the fitted normalisation factors.

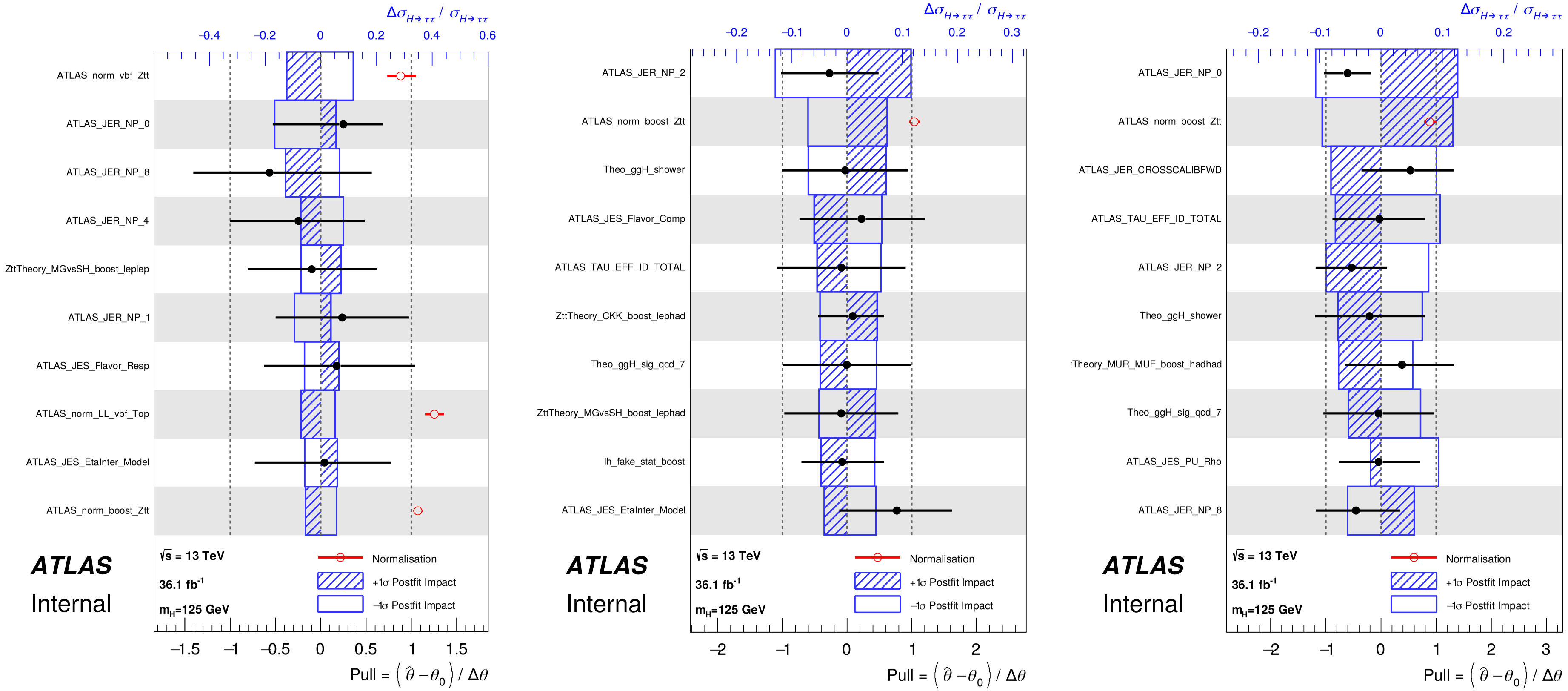

Figure 5.17: Fractional impact of systematic uncertainties on $\sigma_{H\to\tau\tau}$ as computed by the fit. Left plot shows the outcome of the fit of all signal regions in the $\tau_{\text{lep}}\tau_{\text{lep}}$ channel. Middle plot shows the outcome of the fit of all signal regions in the $\tau_{\text{lep}}\tau_{\text{had}}$ channel. Right plot shows the outcome of the fit of all signal regions in the $\tau_{\text{had}}\tau_{\text{had}}$ channel. The systematic uncertainties are listed in decreasing order of their impact on the parameter of interest (POI) on the y-axis. The hatched blue and open blue boxes show the variations of POI referring to the top x-axis ($\pm 1\sigma$ impact on the POI). The filled circles, referring to the bottom x-axis, show the pulls of the fitted NPs, i.e. the deviations of the fitted parameters $\hat{\theta}$ from their nominal values θ_0, normalised to their nominal uncertainties $\Delta\theta$. The black lines show the uncertainties of the NPs resulting from the fit. The open circles, also referring to the bottom x-axis, show the values of the fitted normalisation factors.

5.7.6 Cross-section measured separately in VBF and ggF production modes

The measurement of the overall signal strength or cross-section discussed in the previous sections does not give direct information on the relative contributions of the different production mechanisms to the measurement in $H \to \tau\tau$ decay mode.

Therefore, the cross-sections of different production processes are determined, exploiting the sensitivity offered by the use of the event categories in the three analysis channels. We fit the data separating the vector-boson-mediated VBF processes from the fermion-mediated ggF processes.

We introduce two POIs, $\sigma^{\mathrm{VBF}}_{H\to\tau\tau}$ and $\sigma^{gg\mathrm{F}}_{H\to\tau\tau}$, which scale the SM-predicted rates to those observed, replacing the single POI previously used. The contributions from other Higgs boson production processes are set to their SM predicted values. The two-dimensional 68 % and 95 % confidence level (CL) contours in the plane of the two POIs, are shown in Figure 5.18. The tilt of the contours indicates the strong anti-correlation between these two results (correlation coefficient of -52%).

The plot shows the best-fit value as well as the SM prediction. The best-fit values determined by the fit are

$$\sigma^{\mathrm{VBF}}_{H\to\tau\tau} = 0.38 \pm 0.09\,(\mathrm{stat.})\,^{+0.11}_{-0.09}\,(\mathrm{syst.})\,\mathrm{pb},$$
$$\sigma^{gg\mathrm{F}}_{H\to\tau\tau} = 3.1 \pm 1.0\,(\mathrm{stat.})\,^{+1.6}_{-1.3}\,(\mathrm{syst.})\,\mathrm{pb}.$$

Observed results are in agreement with the SM predictions taken from [92]

$$\sigma^{\mathrm{SM}}_{\mathrm{VBF},H\to\tau\tau} = 0.237 \pm 0.006\,\mathrm{pb},$$
$$\sigma^{\mathrm{SM}}_{gg\mathrm{F},H\to\tau\tau} = 3.05 \pm 0.13\,\mathrm{pb}.$$

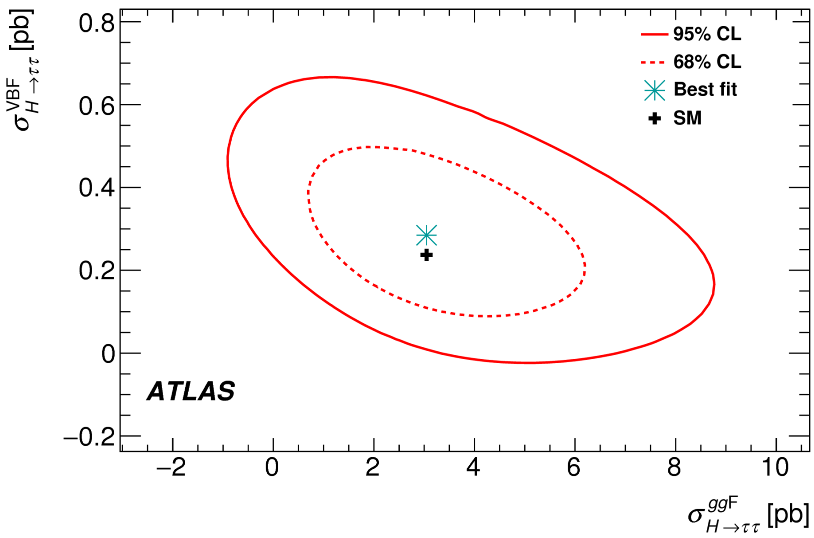

Figure 5.18: Likelihood contours for the combination of all channels in the ($\sigma^{\mathrm{VBF}}_{H\to\tau\tau}$, $\sigma^{gg\mathrm{F}}_{H\to\tau\tau}$) plane. The 68% and 95% confidence level (CL) contours are shown as dashed and solid lines, respectively, for $m_H = 125\,\mathrm{GeV}$. The SM expectation is indicated by a plus symbol and the best fit to the data is shown as a star.

5.7.7 Postfit plots

The $m_{\tau\tau}^{\text{MMC}}$ distributions for the predicted signal plus background are compared with the data in Figure 5.19, separately for the combined SRs of the $\tau_{\text{lep}}\tau_{\text{lep}}$, $\tau_{\text{lep}}\tau_{\text{had}}$ and $\tau_{\text{had}}\tau_{\text{had}}$ channels (left to right). It the left and middle plot in Figure 5.20, the same is shown separately for the combined VBF and boosted SRs, respectively. A weighted combination of the $m_{\tau\tau}^{\text{MMC}}$ distributions in all SRs is shown in the right plot in Figure 5.20. The events are weighted by a factor of $\ln(1 + S/B)$ which enhances the SRs with more significant signal contributions. S/B corresponds to the expected signal-to-background ratio in the corresponding SR.

5.8 Fit tests

5.8.1 Fit results using the Asimov dataset

In this section we use Asimov dataset [63], in which the observed data are replaced by the MC simulation. Asimov dataset allows us to develop and test the fit model and it provides an expected sensitivity as well. The input variations of some NPs might be overestimated and if the observed (Asimov) data have power to constrain them, we observe smaller $\pm 1\sigma$ band in the negative-log likelihood distribution than the one expected.

In figures in this section, the analsysis channels $\tau_{\text{lep}}\tau_{\text{lep}}$, $\tau_{\text{lep}}\tau_{\text{had}}$ and $\tau_{\text{had}}\tau_{\text{had}}$ are labelled as ‘ll’, ‘lh’ and ‘hh’, respectively.

Expected significance

We present the expected significances for each channel, category and for their combination in Table 5.11.

Table 5.11: The expected signal significance obtained from the combined fit with the three analysis channels and the two categories is labelled as ‘Combination’. The combination of all VBF (boosted) signal regions across all channels is indicated by ‘VBF’ (‘Boosted’). Obtained results from the individual fit in each channel and category are shown as well.

Fitted region	Expected significance [σ]
Combination	4.48
VBF	2.95
Boosted	2.93
$\tau_{\text{lep}}\tau_{\text{lep}}$	1.19
$\tau_{\text{lep}}\tau_{\text{had}}$	2.81
$\tau_{\text{had}}\tau_{\text{had}}$	2.84
$\tau_{\text{lep}}\tau_{\text{lep}}$ VBF	0.91
$\tau_{\text{lep}}\tau_{\text{had}}$ VBF	1.94
$\tau_{\text{had}}\tau_{\text{had}}$ VBF	1.84
$\tau_{\text{lep}}\tau_{\text{lep}}$ BST	0.67
$\tau_{\text{lep}}\tau_{\text{had}}$ BST	1.91
$\tau_{\text{had}}\tau_{\text{had}}$ BST	1.85

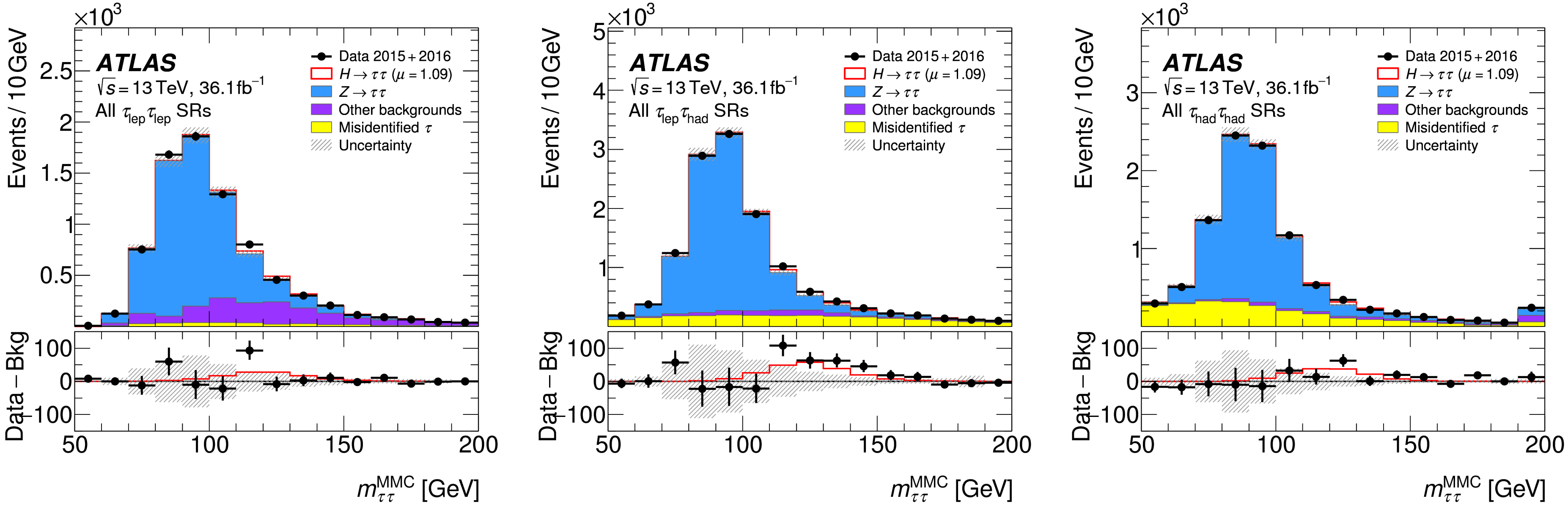

Figure 5.19: Distributions of the reconstructed di-tau invariant mass $m_{\tau\tau}^{\mathrm{MMC}}$ for the sum of all $\tau_{\mathrm{lep}}\tau_{\mathrm{lep}}$ (left), all $\tau_{\mathrm{lep}}\tau_{\mathrm{had}}$ (middle) and all $\tau_{\mathrm{had}}\tau_{\mathrm{had}}$ (right) SRs. The bottom panels show the differences between observed data events and expected background events (black points). The observed Higgs-boson signal ($\mu = 1.09$) is shown with the solid red line. Entries with values that would exceed the x-axis range are shown in the last bin of each distribution. The signal and background predictions are determined in the likelihood fit. The size of the combined statistical, experimental and theoretical uncertainties in the background is indicated by the hatched bands.

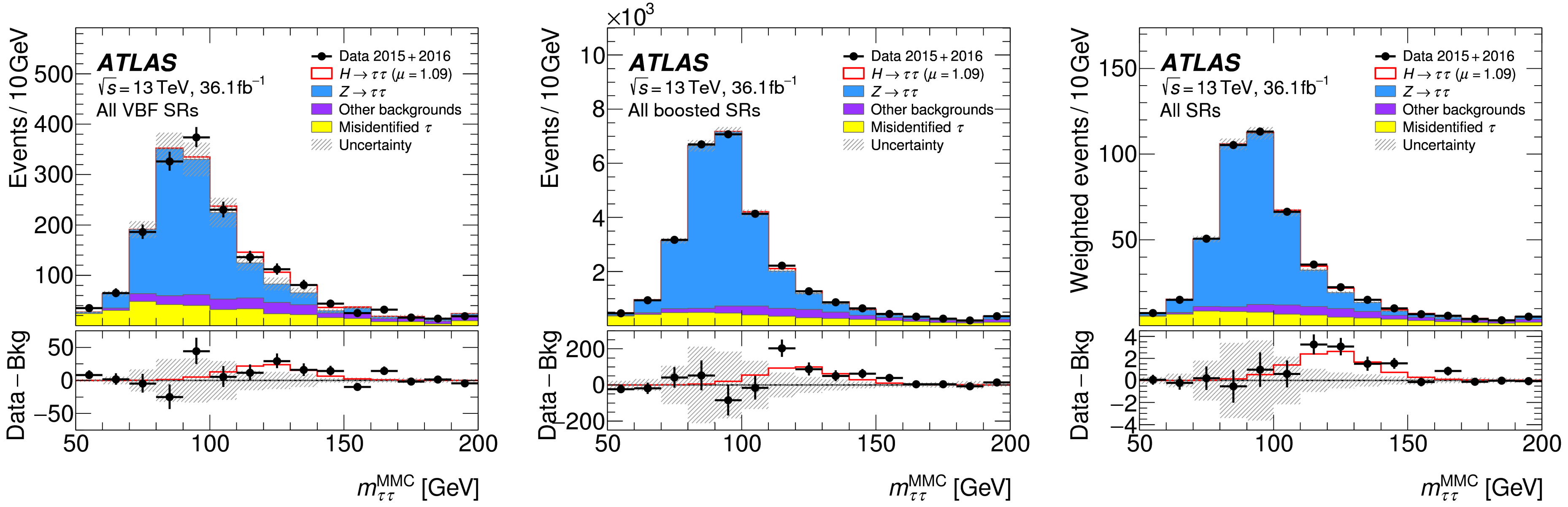

Figure 5.20: The left and middle plots show distribution of the reconstructed di-tau invariant mass $m_{\tau\tau}^{\mathrm{MMC}}$ for the sum of all VBF and all boosted SRs, respectively. The right plot shows the same for all SRs; however, the contributions of the different SRs are weighted by a factor of $\ln(1 + S/B)$, where S and B are the expected numbers of signal and background events in that region, respectively. The bottom panels show the differences between observed data events and expected background events (black points). The observed Higgs-boson signal ($\mu = 1.09$) is shown with the solid red line. Entries with values that would exceed the x-axis range are shown in the last bin of each distribution. The signal and background predictions are determined in the likelihood fit. The size of the combined statistical, experimental and theoretical uncertainties in the background is indicated by the hatched bands.

Expected results and uncertainties on the signal strength measurement

Table 5.12 shows the best-fit value for the signal strength and the breakdown of uncertainties in terms of absolute values. The main contribution to the final uncertainty is coming from the systematic uncertainties. The biggest contribution among the systematic uncertainties arises from the JER uncertainties and signal theoretical uncertainties. Breakdown of uncertainties on the signal strength measurement obtained from the fit to Asimov dataset is similar to the one obtained from the fit to measured data, shown in Figure 5.7.

Nuisance parameters constraints

Figure 5.21 shows the expected constraints of all NFs and NPs except for the MC statistical uncertainties. The postfit central values for all NPs are 0, since we are looking at the Asimov dataset (based on the MC simulation). Figure 5.22 shows only the NPs with the postfit constraint less than 0.75 of the prefit uncertainty. The constraints observed using the Asimov dataset are in good agreement with those observed in the fit on measured data.

Table 5.12: Summary of different sources of uncertainty on the best-fit signal strength in terms of absolute values. The uncertainties are grouped to individual categories according to their origin. 'All but normalisations' correspond to the fit in which all experimental and theoretical uncertainties are included, but the normalisation factors are excluded.

Parameter of interest Central value	$\mu_{H\to\tau\tau}$ 1.000
Set of nuisance parameters	Expected uncertainty
Total	$+0.279/-0.249$
DataStat	$+0.156/-0.153$
FullSyst	$+0.232/-0.197$
All normalisations	$+0.066/-0.046$
Ztt normalisation	$+0.059/-0.036$
All but normalisations	$+0.222/-0.185$
Jets MET	$+0.106/-0.086$
BTag	$+0.029/-0.022$
Electron/Muon	$+0.011/-0.009$
Tau	$+0.058/-0.042$
Pileup reweighting	$+0.014/-0.005$
Fake estimation	$+0.037/-0.034$
Luminosity	$+0.031/-0.022$
Theory unc. (Signal)	$+0.134/-0.087$
Theory unc. (Ztautau)	$+0.051/-0.041$
MC stat	$+0.103/-0.098$

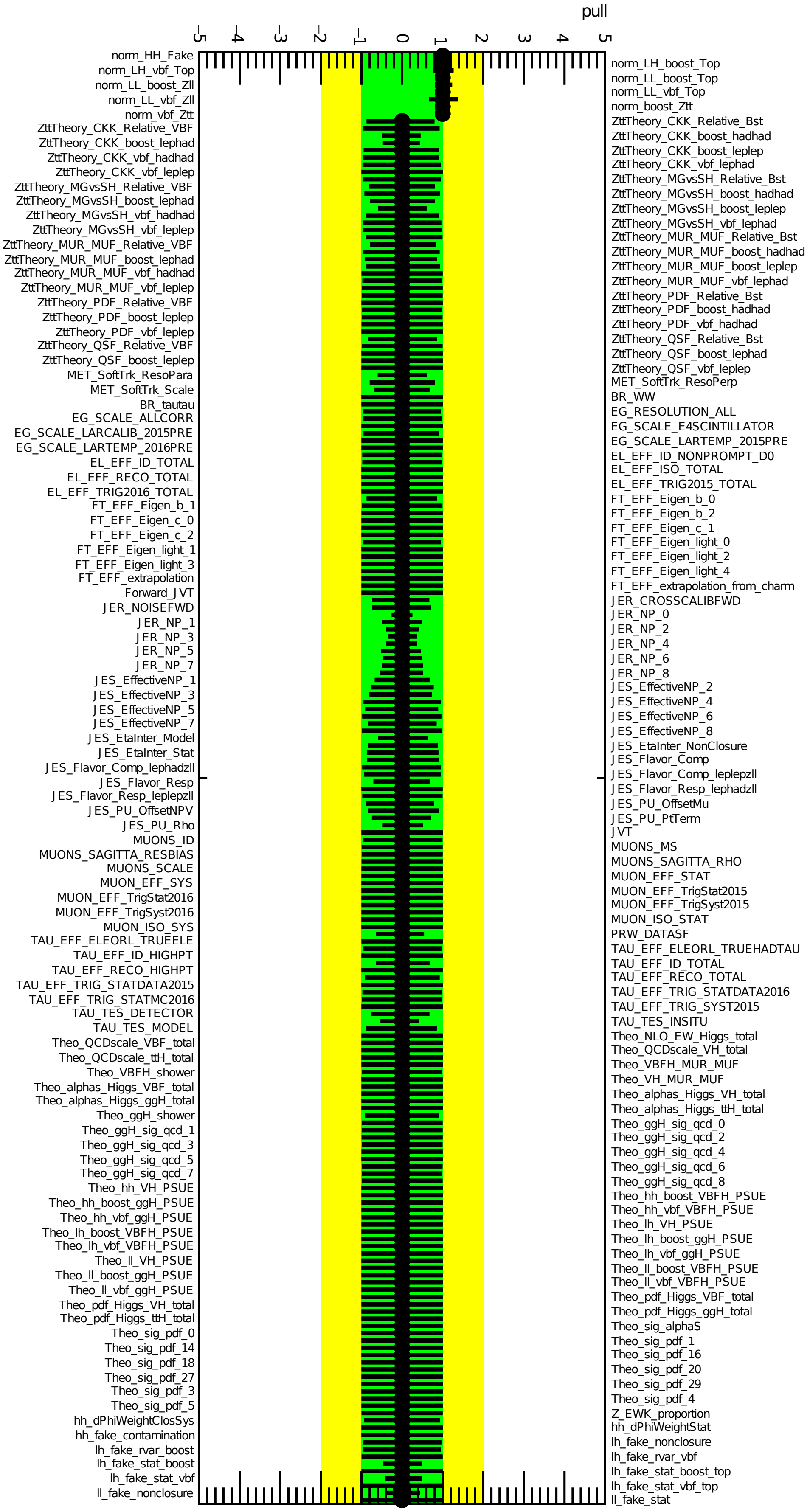

Figure 5.21: Constraints of all the nuisance parameters except for those related to MC statistics.

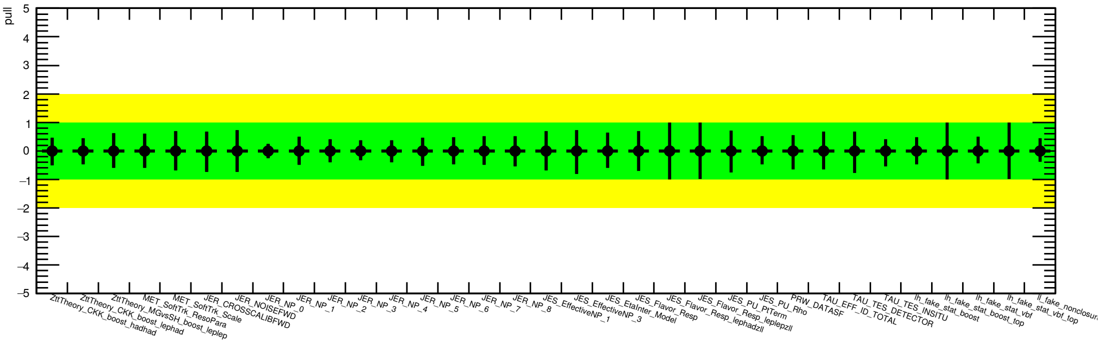

Figure 5.22: Constraints of the nuisance parameters for which the constraint is less than 0.75 of the prefit uncertainty.

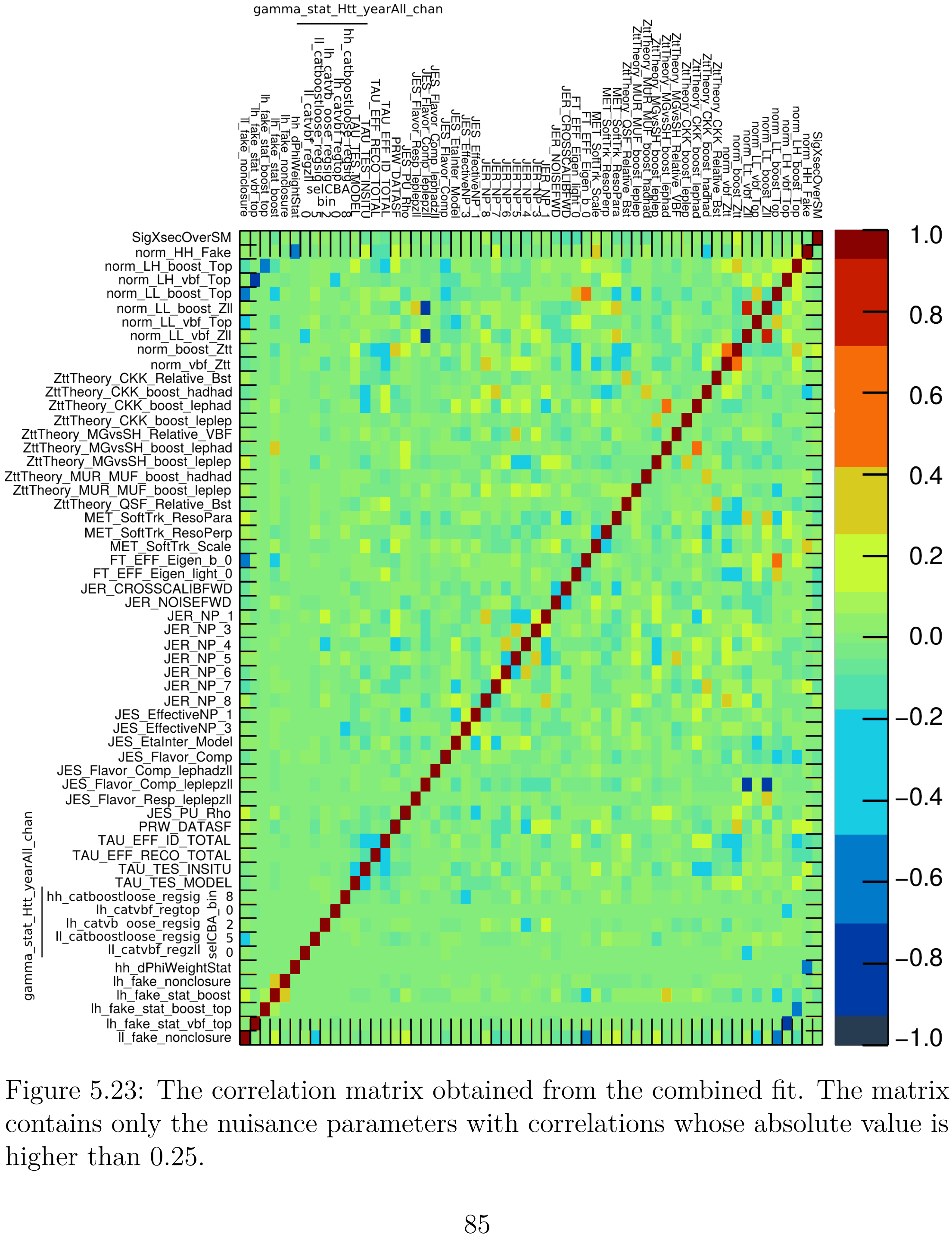

Figure 5.23: The correlation matrix obtained from the combined fit. The matrix contains only the nuisance parameters with correlations whose absolute value is higher than 0.25.

Nuisance parameters correlations

The correlation matrix shown in Figure 5.23 contains only the NPs which have a correlation of absolute value of at least 25% with any other NP. The correlations of the NPs observed using the Asimov dataset are in good agreement with those observed in the fit on measured data, shown in Figure 5.13.

Nuisance parameters ranking

We present the plots which show prefit and postfit impact of the NP on the POI. Ten NPs with the highest impact on the signal strength measurement are shown in Figure 5.24 and 5.25. The left, middle and right plot in Figure 5.24 shows the ranking for the combined fit of all channels and SRs, for the fit of all VBF SR and for the fit of all boosted SRs, respectively. The left, middle and right plot in Figure 5.25 shows the ranking of the NPs with respect to their impact on the signal strength for a fit of all SRs in the $\tau_{\mathrm{lep}}\tau_{\mathrm{lep}}$, $\tau_{\mathrm{lep}}\tau_{\mathrm{had}}$ and $\tau_{\mathrm{had}}\tau_{\mathrm{had}}$ channels, respectively.

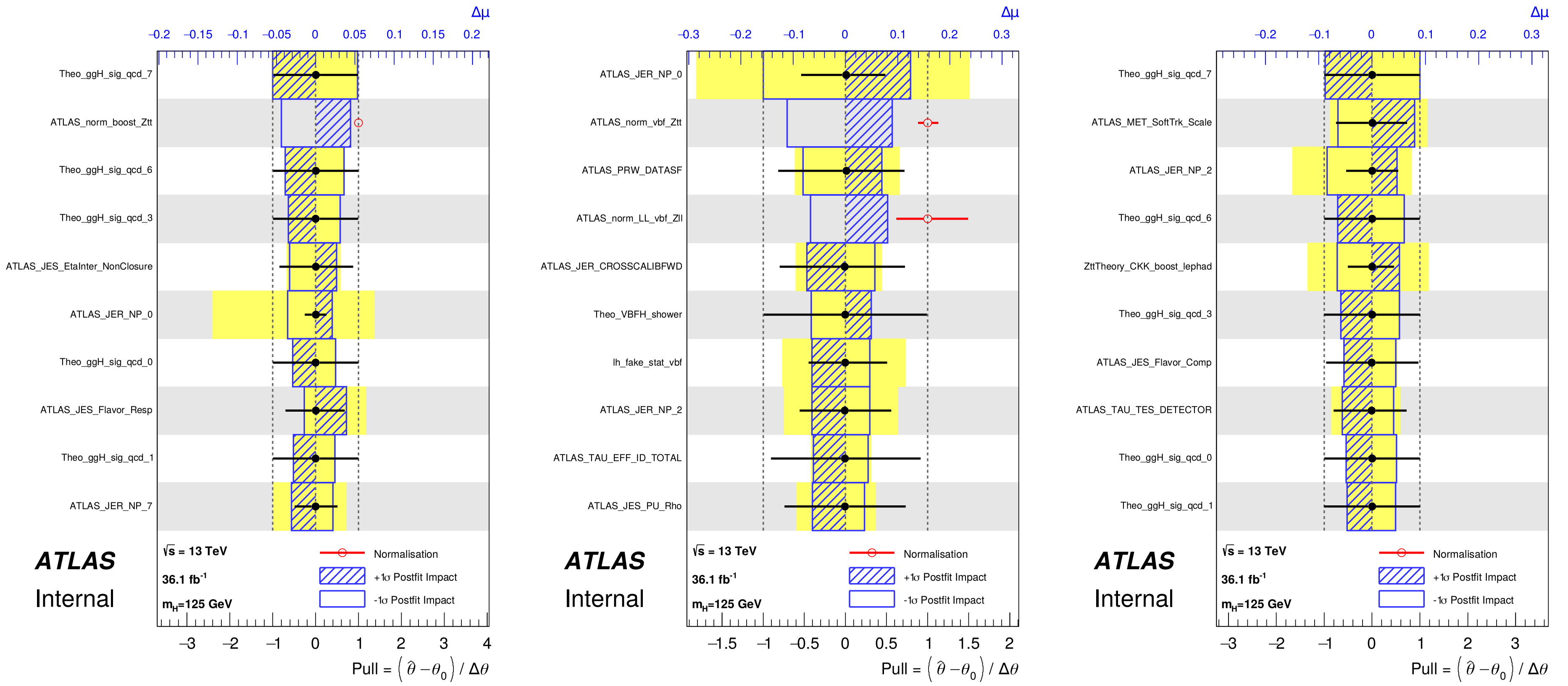

Figure 5.24: Impact of systematic uncertainties on $\mu_{H\to\tau\tau}$ as computed by the fit. Left plot shows the outcome of the combined fit of all channels and signal regions. Middle plot shows the outcome of the fit of all channels in the VBF signal regions. Right plot shows the outcome of the fit of all channels in the Boosted signal regions. The systematic uncertainties are listed in decreasing order of their impact on the parameter of interest (POI) on the y-axis. The hatched blue and open blue boxes show the variations of POI referring to the top x-axis ($\pm 1\sigma$ impact on the POI). The filled circles, referring to the bottom x-axis, show the pulls of the fitted NPs, i.e. the deviations of the fitted parameters $\hat{\theta}$ from their nominal values θ_0, normalised to their nominal uncertainties $\Delta\theta$. The black lines show the uncertainties of the NPs resulting from the fit. The open circles, also referring to the bottom x-axis, show the values of the fitted normalisation factors. Yellow bands show prefit impact of each NP.

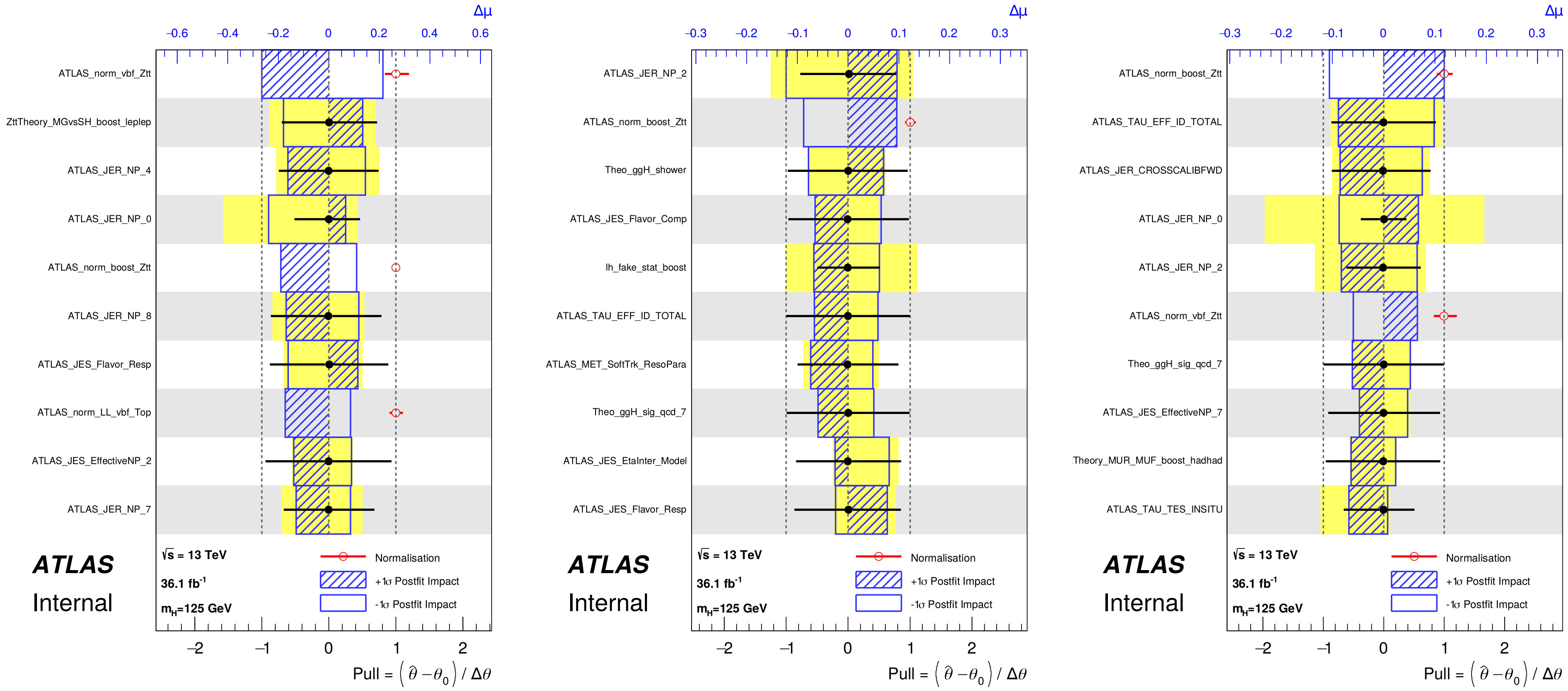

Figure 5.25: Impact of systematic uncertainties on $\mu_{H\to\tau\tau}$ as computed by the fit. Left plot shows the outcome of the fit of all signal regions in the $\tau_{\text{lep}}\tau_{\text{lep}}$ channel. Middle plot shows the outcome of the fit of all signal regions in the $\tau_{\text{lep}}\tau_{\text{had}}$ channel. Right plot shows the outcome of the fit of all signal regions in the $\tau_{\text{had}}\tau_{\text{had}}$ channel. The systematic uncertainties are listed in decreasing order of their impact on the parameter of interest (POI) on the y-axis. The hatched blue and open blue boxes show the variations of POI referring to the top x-axis ($\pm 1\sigma$ impact on the POI). The filled circles, referring to the bottom x-axis, show the pulls of the fitted NPs, i.e. the deviations of the fitted parameters $\hat{\theta}$ from their nominal values θ_0, normalised to their nominal uncertainties $\Delta\theta$. The black lines show the uncertainties of the NPs resulting from the fit. The open circles, also referring to the bottom x-axis, show the values of the fitted normalisation factors. Yellow bands show prefit impact of each NP.

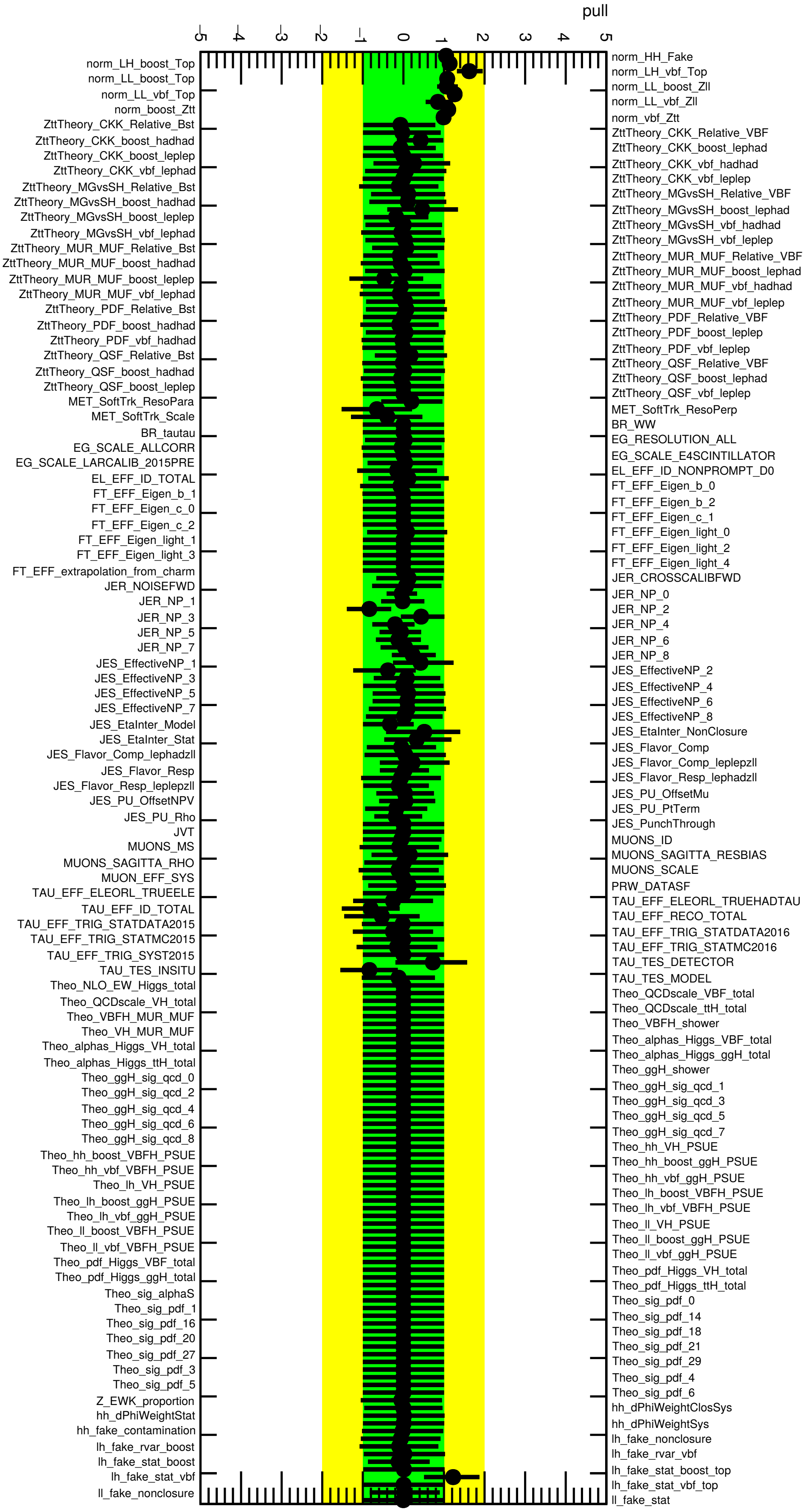

Figure 5.26: Constraints and pulls of all the nuisance parameters except for those related to MC statistics.

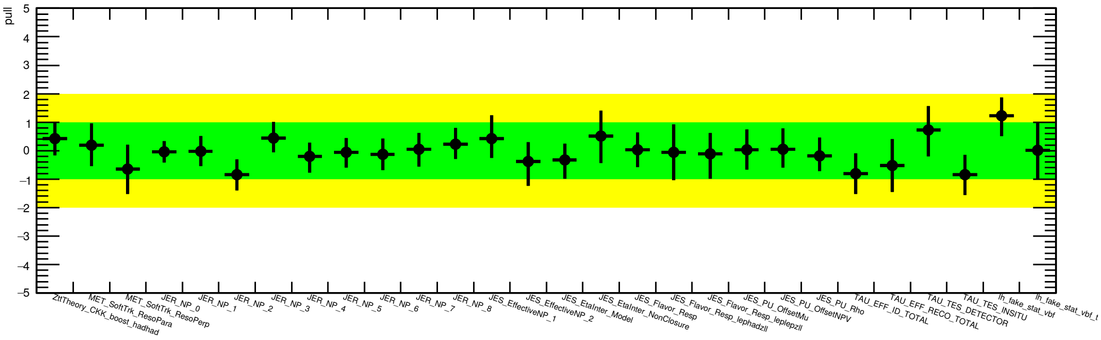

Figure 5.27: Constraints and pulls of the nuisance parameters for which the constraint is less than 0.75 of the prefit uncertainty or pulls greater than 0.5.

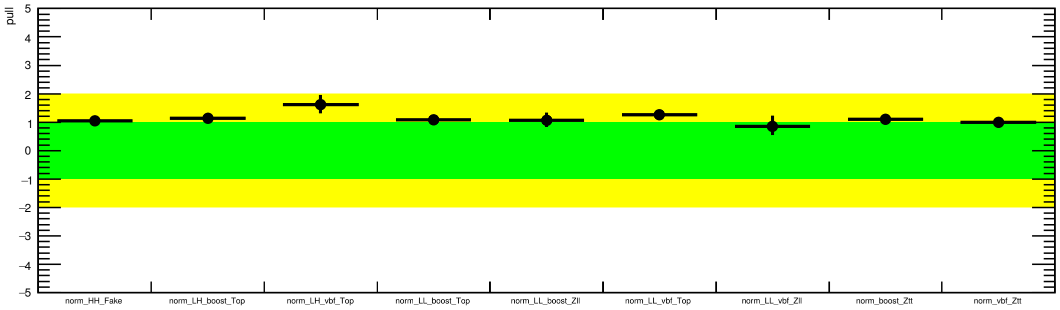

Figure 5.28: Postfit values of all normalisation factors entering the combined fit.

5.8.2 Fit results using low-mass $m_{\tau\tau}^{\text{MMC}}$ distribution

Furthermore, to study the behaviour of the fit model in real data before looking at the region where we expect Higgs boson signal, we provide a fit of the $m_{\tau\tau}^{\text{MMC}}$ distribution restricting its range below 100 GeV in all SRs. As the signal contribution is really small in this region (less than 3 expected events), in order to avoid unphysical large downward fluctuation of the signal strength we introduce in the fit a criterion of $\mu \geq 0$.

All results in this section use a $\tau_{\text{had}}\tau_{\text{had}}$ workspace inputs with a wrong implementation of the ggH parton shower uncertainty. The impact of this uncertainty is marginal and the conclusions drawn in this section does not change in any way after its correct implementation.

Nuisance parameter constraints

Figure 5.26 shows the constraints and pulls of the NPs and NFs from a combined fit, excluding the NPs for the MC statistics. NPs with pulls greater than 0.5 or constraints smaller than 0.75 are shown in Figure 5.27. Pulls observed in the low mass fit are in good agreement with those observed in the fit of whole $m_{\tau\tau}^{\text{MMC}}$ range.

Postfit normalisation

Figure 5.28 summarises the postfit values of the NFs considered in the fit.

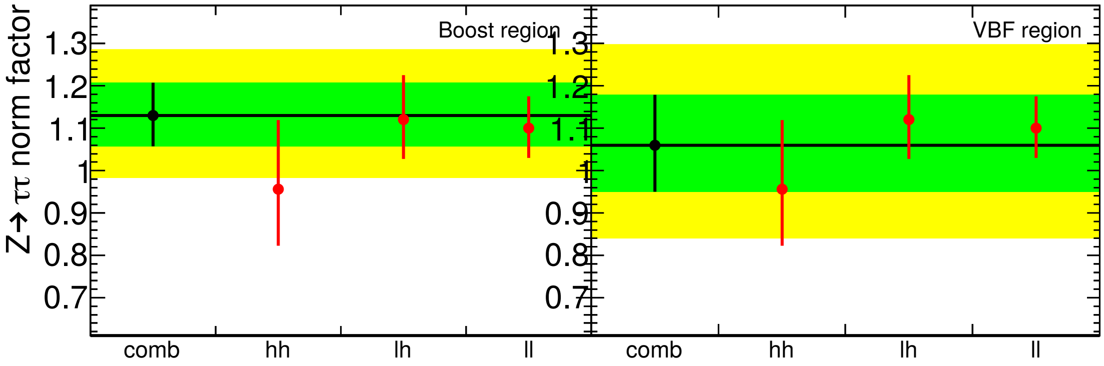

Figure 5.29: The summary of the $Z \to \tau\tau$ normalisation factors in the nominal scenario (black) and the split-by-channel scenario (red).

Table 5.13: Pulls of the nuisance parameters which can impact the normalisation of the $Z \to \tau\tau$ background in the nominal scenario as well as the split-by-channel scenario.

Nuisance parameter	Nominal	Split-by-channel
TAU_EFF_ELEORL_TRUEELE	$0.01^{+1.00}_{-1.00}$	$0.00^{+1.00}_{-1.00}$
TAU_EFF_ELEORL_TRUEHADTAU	$-0.39^{+0.98}_{-0.98}$	$-0.04^{+0.99}_{-0.99}$
TAU_EFF_ID_TOTAL	$-0.66^{+0.76}_{-0.71}$	$-0.05^{+0.98}_{-0.99}$
TAU_EFF_RECO_TOTAL	$-0.46^{+0.93}_{-0.93}$	$-0.18^{+0.98}_{-0.99}$
TAU_EFF_TRIG_STATDATA2015	$-0.02^{+1.01}_{-1.01}$	$-0.03^{+1.01}_{-1.01}$
TAU_EFF_TRIG_STATDATA2016	$-0.38^{+0.99}_{-0.99}$	$-0.09^{+0.99}_{-0.99}$
TAU_EFF_TRIG_STATMC2015	$0.00^{+1.00}_{-1.00}$	$0.00^{+1.00}_{-1.00}$
TAU_EFF_TRIG_STATMC2016	$-0.23^{+0.99}_{-0.99}$	$-0.06^{+0.99}_{-0.99}$
TAU_EFF_TRIG_SYST2015	$0.00^{+1.00}_{-1.00}$	$0.00^{+1.00}_{-1.00}$

Using the low mass fit, we test several schemes for the normalisation of the $Z \to \tau\tau$ background:

- *Nominal:* 2 NFs, 1 NF across all the channels for the boosted SR and 1 NF across all the channels for the VBF SR
- *Split-by-channel:* 6 NFs, 1 NF per channel for the boosted SR and 1 NF per channel in the VBF SR
- *Full-splitting:* 13 NFs, 1 NF for each of the 13 SRs considered in the fit

Figure 5.29 shows the postfit values of the NFs in the nominal scheme and the split-by-channel scheme. We observe a good agreement across the three channels as well as with the combination; however, the NF for the $\tau_{\text{had}}\tau_{\text{had}}$ channel is lower than the combination and the other channels. In the combined fit, we notice that the NPs related to the tau lepton identification (TAU_ID) are pulled down, while when we split the $Z \to \tau\tau$ NFs in the three channels, this is not the case as illustrated in Table 5.13. The difference in the NFs noticed in the fit on the individual channel is absorbed by TAU_EFF_ID_TOTAL and TAU_TES_DETECTOR NPs.

Figure 5.30 illustrates the behaviour of the $Z \to \tau\tau$ NFs in the three scenarios: nominal (black), split-by-channel (red), full-splitting (blue). In this test, the Top and $Z \to \ell\ell$ CRs are not included and we fix their normalisation to their expected

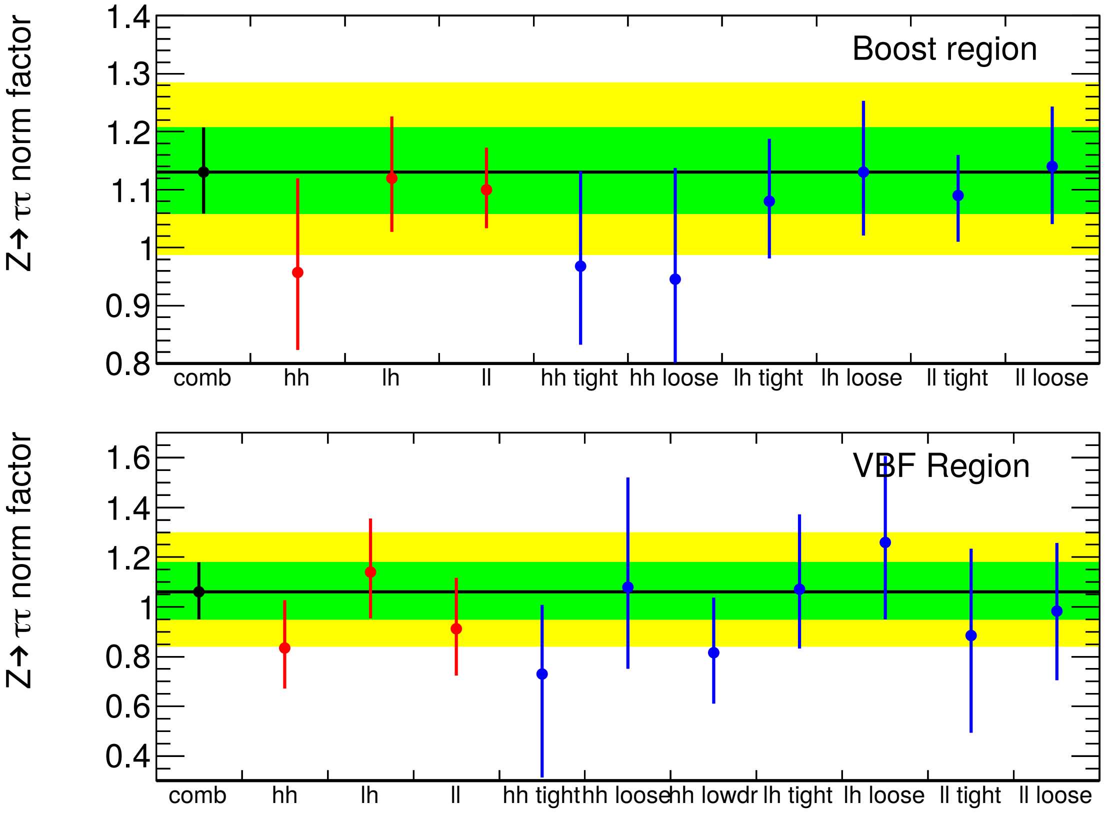

Figure 5.30: The summary of $Z \to \tau\tau$ normalisation factors in the three scenarios (nominal, split-by-channel, full-splitting), for the boosted category (top) and VBF category (bottom). We do not include Top or $Z \to \ell\ell$ control regions in the fit and their normalisations are fixed to the expected prefit values.

prefit values. As a consequence, the results in the nominal scenario as well as the split-by-channel scenario are slightly different from those shown in Figure 5.29.

5.8.3 Inclusion of the $Z \to \tau\tau$ CR in the fit

During the development of the analysis, we planned to use a $Z \to \tau\tau$ CR to constrain the normalisation and theoretical uncertainties on the dominant $Z \to \tau\tau$ background. Assuming lepton universality, we aimed to use the CRs enriched in $Z \to \ell\ell$ events for this purpose.

In general, the free-floating NFs and $Z \to \tau\tau$ theoretical uncertainties act on the $Z \to \tau\tau$ background in the corresponding SRs, as shown in Figure 5.4. When we include the $Z \to \tau\tau$ CRs in the fit, these NFs and NPs additionally act on the $Z \to \ell\ell$ events in the $Z \to \tau\tau$ CRs.

We run several fits with and without the $Z \to \tau\tau$ CRs. In case of including the $Z \to \tau\tau$ CRs in the fit we consider two possibilities:

- Use only the event yields of the $Z \to \tau\tau$ CRs (labelled as 'With $Z \to \tau\tau$ CR' in the table),
- Include also the shape information by fitting the dilepton-system p_{T} in the $Z \to \tau\tau$ CRs (labelled as 'With $Z \to \tau\tau$ CR shape' in the table)

Obtained expected sensitivity (Asimov fit) from the aforementioned scenarios and from the nominal fit without the $Z \to \tau\tau$ CRs is shown in Table 5.14. Including only the event yields of the $Z \to \tau\tau$ CRs result in a very small improvement of the sensitivity, while including the shape information provides larger improvement.

Figure 5.31 shows the pulls of the NPs from a combined fit with $Z \to \tau\tau$ CRs yield information, performed to measured data, but limited to $m_{\tau\tau}^{\text{MMC}}$ values below 100 GeV in the SRs. Figure 5.32 shows the pulls of the NPs from a combined fit with $Z \to \tau\tau$ CRs including shape information, performed to measured data, but limited to $m_{\tau\tau}^{\text{MMC}}$ values below 100 GeV in the SRs.

Table 5.15 shows the breakdown of the uncertainties on the signal strength for the standard fit (without $Z \to \tau\tau$ CRs) and for the case with single-bin $Z \to \tau\tau$ CRs using the Asimov dataset. Differences between the obtained results for the three scenarios are very small.

Furthermore, we investigate the possible splitting of the $Z \to \tau\tau$ CRs and using dedicated NFs for each of the exclusive SRs (loose/tight etc.). The definition of the VBF exclusive categories differs a lot between the three analysis channels, thus we investigate this option only in the boosted categories, where the difference in kinematic selections between the channels is small. During this investigations a single, separate CR and NF for $Z \to \tau\tau$ is used in the VBF category. Split CRs for the other background contributions ($Z \to \ell\ell$, top) were not available when performing the test, thus the comparison is made between the fits including:

- Only the SRs
- SRs and a single, inclusive $Z \to \tau\tau$ CR in boosted category (similar to that investigated above, except no other CRs are included)
- SRs and two $Z \to \tau\tau$ CRs for the boosted category, one CR for the loose categorisation and one for the tight categorisation (corresponding to low and high Higgs-candidate transverse momentum), with a single $Z \to \tau\tau$ NF across the boosted category
- SRs and two $Z \to \tau\tau$ CRs for the boosted category, one CR for the loose categorisation and one for the tight categorisation, with two $Z \to \tau\tau$ NFs, one for the loose and one for the tight selection (corresponding to the each of the two CRs)

Table 5.16 shows the results of this study. As can be seen, there is essentially no difference in the expected signal sensitivity between studied scenarios.

As the inclusion of the $Z \to \tau\tau$ CRs does not show a significant improvement of the expected signal significance compared to expected significance obtained from the fit without the $Z \to \tau\tau$ CRs, we have decided to not include $Z \to \tau\tau$ CRs in the final fit.

It should be noted that, no additional systematic uncertainties are considered in this investigation, for the extrapolation between $Z \to \ell\ell$ events in the $Z \to \tau\tau$ CRs and $Z \to \tau\tau$ events in the SRs. If it would be decided to use the $Z \to \tau\tau$ CRs as part of the default fit, we would have to further investigate these uncertainties. In other words, the expected significances and uncertainties provided in this section should be considered as optimistic upper limits (in the case such studies demonstrate that such an uncertainty is negligible/unnecessary). The fact that no notable improvement is observed even under this assumption, further strengthens the case for not using $Z \to \tau\tau$ CRs.

Table 5.14: A comparison of the expected sensitivity for the default setup without the $Z \to \tau\tau$ control region (CR), and two options of including the $Z \to \tau\tau$ CRs: either only the event yields are used ('With $Z \to \tau\tau$ CR'), or also shape information is included ('With $Z \to \tau\tau$ CR shape'), by fitting the dilepton-system p_{T} in the $Z \to \tau\tau$ CR rather than just the event yields. For consistency, the fits for this investigation were all performed using the same inputs, which is the reason why the result of the first row is not identical to the one presented in Section 5.7. The relative effects are however not expected to depend on this, since the differences in the inputs are not related to the $Z \to \tau\tau$ CRs.

Scenario	Expected significance [σ]			
	Combination	$\tau_{\mathrm{lep}}\tau_{\mathrm{lep}}$	$\tau_{\mathrm{lep}}\tau_{\mathrm{had}}$	$\tau_{\mathrm{had}}\tau_{\mathrm{had}}$
No $Z \to \tau\tau$ CR	4.26	0.98	2.43	3.05
With $Z \to \tau\tau$ CR	4.31	0.98	2.46	3.07
With $Z \to \tau\tau$ CR shape	4.34	1.01	2.48	3.09

Table 5.15: A comparison of the breakdown of the uncertainties on the signal strength for the standard fit without the $Z \to \tau\tau$ control region (CR) and the fit using a single-bin $Z \to \tau\tau$ CR. The uncertainties are grouped to individual categories according to their origin. 'All but normalisations' correspond to the fit in which all experimental and theoretical uncertainties are included, but the normalisation factors are excluded.

	Standard Fit	Fit with $Z \to \tau\tau$ CR
Parameter of interest	$\mu_{H\to\tau\tau}$	$\mu_{H\to\tau\tau}$
Central value	1.000	1.000
Set of nuisance parameters	Expected uncertainty	Expected uncertainty
Total	$+0.273/-0.250$	$+0.271/-0.249$
DataStat	$+0.157/-0.154$	$+0.157/-0.154$
FullSyst	$+0.223/-0.197$	$+0.221/-0.196$
All normalisations	$+0.062/-0.049$	$+0.062/-0.051$
Ztt normalisation	$+0.047/-0.033$	$+0.039/-0.029$
All but normalisations	$+0.214/-0.187$	$+0.218/-0.193$
Jets MET	$+0.131/-0.110$	$+0.128/-0.109$
BTag	$+0.024/-0.021$	$+0.030/-0.022$
Electron / Muon	$+0.023/-0.020$	$+0.029/-0.021$
Tau	$+0.075/-0.057$	$+0.070/-0.055$
Pileup reweighting	$+0.024/-0.014$	$+0.017/-0.010$
Fake estimation	$+0.052/-0.044$	$+0.048/-0.042$
Luminosity	$+0.041/-0.027$	$+0.043/-0.028$
Theory unc. (Signal)	$+0.070/-0.043$	$+0.070/-0.044$
Theory unc. (Ztautau)	$+0.057/-0.041$	$+0.064/-0.053$
MC stat	$+0.106/-0.102$	$+0.107/-0.103$

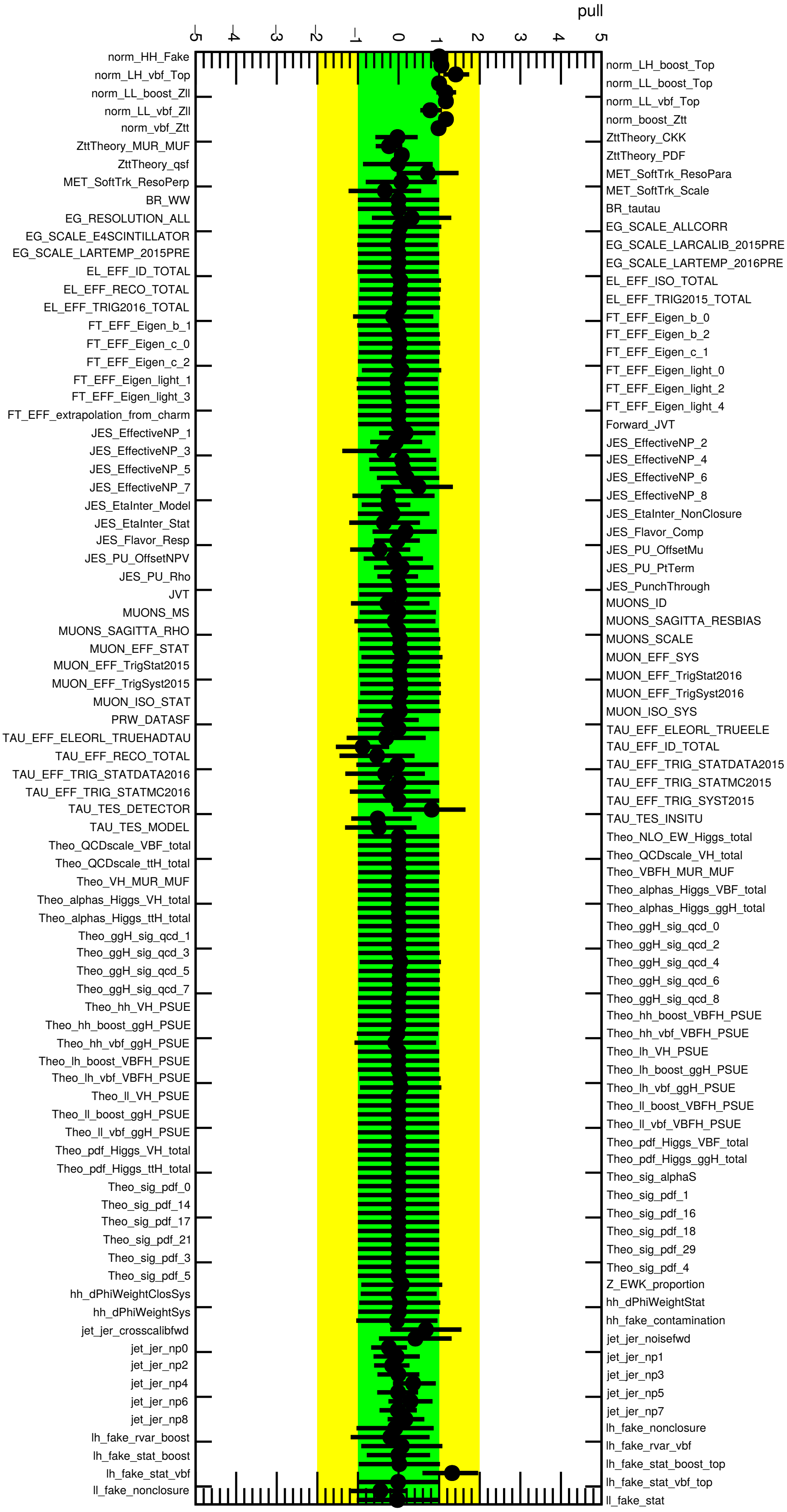

Figure 5.31: Pulls of nuisance parameters entering the combined fit with a 1-bin $Z \to \tau\tau$ CR.

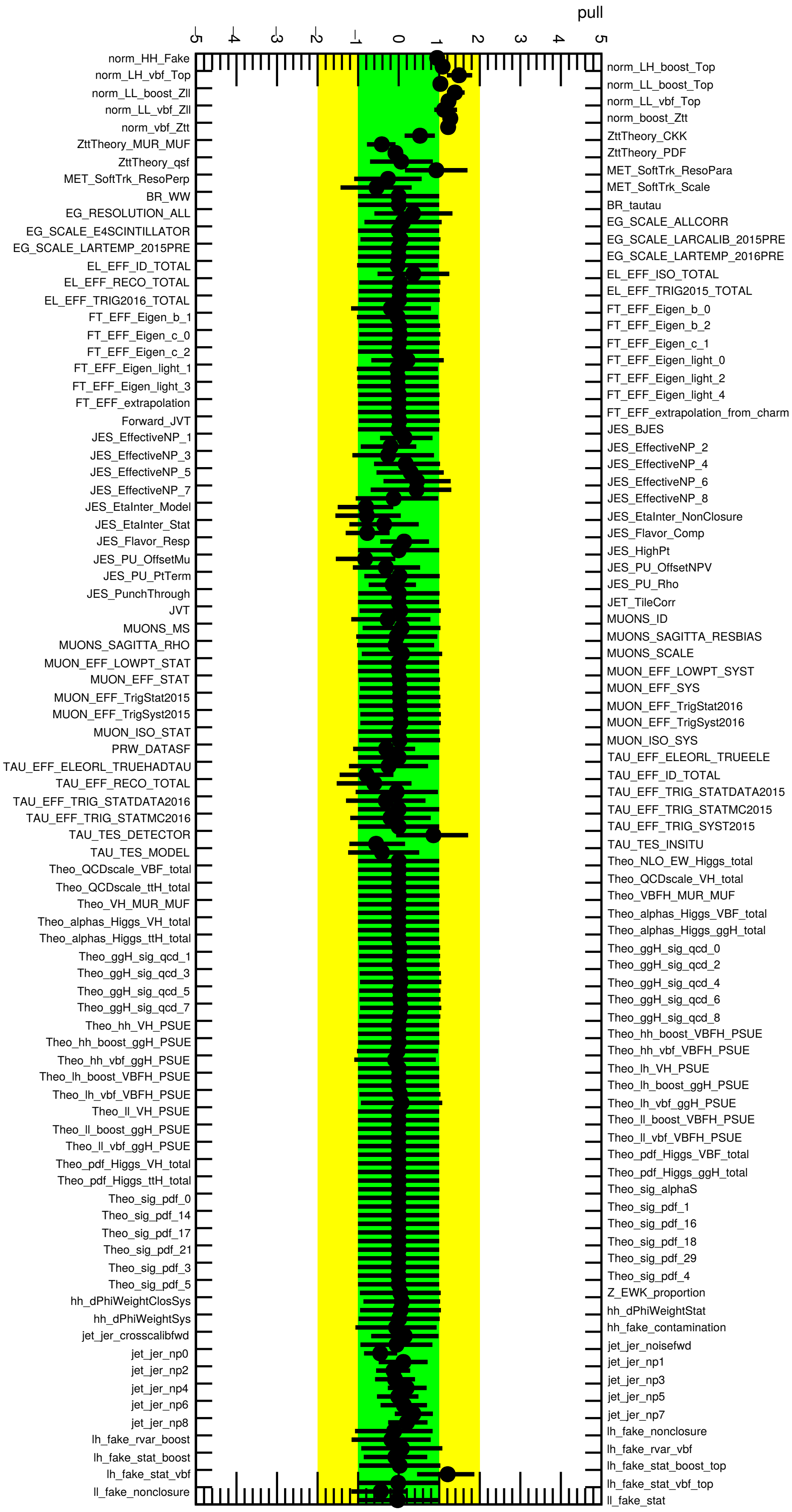

Figure 5.32: Pulls of nuisance parameters entering the combined fit with a $Z \to \tau\tau$ CR including shape information.

Table 5.16: A comparison of the expected sensitivity for different configurations, investigating the option of splitting the $Z \to \tau\tau$ boosted control regions (CRs) and corresponding normalisation factors (NFs). More details on the different configurations are provided in the text.

Configuration	Expected significance [σ]
SR only	4.40
SR and inclusive $Z \to \tau\tau$ CR	4.39
SR and split $Z \to \tau\tau$ boosted CRs; a single NF	4.41
SR and split $Z \to \tau\tau$ boosted CRs; separate NFs	4.38

5.8.4 Impact of a m_{jj} reweighting of Sherpa $Z(\to \tau\tau)$+jets MC on the sensitivity of the analysis

Further, we aim to quantify the impact of the m_{jj} mismodelling observed between the data and MC simulation, as the m_{jj} is an important variable for VBF categorisation. For this purpose we derive a reweighting function using the data/Sherpa $Z(\to \tau\tau)$+jets MC comparisons. The observed trend in the ratio of data to simulation as a function of m_{jj} is shown in Figure B.1.

In each channel, the reweighting acts on the relative normalisation of the VBF sub-categories within the VBF inclusive category and we want to make sure that the Sherpa $Z(\to \tau\tau)$+jets events match the data ones.

Table 5.17 summarises the yield ratio for data and Sherpa $Z(\to \tau\tau)$+jets MC between the VBF categories in the three analysis channels.

Table 5.18 shows the impact of the m_{jj} reweighting on the Sherpa $Z(\to \tau\tau)$+jets yields in the different VBF categories. As expected, the reweighting tends to reduce the size of the $Z(\to \tau\tau)$+jets background in the high m_{jj} categories. The magnitude of the effect ranges from a few % up to 10 % for the $\tau_{\text{lep}}\tau_{\text{lep}}$ VBF tight region. This behaviour is expected since the $\tau_{\text{lep}}\tau_{\text{lep}}$ VBF tight region is the one with the highest cut applied on m_{jj} variable.

In order to estimate the impact of this reweighting in the analysis, the expected significance is computed using the reweighted inputs and compared to the nominal setup, shown in Table 5.19. To conclude, reweighting the simulation with the observed m_{jj} distribution has a negligible impact on the measurement.

5.8.5 Inflating the fake uncertainties

Furthermore we want to evaluate the impact of the fake uncertainties and test the behaviour of the fit model in case we inflate the fake uncertainties by a factor of two. In practice, in the inputs each ‘fake’ variation is replaced using the following formula bin-by-bin:

$$\text{new variation} = 2 \times (\text{original variation} - \text{nominal}) + \text{nominal} \tag{5.2}$$

Table 5.20 shows the significance in each of the analysis channels for the fit with inflated fake uncertainties and the nominal fit. We can note that the impact

Table 5.17: Yield ratio of the different VBF categories for data and SHERPA $Z(\to \tau\tau)$+jets MC.

Channel	Ratio	Data	SHERPA $Z(\to \tau\tau)$+jets
$\tau_{\mathrm{lep}}\tau_{\mathrm{lep}}$	Loose / Tight	2.353	2.123 ± 0.046
$\tau_{\mathrm{lep}}\tau_{\mathrm{had}}$	Loose / Tight	1.730	1.760 ± 0.027
$\tau_{\mathrm{had}}\tau_{\mathrm{had}}$	Loose / Tight	0.674	0.590 ± 0.014
	Loose / High p_{T}	1.053	1.076 ± 0.018
	Tight / High p_{T}	1.562	1.824 ± 0.023

Table 5.18: Ratio of the inputs with m_{jj} reweighting applied on the SHERPA $Z(\to \tau\tau)$+jets event yields and the nominal in the VBF categories.

Channel	Category	m_{jj} / nom
$\tau_{\mathrm{lep}}\tau_{\mathrm{lep}}$	Loose	1.02
	Tight	0.90
$\tau_{\mathrm{lep}}\tau_{\mathrm{had}}$	Loose	1.03
	Tight	0.98
$\tau_{\mathrm{had}}\tau_{\mathrm{had}}$	Loose	1.06
	Tight	0.98
	High p_{T}	0.99

Table 5.19: Impact of the m_{jj} reweighting on the expected significance in each analysis channel.

Channel	Expected significance [σ]	
	m_{jj} reweighted inputs	Nominal
$\tau_{\mathrm{lep}}\tau_{\mathrm{lep}}$	1.230	1.183
$\tau_{\mathrm{lep}}\tau_{\mathrm{had}}$	2.812	2.813
$\tau_{\mathrm{had}}\tau_{\mathrm{had}}$	2.844	2.838

Table 5.20: A comparison of the expected significance between the nominal fit and an alternate version with inflated fake uncertainties. The significances are computed in a combined fit across all the channels.

Channel	Expected significance [σ]		
	Nominal	Inflated fake unc.	Difference
$\tau_{\mathrm{lep}}\tau_{\mathrm{lep}}$	1.18	1.17	0.01
$\tau_{\mathrm{lep}}\tau_{\mathrm{had}}$	2.68	2.58	0.10
$\tau_{\mathrm{had}}\tau_{\mathrm{had}}$	2.95	2.88	0.07

of the inflation of the uncertainties reduces the significance by 0.01, 0.10 and 0.07 in the $\tau_{\mathrm{lep}}\tau_{\mathrm{lep}}$, $\tau_{\mathrm{lep}}\tau_{\mathrm{had}}$ and $\tau_{\mathrm{had}}\tau_{\mathrm{had}}$ channel, respectively.

The expected constraints (from the Asimov fit) on the fake-related parameters in the two considered scenarios are listed in Table 5.21. In the $\tau_{\mathrm{lep}}\tau_{\mathrm{lep}}$ channel, the two fake NPs are constrained in the nominal fit. These constraints are increased

Table 5.21: A comparison of the expected constraints (Asimov dataset) on the fake related nuisance parameters between the nominal fit and an alternate scenario with inflated fake uncertainties.

Channel	Nuisance parameter	Expected constraints of nuisance parameters		
		Nominal	Inflated fake unc.	Difference
$\tau_{\mathrm{lep}}\tau_{\mathrm{lep}}$	ll_fake_nonclosure	$+0.83/-0.65$	$+0.69/-0.35$	$+0.14/-0.30$
	ll_fake_stat	$+0.75/-0.60$	$+0.50/-0.32$	$+0.25/-0.28$
$\tau_{\mathrm{lep}}\tau_{\mathrm{had}}$	lh_fake_nonclosure	$+0.95/-0.95$	$+0.86/-0.87$	$+0.09/-0.08$
	lh_fake_rvar_boost	$+0.96/-0.97$	$+0.88/-0.88$	$+0.08/-0.09$
	lh_fake_rvar_vbf	$+1.00/-1.00$	$+1.00/-1.00$	$+0.00/-0.00$
	lh_fake_stat_boost	$+0.47/-0.47$	$+0.28/-0.27$	$+0.19/-0.20$
	lh_fake_stat_boost_top	$+1.00/-1.00$	$+1.00/-1.00$	$+0.00/-0.00$
	lh_fake_stat_vbf	$+0.50/-0.45$	$+0.28/-0.23$	$+0.22/-0.27$
	lh_fake_stat_vbf _top	$+1.00/-1.00$	$+0.97/-0.97$	$+0.03/-0.03$
$\tau_{\mathrm{had}}\tau_{\mathrm{had}}$	norm_HH_Fake	$+0.15/-0.13$	$+0.24/-0.18$	$+0.09/-0.05$
	hh_dPhiWeightClosSys	$+0.94/-0.93$	$+0.83/-0.81$	$+0.11/-0.12$
	hh_dPhiWeightStat	$+1.00/-1.00$	$+1.00/-1.00$	$+0.00/-0.00$
	hh_dPhiWeightSys	$+1.00/-1.00$	$+1.00/-1.00$	$+0.00/-0.00$
	hh_fake_contamination	$+1.00/-1.00$	$+1.00/-1.00$	$+0.00/-0.00$

Table 5.22: A comparison of the expected impact (Asimov dataset) of the fake related nuisance parameters on the parameter of interest between the nominal fit and an alternate scenario with inflated fake uncertainties.

Channel	Nuisance parameter	Expected $\pm 1\sigma$ impact on μ	
		Nominal	Inflated fake unc.
$\tau_{\mathrm{lep}}\tau_{\mathrm{lep}}$	ll_fake_nonclosure	$+0.0012/-0.0059$	$+0.0218/-0.0152$
	ll_fake_stat	$+0.0014/-0.0005$	$+0.0066/-0.0022$
$\tau_{\mathrm{lep}}\tau_{\mathrm{had}}$	lh_fake_nonclosure	$+0.0104/-0.0083$	$+0.0494/-0.0438$
	lh_fake_rvar_boost	$+0.0029/-0.0020$	$+0.0002/-0.0082$
	lh_fake_rvar_vbf	$+0.0028/-0.0014$	$+0.0030/-0.0005$
	lh_fake_stat_boost	$+0.0149/-0.0077$	$+0.0042/-0.0026$
	lh_fake_stat_boost_top	$+0.0013/-0.0053$	$+0.0112/-0.0016$
	lh_fake_stat_vbf	$+0.0272/-0.0198$	$+0.0095/-0.0002$
	lh_fake_stat_vbf _top	$+0.0032/-0.0025$	$+0.0103/-0.0008$
$\tau_{\mathrm{had}}\tau_{\mathrm{had}}$	norm_HH_Fake	$+0.0148/-0.0117$	$+0.0099/-0.0035$
	hh_dPhiWeightClosSys	$+0.0146/-0.0073$	$+0.0236/-0.0159$
	hh_dPhiWeightStat	$+0.0007/-0.0054$	$+0.0037/-0.0069$
	hh_dPhiWeightSys	$+0.0000/-0.0000$	$+0.0002/-0.0004$
	hh_fake_contamination	$+0.0003/-0.0021$	$+0.0014/-0.0030$

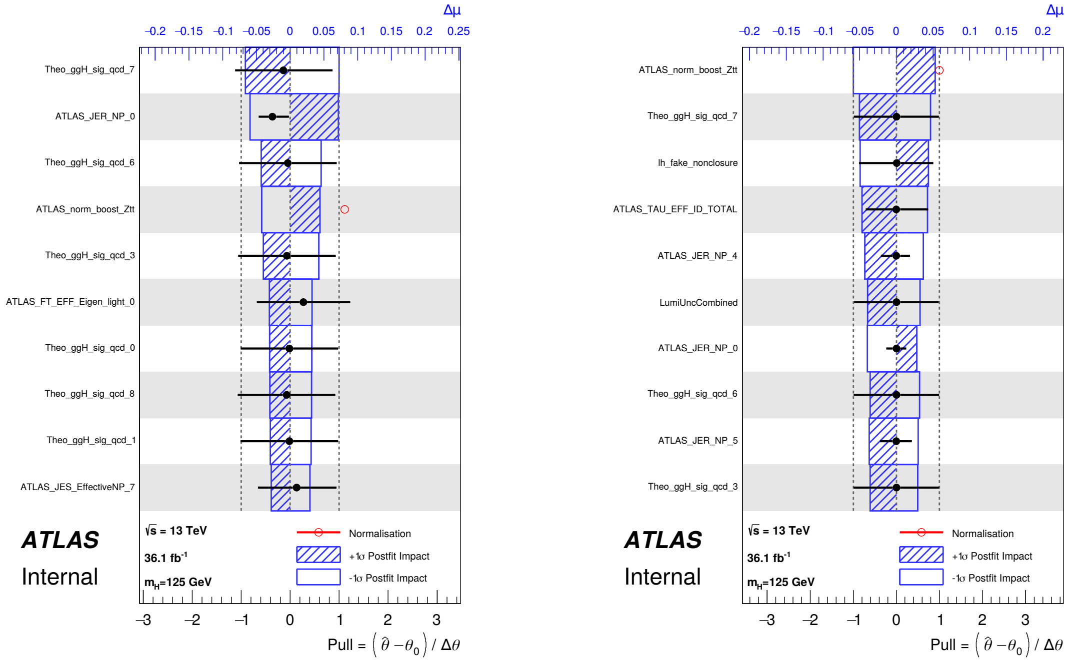

Figure 5.33: The impact of systematic uncertainties on $\mu_{H\to\tau\tau}$ as computed by the fit in the nominal scenario (left) and the alternative scenario with inflated fake uncertainties (right). The systematic uncertainties are listed in decreasing order of their impact on the parameter of interest (POI) on the y-axis. The hatched blue and open blue boxes show the variations of POI referring to the top x-axis ($\pm 1\sigma$ impact on the POI). The filled circles, referring to the bottom x-axis, show the pulls of the fitted NPs, i.e. the deviations of the fitted parameters $\hat{\theta}$ from their nominal values θ_0, normalised to their nominal uncertainties $\Delta\theta$. The black lines show the uncertainties of the NPs resulting from the fit. The open circles, also referring to the bottom x-axis, show the values of the fitted normalisation factors.

in the scenario with inflated fake uncertainties by up to 0.3σ which is quite consequent. However, as shown in Table 5.20, this change has a limited impact on the significance. In the $\tau_{\text{lep}}\tau_{\text{had}}$ channel, only the NPs related to the statistical power of the fake CRs are constrained in the nominal fit. In the scenario with inflated fake uncertainties, most NPs get constrained up to 0.27σ. This translates into a reducing the significance by 0.1σ. In the $\tau_{\text{had}}\tau_{\text{had}}$ channel, the normalisation of the fake background is left free-floating in the fit. In the nominal fit the uncertainty is about 15 % and it rises up to 24 % in the scenario with inflated fake uncertainties. hh_dPhiWeightClosSys is the only NP constrained in both scenarios and it increases by 0.1σ in the alternate scenario. This results in a degradation of the significance by 0.07σ.

The impact on the POI of the misidentified tau related parameters between the nominal fit and an alternate scenario with inflated fake uncertainties is shown in Table 5.22. The comparison of ten NPs with the highest impact on the POI for the two scenarios is shown in Figure 5.33. As we have changed input uncertainties related to the fake NPs, postfit values of all NPs, which minimise the negative-log likelihood are completely different in the two scenarios. As a result, the impact of the NPs on the POI and consequently their ranking differs significantly between the two scenarios.

Conclusion

In the thesis, I presented the results from the four years I spent working at the ATLAS experiment at the LHC.

The first part was dedicated to the time calibration of the Tile Calorimeter, the topic which was initially chosen as my qualification task, but I continued to contribute even after its completion. The importance of the accurate time calibration cannot be stressed enough, as it is necessary for the energy reconstruction, non-collision background removal as well as for specific physics analyses. Throughout the time I dedicated to this issue, I participated in the initial time calibration before the data taking with laser system and subsequent fine-tuning with collision data. Furthermore, I took part in monitoring the time stability with laser system and physics collision data. In particular, I performed the corrections for sudden changes in time settings, which were observed during the data taking and before the recorded data are processed for physics analyses.

The main part of the thesis deals with the physics analysis whose goal was the measurement of the production cross-sections of the Higgs boson in its decays to a pair of tau leptons. The used dataset come from pp collisions at a centre-of-mass energy of $\sqrt{s} = 13\,\text{TeV}$ and correspond to the integrated luminosity of $36.1\,\text{fb}^{-1}$. The analysis observed an excess of events over the expected background from other standard model processes with an observed (expected) significance of 4.4 (4.1) standard deviations. After combining with $24.8\,\text{fb}^{-1}$ of data collected at $\sqrt{s} = 7$ and $8\,\text{TeV}$, the observed (expected) significance amounted to 6.4 (5.4) standard deviations, which leads to a single-experiment observation of $H \to \tau\tau$ decays by ATLAS.

By using the data collected at $\sqrt{s} = 13\,\text{TeV}$, the $pp \to H \to \tau\tau$ total cross-section was found to be $\sigma_{H\to\tau\tau} = 3.77\,^{+0.60}_{-0.59}\,(\text{stat.})\,^{+0.87}_{-0.74}\,(\text{syst.})\,\text{pb}$, for a Higgs boson with a mass of $125\,\text{GeV}$. Moreover, I performed a two-dimensional fit to separate the vector-boson-mediated VBF process from the fermion-mediated ggF process. The cross-sections of the Higgs boson decaying into two tau leptons was measured to be

$$\begin{aligned} \sigma^{\text{VBF}}_{H\to\tau\tau} &= 0.38 \pm 0.09\,(\text{stat.})\,^{+0.11}_{-0.09}\,(\text{syst.})\,\text{pb}, \\ \sigma^{gg\text{F}}_{H\to\tau\tau} &= 3.1 \pm 1.0\,(\text{stat.})\,^{+1.6}_{-1.3}\,(\text{syst.})\,\text{pb}, \end{aligned}$$

for the two production processes. All these measurements are consistent with the Standard Model predictions.

Bibliography

[1] Lyndon Evans and Philip Bryant. LHC Machine. *JINST*, 3:S08001, 2008.

[2] ATLAS Collaboration. The ATLAS Experiment at the CERN Large Hadron Collider. *JINST*, 3:S08003, 2008.

[3] S. L. Glashow. Partial-symmetries of weak interactions. *Nucl. Phys.*, 22:579–588, 1961.

[4] Steven Weinberg. A Model of Leptons. *Phys. Rev. Lett.*, 19:1264–1266, 1967.

[5] Abdus Salam. Weak and Electromagnetic Interactions. *Proceedings of the 8th Nobel symposium, Ed. N. Svartholm, Almqvist & Wiskell, 1968,*, Conf. Proc. C680519:367–377, 1968.

[6] CMS Collaboration. The CMS experiment at the CERN LHC. *JINST*, 3:S08004, 2008.

[7] ATLAS Collaboration. Observation of a new particle in the search for the Standard Model Higgs boson with the ATLAS detector at the LHC. *Phys. Lett. B*, 716:1, 2012.

[8] CMS Collaboration. Observation of a new boson at a mass of 125 GeV with the CMS experiment at the LHC. *Phys. Lett. B*, 716:30, 2012.

[9] ATLAS Collaboration. Evidence for the Higgs-boson Yukawa coupling to tau leptons with the ATLAS detector. *JHEP*, 04:117, 2015.

[10] CMS Collaboration. Evidence for the direct decay of the 125 GeV Higgs boson to fermions. *Nature Phys.*, 10:557, 2014.

[11] ATLAS and CMS Collaborations. Measurements of the Higgs boson production and decay rates and constraints on its couplings from a combined ATLAS and CMS analysis of the LHC pp collision data at $\sqrt{s} = 7$ and 8 TeV. *JHEP*, 08:045, 2016.

[12] M. Aaboud et al. Observation of Higgs boson production in association with a top quark pair at the LHC with the ATLAS detector. *Phys. Lett.*, B784:173–191, 2018.

[13] CMS Collaboration. Observation of $\mathrm{t\bar{t}H}$ production. *Phys. Rev. Lett.*, 120(23):231801, 2018.

[14] ATLAS Collaboration. Observation of $H \to b\bar{b}$ decays and VH production with the ATLAS detector. *Phys. Lett. B*, 786:59–86, 2018.

[15] CMS Collaboration. Observation of Higgs Boson Decay to Bottom Quarks. *Phys. Rev. Lett.*, 121(12):121801, 2018.

[16] ATLAS Collaboration. Search for the Dimuon Decay of the Higgs Boson in pp Collisions at $\sqrt{s} = 13$ TeV with the ATLAS Detector. *Phys. Rev. Lett.*, 119:051802, 2017.

[17] CMS Collaboration. Search for the Higgs boson decaying to two muons in proton-proton collisions at $\sqrt{s} = 13$ TeV. *Submitted to: Phys. Rev. Lett.*, 2018.

[18] ATLAS Collaboration. Measurements of the Higgs boson production and decay rates and coupling strengths using pp collision data at $\sqrt{s} = 7$ and 8 TeV in the ATLAS experiment. *Eur. Phys. J. C*, 76:6, 2016.

[19] CMS Collaboration. Precise determination of the mass of the Higgs boson and tests of compatibility of its couplings with the standard model predictions using proton collisions at 7 and 8 TeV. *Eur. Phys. J. C*, 75:212, 2015.

[20] ATLAS Collaboration. Study of the spin and parity of the Higgs boson in diboson decays with the ATLAS detector. *Eur. Phys. J. C*, 75:476, 2015.

[21] CMS Collaboration. Constraints on the spin-parity and anomalous HVV couplings of the Higgs boson in proton collisions at 7 and 8 TeV. *Phys. Rev. D*, 92:012004, 2015.

[22] Morad Aaboud et al. Cross-section measurements of the Higgs boson decaying into a pair of τ-leptons in proton-proton collisions at $\sqrt{s} = 13$ TeV with the ATLAS detector. *Submitted to: Phys. Rev.*, 2018.

[23] ATLAS Collaboration. ATLAS tile calorimeter: Technical Design Report, 1996.

[24] F. Englert and R. Brout. Broken Symmetry and the Mass of Gauge Vector Mesons. *Phys. Rev. Lett.*, 13:321–323, 1964.

[25] Peter W. Higgs. Broken symmetries and the masses of gauge bosons. *Phys. Rev. Lett.*, 13:508–509, 1964.

[26] G.S. Guralnik, C.R. Hagen, and T.W.B. Kibble. Global Conservation Laws and Massless Particles. *Phys. Rev. Lett.*, 13:585–587, 1964.

[27] Peter W. Higgs. Spontaneous Symmetry Breakdown without Massless Bosons. *Phys. Rev.*, 145:1156–1163, 1966.

[28] T.W.B. Kibble. Symmetry Breaking in Non-Abelian Gauge Theories. *Phys. Rev.*, 155:1554–1561, 1967.

[29] Wikipedia. Standard Model — Wikipedia, the free encyclopedia. `http://en.wikipedia.org/w/index.php?title=Standard%20Model&oldid=888529742`, 2019. [Online; accessed 20-March-2019].

[30] Georges Aad et al. Combined Measurement of the Higgs Boson Mass in pp Collisions at $\sqrt{s} = 7$ and 8 TeV with the ATLAS and CMS Experiments. *Phys. Rev. Lett.*, 114:191803, 2015.

[31] LHC Higgs Cross Section Working Group, D. de Florian, C. Grojean, F. Maltoni, C. Mariotti, A. Nikitenko, M. Pieri, P. Savard, M. Schumacher, and R. Tanaka (Eds.). Handbook of LHC Higgs Cross Sections: 4. Deciphering the Nature of the Higgs Sector. *CERN-2017-002-M*, CERN, Geneva, 2016.

[32] Georges Aad et al. Measurements of the Higgs boson production and decay rates and constraints on its couplings from a combined ATLAS and CMS analysis of the LHC pp collision data at $\sqrt{s} = 7$ and 8 TeV. *JHEP*, 08:045, 2016.

[33] J. Beringer et al. Review of particle physics. *Phys. Rev. D*, 86:010001, 2012.

[34] Serguei Chatrchyan et al. Search for a standard-model-like Higgs boson with a mass in the range 145 to 1000 GeV at the LHC. *Eur. Phys. J.*, C73:2469, 2013.

[35] Albert M Sirunyan et al. Observation of the Higgs boson decay to a pair of τ leptons with the CMS detector. *Phys. Lett.*, B779:283–316, 2018.

[36] Morad Aaboud et al. Measurement of the Higgs boson mass in the $H \to ZZ^* \to 4\ell$ and $H \to \gamma\gamma$ channels with $\sqrt{s} = 13$ TeV pp collisions using the ATLAS detector. *Phys. Lett.*, B784:345–366, 2018.

[37] The ATLAS collaboration. Combined measurements of Higgs boson production and decay using up to 80 fb^{-1} of proton–proton collision data at $\sqrt{s} =$ 13 TeV collected with the ATLAS experiment. 2018.

[38] The ALICE Collaboration. The ALICE experiment at the CERN LHC. *Journal of Instrumentation*, 3(08):S08002–S08002, aug 2008.

[39] The LHCb Collaboration. The LHCb detector at the LHC. *Journal of Instrumentation*, 3(08):S08005–S08005, aug 2008.

[40] ATLAS Collaboration. Track Reconstruction Performance of the ATLAS Inner Detector at $\sqrt{s} = 13$ TeV. ATL-PHYS-PUB-2015-018, 2015.

[41] ATLAS Collaboration. The ATLAS Inner Detector commissioning and calibration. *Eur. Phys. J. C*, 70:787, 2010.

[42] M Capeans et al. ATLAS Insertable B-Layer Technical Design Report. Technical Report CERN-LHCC-2010-013. ATLAS-TDR-19, Sep 2010.

[43] ATLAS experiment. PublishedTilecalFigures. `https://twiki.cern.ch/twiki/bin/view/AtlasPublic/PublishedTilecalFigures`, 2019. [Online; accessed 20-March-2019].

[44] ATLAS liquid argon calorimeter: Technical design report. 1996.

[45] ATLAS Collaboration. Readiness of the ATLAS liquid argon calorimeter for LHC collisions. *Eur. Phys. J. C*, 70:723, 2010.

[46] A. Artamonov et al. The ATLAS forward calorimeters. *JINST*, 3:P02010, 2008.

[47] ATLAS Collaboration. Commissioning of the ATLAS Muon Spectrometer with cosmic rays. *Eur. Phys. J. C*, 70:875, 2010.

[48] Georges Aad et al. Performance of the ATLAS Trigger System in 2010. *Eur. Phys. J.*, C72:1849, 2012.

[49] Morad Aaboud et al. Performance of the ATLAS Trigger System in 2015. *Eur. Phys. J.*, C77(5):317, 2017.

[50] J. Abdallah et al. Mechanical construction and installation of the ATLAS Tile calorimeter. *JINST*, 8:T11001, 2013.

[51] J. Abdallah et al. The optical instrumentation of the ATLAS Tile Calorimeter. *JINST*, 8:P01005, 2013.

[52] S. Berglund et al. The ATLAS Tile Calorimeter digitizer. *JINST*, 3:P01004, 2008.

[53] ATLAS Collaboration. Readiness of the ATLAS Tile Calorimeter for LHC collisions. *Eur. Phys. J. C*, 70:1193, 2010.

[54] W.E. Cleland and E.G. Stern. Signal processing considerations for liquid ionization calorimeters in a high rate environment. *Nucl. Instrum. Meth. A*, 338:467 – 497, 1994.

[55] Morad Aaboud et al. Operation and performance of the ATLAS Tile Calorimeter in Run 1. *Eur. Phys. J.*, C78(12):987, 2018.

[56] Wigmans, R. *Calorimetry: Energy Measurement in Particle Physics.* International series of monographs on physics. Clarendon Press, 2000.

[57] P. Adragna et al. Testbeam studies of production modules of the ATLAS Tile Calorimeter. *Nucl. Instrum. Meth. A*, 606:362 – 394, 2009.

[58] ATLAS experiment. TileCaloPublicResultsTiming. `https://twiki.cern.ch/twiki/bin/view/AtlasPublic/TileCaloPublicResultsTiming`, 2019. [Online; accessed 20-March-2019].

[59] A. N. Kolmogorov. *Grundbegriffe der Wahrscheinlichkeitsrechnung.* Springer, 1933.

[60] A. N. Kolmogorov. *Foundations of the theory of probability.* Chelsea, 1956.

[61] Glen Cowan. *Statistical Data Analysis.* Clarendon (Oxford), Oxford, 1998 (ISBN: 0-19-850156-0 or 0-19-850155-2 in paperback).

[62] G. Cowan. Topics in statistical data analysis for high-energy physics. In *High-energy physics. Proceedings, 17th European School, ESHEP 2009, Bautzen, Germany, June 14-27, 2009*, pages 197–218, 2013. [,207(2013)].

[63] Glen Cowan, Kyle Cranmer, Eilam Gross, and Ofer Vitells. Asymptotic formulae for likelihood-based tests of new physics. *Eur. Phys. J. C*, 71:1554, 2011.

[64] Glen Cowan. Statistics for Searches at the LHC. In *Proceedings, 69th Scottish Universities Summer School in Physics : LHC Phenomenology (SUSSP69): St.Andrews, Scotland, August 19-September 1, 2012*, pages 321–355, 2013.

[65] Kyle Cranmer. Practical Statistics for the LHC. In *Proceedings, 2011 European School of High-Energy Physics (ESHEP 2011): Cheile Gradistei, Romania, September 7-20, 2011*, pages 267–308, 2015. [,247(2015)].

[66] Kyle Cranmer, George Lewis, Lorenzo Moneta, Akira Shibata, and Wouter Verkerke. HistFactory: A tool for creating statistical models for use with RooFit and RooStats. Technical Report CERN-OPEN-2012-016, New York U., New York, Jan 2012.

[67] F. James and M. Roos. Minuit: A System for Function Minimization and Analysis of the Parameter Errors and Correlations. *Comput. Phys. Commun.*, 10:343–367, 1975.

[68] Jerzy Neyman and E.S. Pearson. On the problem of the most efficient tests of statistical hypotheses. *Philosophical Transactions of the Royal Society, A*, 231:289–337, 01 1933.

[69] S. S. Wilks. The Large-Sample Distribution of the Likelihood Ratio for Testing Composite Hypotheses. *Annals Math. Statist.*, 9(1):60–62, 1938.

[70] Abraham Wald. Tests of statistical hypotheses concerning several parameters when the number of observations is large. *Transactions of the American Mathematical Society*, 54(3):426–426, March 1943.

[71] ATLAS and CMS Collaborations. Combined Measurement of the Higgs Boson Mass in pp Collisions at $\sqrt{s} = 7$ and 8 TeV with the ATLAS and CMS Experiments. *Phys. Rev. Lett.*, 114:191803, 2015.

[72] ATLAS Collaboration. The ATLAS Simulation Infrastructure. *Eur. Phys. J. C*, 70:823, 2010.

[73] GEANT4 Collaboration, S. Agostinelli et al. Geant4 – a simulation toolkit. *Nucl. Instrum. Meth. A*, 506:250, 2003.

[74] ATLAS Collaboration. Muon reconstruction performance of the ATLAS detector in proton–proton collision data at $\sqrt{s} = 13$ TeV. *Eur. Phys. J. C*, 76:292, 2016.

[75] ATLAS Collaboration. Performance of the ATLAS Trigger System in 2015. *Eur. Phys. J. C*, 77:317, 2017.

[76] ATLAS Collaboration. Electron and photon energy calibration with the ATLAS detector using LHC Run 1 data. *Eur. Phys. J. C*, 74:3071, 2014.

[77] ATLAS Collaboration. Electron efficiency measurements with the ATLAS detector using the 2015 LHC proton–proton collision data. ATLAS-CONF-2016-024, 2016.

[78] M. Cacciari, G. P. Salam and G. Soyez. The anti-k_t jet clustering algorithm. *JHEP*, 04:063, 2008.

[79] ATLAS Collaboration. Topological cell clustering in the ATLAS calorimeters and its performance in LHC Run 1. *Eur. Phys. J. C*, 77:490, 2017.

[80] ATLAS Collaboration. Performance of pile-up mitigation techniques for jets in pp collisions at $\sqrt{s} = 8$ TeV using the ATLAS detector. *Eur. Phys. J. C*, 76:581, 2016.

[81] ATLAS Collaboration. Identification and rejection of pile-up jets at high pseudorapidity with the ATLAS detector. 2017.

[82] ATLAS Collaboration. Measurement of the tau lepton reconstruction and identification performance in the ATLAS experiment using pp collisions at $\sqrt{s} = 13$ TeV. ATLAS-CONF-2017-029, 2017.

[83] ATLAS Collaboration. The ATLAS Tau Trigger in Run 2. ATLAS-CONF-2017-061, 2017.

[84] ATLAS Collaboration. Performance of missing transverse momentum reconstruction with the ATLAS detector using proton-proton collisions at $\sqrt{s}$ = 13 TeV. 2018.

[85] A. Elagin, P. Murat, A. Pranko, and A. Safonov. A New Mass Reconstruction Technique for Resonances Decaying to $\tau\tau$. *Nucl. Instrum. Meth. A*, 654:481–489, 2011.

[86] R. Ellis et al. Higgs decay to $\tau^+\tau^-$:a possible signature of intermediate mass higgs bosons at high energy hadron colliders. *Nucl. Phys. B*, 297:221, 1998.

[87] ATLAS Collaboration. Observation and measurement of Higgs boson decays to WW^* with the ATLAS detector. *Phys. Rev. D*, 92:012006, 2015.

[88] ATLAS Collaboration. Modelling $Z \to \tau\tau$ processes in ATLAS with τ-embedded $Z \to \mu\mu$ data. *JINST*, 10:P09018, 2015.

[89] Iain W. Stewart and Frank J. Tackmann. Theory uncertainties for Higgs mass and other searches using jet bins. *Phys. Rev. D*, 85:034011, 2012.

[90] Shireen Gangal and Frank J. Tackmann. Next-to-leading-order uncertainties in Higgs+2 jets from gluon fusion. *Phys. Rev. D*, 87(9):093008, 2013.

[91] Jon Butterworth et al. PDF4LHC recommendations for LHC Run II. *J. Phys. G*, 43:023001, 2016.

[92] LHC Higgs Cross Section Working Group, S. Dittmaier, C. Mariotti, G. Passarino, and R. Tanaka (Eds.). Handbook of LHC Higgs Cross Sections: 1. Inclusive Observables. *CERN-2011-002*, CERN, Geneva, 2011.

[93] Leif Lonnblad and Stefan Prestel. Matching Tree-Level Matrix Elements with Interleaved Showers. *JHEP*, 03:019, 2012.

[94] J. Alwall, R. Frederix, S. Frixione, V. Hirschi, F. Maltoni, et al. The automated computation of tree-level and next-to-leading order differential cross sections, and their matching to parton shower simulations. *JHEP*, 07:079, 2014.

[95] ATLAS Collaboration. Electron identification measurements in ATLAS using $\sqrt{s} = 13$ TeV data with 50 ns bunch spacing. ATL-PHYS-PUB-2015-041, 2015.

[96] ATLAS Collaboration. Luminosity determination in *pp* collisions at $\sqrt{s} =$ 7 TeV using the ATLAS detector at the LHC. *Eur. Phys. J. C*, 71:1630, 2011.

[97] ATLAS Collaboration. Luminosity determination in *pp* collisions at $\sqrt{s} =$ 8 TeV using the ATLAS detector at the LHC. *Eur. Phys. J. C*, 76:653, 2016.

[98] ATLAS Collaboration. Jet energy scale measurements and their systematic uncertainties in proton–proton collisions at $\sqrt{s} = 13$ TeV with the ATLAS detector. 2017.

[99] ATLAS Collaboration. Jet Calibration and Systematic Uncertainties for Jets Reconstructed in the ATLAS Detector at $\sqrt{s} = 13$ TeV. ATL-PHYS-PUB-2015-015, 2015.

[100] ATLAS Collaboration. Identification and energy calibration of hadronically decaying tau leptons with the ATLAS experiment in *pp* collisions at $\sqrt{s} =$ 8 TeV. *Eur. Phys. J. C*, 75:303, 2015.

[101] Morad Aaboud et al. Electron and photon energy calibration with the ATLAS detector using 2015-2016 LHC proton-proton collision data. *Submitted to: JINST*, 2018.

[102] ATLAS Collaboration. Reconstruction, Energy Calibration, and Identification of Hadronically Decaying Tau Leptons in the ATLAS Experiment for Run-2 of the LHC. ATL-PHYS-PUB-2015-045, 2015.

[103] ATLAS Collaboration. Tagging and suppression of pileup jets with the ATLAS detector. ATLAS-CONF-2014-018, 2014.

[104] ATLAS Collaboration. Performance of b-jet identification in the ATLAS experiment. *JINST*, 11:P04008, 2016.

[105] Roostats. https://twiki.cern.ch/twiki/bin/view/RooStats/WebHome.

[106] J. Friedman. Data analysis techniques for high energy particle physics. In *Proceedings of 3rd CERN School on Computing*, 1974.

[107] Hbb WG. Wsmaker software package. svn+ssh://svn.cern.ch/reps/atlasphys-hsg5/Physics/Higgs/HSG5/Limits/InputPreparation/WSMaker/trunk.

List of abbreviations

gg**F** gluon–gluon fusion. 6

BEH mechanism Brout-Englert-Higgs mechanism. 3

CERN European Organisation for Nuclear Research. 3

CL confidence level. 79

CP charge-parity. 3

CRs control regions. 45

CSCs Cathode Strip Chambers. 18

EBs extended barrels. 21

EW electroweak. 45

FCal Forward Calorimeter. 17

HEC Hadronic End-cap Calorimeter. 17

HLT high-level trigger. 19

IBL Insertable B-Layer. 14

ID inner detector. 14

IPs interaction points. 13

JER jet energy resolution. 39

JES jet energy scale. 57

JVT Jet Vertex Tagger. 47

L1 first-level trigger. 19

LB central (long) barrel. 21

LBs luminosity blocks. 25

LHC Large Hadron Collider. 3

LO leading order. 56

LS1 Long Shutdown 1. 9

MBTS Minimum Bias Trigger Scintillators. 19

MC Monte Carlo. 36

MDTs Monitored Drift Tube chambers. 18
MLE maximum likelihood estimator. 33
MMC missing-mass calculator. 48

NF normalisation factor. 54
NLL negative-log likelihood. 34
NLO next-to-leading order. 56
NNLO next-to-next-to-leading order. 46
NPs nuisance parameters. 31

OF Optimal Filtering. 23
ORL overlap removal. 46

PDF parton distribution function. 7
pdf probability density function. 31
PMTs photomultiplier tubes. 21
POIs parameters of interest. 31

QCD quantum chromodynamics. 7

ROS read-out system. 19
RPCs Resistive Plate Chambers. 18

SCT semiconductor tracker. 14
SF same-flavour. 48
SM Standard Model. 3
SRs signal regions. 45

TDAQ Trigger and Data Acquisition. 18
TES $\tau_{\text{had-vis}}$ energy scale. 39
TGCs Thin Gap Chambers. 18
TileCal Tile Calorimeter. 3
TRT transition radiation tracker. 14

UEPS underlying event, hadronisation and parton shower. 46

VBF vector boson fusion. 6
VRs validation regions. 52

WLS wavelength shifting. 21

List of Publications

As a member of the ATLAS collaboration, I am an author of about 300 publications. I have contributed to the four physics measurements and ATLAS detector operation, which result in the following publications:

Papers:

1. ATLAS Collaboration. Cross-section measurements of the Higgs boson decaying into a pair of tau-leptons in proton-proton collisions at $\sqrt{s} = 13$ TeV with the ATLAS detector. Submitted to: Phys. Rev. D 99, 072001 (2019). `https://arxiv.org/abs/1811.08856`
2. ATLAS Collaboration. Searches for lepton-flavour-violating decays of the Higgs boson in $\sqrt{s} = 13$ TeV pp collisions with the ATLAS detector. (not published yet, ongoing ATLAS approval process)

Conference Notes:

1. ATLAS Collaboration. Measurement of the $H \to \tau^+\tau^-$ cross-section in 13 TeV Collisions with the ATLAS Detector.
2. ATLAS Collaboration. Searches for lepton-flavour-violating decays of the Higgs boson in $\sqrt{s} = 13$ TeV pp collisions with the ATLAS detector.
3. ATLAS Collaboration. ATLAS Combined Higgs Boson Measurements with 2015-2017 data at $\sqrt{s} = 13$ TeV.

Publication Notes:

1. ATLAS Collaboration. Projections for measurements of Higgs boson cross sections, branching ratios, coupling parameters and mass with the ATLAS detector at the HL-LHC. `https://atlas.web.cern.ch/Atlas/GROUPS/PHYSICS/PUBNOTES/ATL-PHYS-PUB-2018-054/`

Conference proceedings:

1. M. Mlynáriková. Study of the $H \to \tau + \tau$ decay channel with ATLAS. *Proceedings of the ICHEP2018 conference*, 2018. `https://pos.sissa.it/340/742/`
2. M. Mlynáriková. Study of the $H \to \tau\tau$ decay channel with ATLAS. *Proceedings of the ALPS2018 conference*, 2018. `https://pos.sissa.it/330/051/`
3. M. Mlynáriková. Performance of the ATLAS Hadronic Tile Calorimeter. *Proceedings of the Fifth Annual Conference on Large Hadron Collider Physics*, 2017. `https://arxiv.org/pdf/1709.00100`
4. M. Mlynáriková. Upgrade of the ATLAS Hadronic Tile Calorimeter for the High Luminosity LHC. *Proceedings of the Fifth Annual Conference on Large Hadron Collider Physics*, 2017. `https://arxiv.org/pdf/1709.00099`

Appendices

A. Di-tau invariant mass reconstruction

The key discriminant variable which distinguishes the Higgs boson signal from background processes is the mass of the di-tau system. The difference between the Z boson and Higgs boson mass provides the best separation between the signal processes and the $Z \to \tau\tau$ and $Z \to \ell\ell$ processes. The background contribution originating from misidentified taus are expected to be flat across the mass spectrum and it is a non-resonant background. Thus we can extract the signal with maximum sensitivity by fitting the di-tau mass spectrum.

One of the challenges when analysing the Higgs boson decays to a pair of tau leptons is the proper reconstruction of its mass due to the presence of at least two neutrinos in the final state. The neutrinos do not leave any signal in the detector, thus it is not possible to measure the contributions of the neutrinos to the four-momenta of the tau leptons. The presence of neutrinos in the final state and thus $E_{\mathrm{T}}^{\mathrm{miss}}$ hinders the complete reconstruction of the Higgs boson mass. However, we can obtain a rather good approximation of the $m_{\tau\tau}$ mass for the $H \to \tau\tau$ decays due to the strong boost of the two tau leptons. In this section, we present two approaches which can be used for the $H \to \tau\tau$ mass reconstruction, the collinear mass approximation [86] and the Missing Mass Calculator (MMC) [85].

A.1 Collinear mass approximation

The collinear mass approximation technique assumes that the neutrino momenta are collinear with the visible decay products of the tau lepton. The mass $m_{\tau\tau}^{\mathrm{coll}}$ calculated by this approximation is not used as a final discriminant in the $H \to \tau\tau$ analysis; however, is used in the event selection for the $\tau_{\mathrm{lep}}\tau_{\mathrm{lep}}$ channel.

A.2 Missing mass calculator

Instead of making one underlying assumption to estimate the kinematics of neutrinos, the MMC builds likelihood functions in order to estimate the most likely value of the missing components.

We construct the likelihood functions from the angular distribution between visible tau decay products and the tau vector. Then, to maximise the likelihood function, the likelihood scan is performed over the angles between the visible and invisible components of the tau decay.

The Higgs boson mass calculated by the MMC, $m_{\tau\tau}^{\mathrm{MMC}}$, with the RMS of approximately 20 GeV, is used as the final discriminating variable in the $H \to \tau\tau$ measurement. We prefer the MMC method over the collinear mass approximation as it exhibits less degradation in mass resolution in cases where the Higgs boson system is less boosted. The $m_{\tau\tau}^{\mathrm{MMC}}$ provides the best discrimination against the $Z \to \tau\tau$ background contributions as well. Figure A.1 shows $m_{\tau\tau}^{\mathrm{MMC}}$ reconstructed for $Z \to \tau\tau$ and $H \to \tau\tau$ events and the separation between these two processes is evident.

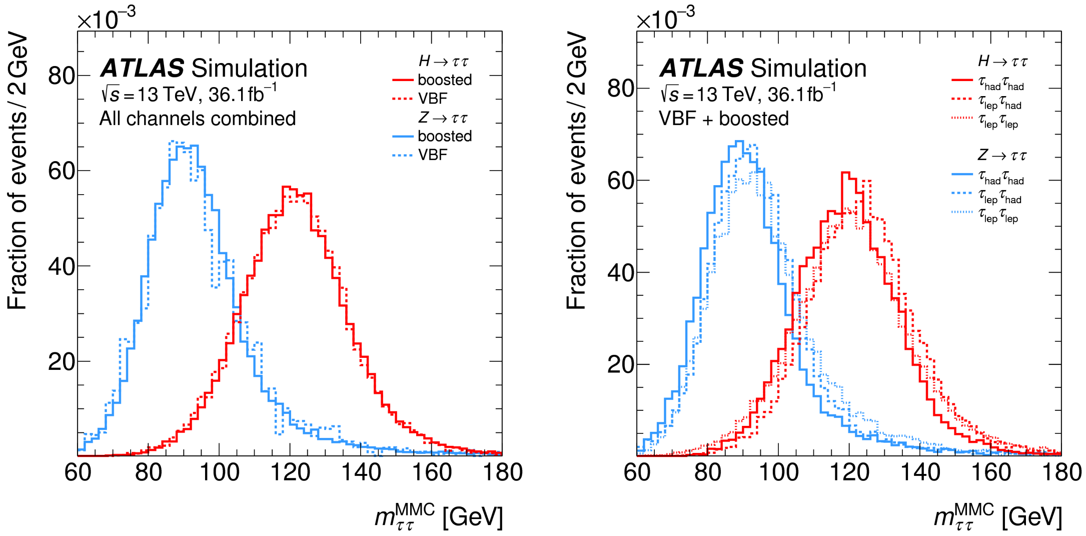

Figure A.1: Distribution of the Higgs boson mass, reconstructed with the Missing Mass Calculator algorithm split by category (left) and channel (right).

B. $Z \to \tau\tau$ validation region

We use Sherpa MC simulations to model the $Z \to \tau\tau$ background. We validate the modelling of this important background by using $Z \to \tau\tau$ VRs which consist of $Z \to \ell\ell$ events. We compare the observed distributions of several variables (e.g. $p_{\mathrm{T}}^{\ell\ell}$, m_{jj}, $p_{\mathrm{T}}^{\ell_1}$) with simulation normalised to the event yields observed in data. In general, Sherpa simulation describes the shape of data distributions within the theoretical and experimental uncertainties. However, we observe a slight trend in the ratio of data to simulation as a function of $\Delta\eta_{jj}$ and m_{jj}, shown in Figure B.1. This trend was further studied and shown no impact on the modelling of $m_{\tau\tau}^{\mathrm{MMC}}$, and reweighting of the simulation with the observed m_{jj} distribution in the VBF category has shown a negligible impact on the measurement, more details in Section 5.8.4.

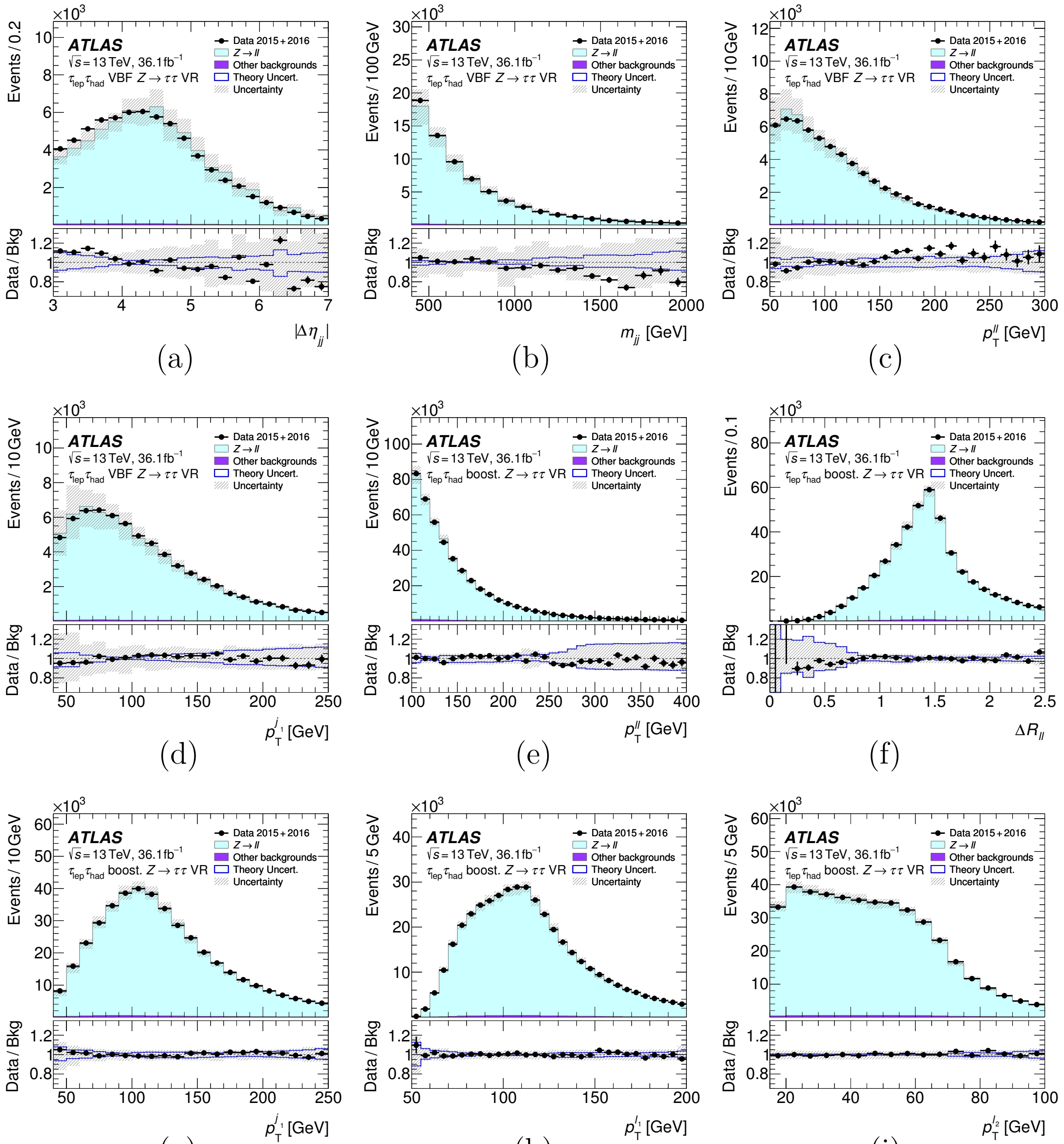

(a) (b) (c)

(d) (e) (f)

(g) (h) (i)

Figure B.1: The observed and expected distributions in the $Z \to \tau\tau$ validation regions corresponding to (a)–(d) the $\tau_{\mathrm{lep}}\tau_{\mathrm{had}}$ VBF inclusive category and (e)–(i) the $\tau_{\mathrm{lep}}\tau_{\mathrm{had}}$ boosted inclusive category. Shown are, in the respective region: (a) the pseudorapidity separation ($|\Delta\eta_{jj}|$) and (b) the invariant mass (m_{jj}) of the two highest-p_{T} jets; (c) and (e) the p_{T} of the di-lepton system ($pt^{\ell\ell}$); (d) and (g) the p_{T} of the highest-p_{T} jet ($p_{\mathrm{T}}^{j_1}$); (f) the angular distance between the light leptons ($\Delta R_{\ell\ell}$); (h) the p_{T} of the highest-p_{T} light lepton ($p_{\mathrm{T}}^{\ell_1}$); and (i) the p_{T} of the second-highest-p_{T} light lepton ($p_{\mathrm{T}}^{\ell_2}$). The predictions in these validation regions are not computed by the fit, but are simply normalised to the event yield in data. The size of the combined statistical, experimental and theoretical uncertainties is indicated by the hatched bands. The ratios of the data to the background model are shown in the lower panels together with the theoretical uncertainties in the Sherpa simulation of $Z \to \ell\ell$, which are indicated by the blue lines.

C. Postfit values of the NPs

Nuisance parameter	Postfit value (in σ unit)
μ	$1.09^{+0.316}_{-0.279}$
ATLAS_norm_HH_Fake	$1.12^{+0.129}_{-0.114}$
ATLAS_norm_LH_boost_Top	$1.13^{+0.0745}_{-0.0702}$
ATLAS_norm_LH_vbf_Top	$1.53^{+0.304}_{-0.273}$
ATLAS_norm_LL_boost_Top	$1.07^{+0.045}_{-0.0455}$
ATLAS_norm_LL_boost_Zll	$1.27^{+0.3}_{-0.251}$
ATLAS_norm_LL_vbf_Top	$1.19^{+0.0895}_{-0.087}$
ATLAS_norm_LL_vbf_Zll	$0.877^{+0.344}_{-0.303}$
ATLAS_norm_boost_Ztt	$1.11^{+0.0476}_{-0.0452}$
ATLAS_norm_vbf_Ztt	$1.04^{+0.0958}_{-0.0886}$
ATLAS_BR_WW	-0.00102^{+1}_{-1}
ATLAS_BR_tautau	$-1.45e-06^{+1}_{-1}$
ATLAS_EG_RESOLUTION_ALL	$0.0413^{+0.961}_{-0.965}$
ATLAS_EG_SCALE_ALLCORR	$-0.0236^{+1}_{-0.993}$
ATLAS_EG_SCALE_E4SCINTILLATOR	$-6.41e-07^{+1}_{-1}$
ATLAS_EG_SCALE_LARCALIB_2015PRE	$0.185^{+0.96}_{-1.16}$
ATLAS_EL_EFF_ID_NONPROMPT_D0	$0.142^{+0.978}_{-0.98}$
ATLAS_EL_EFF_ID_TOTAL	$0.00176^{+0.98}_{-0.979}$
ATLAS_EL_EFF_ISO_TOTAL	$1.5e-05^{+1}_{-1}$
ATLAS_EL_EFF_RECO_TOTAL	$4.62e-05^{+1}_{-1}$
ATLAS_EL_EFF_TRIG2015_TOTAL	$6.97e-05^{+1}_{-1}$
ATLAS_EL_EFF_TRIG2016_TOTAL	$6.97e-05^{+1}_{-1}$
ATLAS_FT_EFF_Eigen_b_0	$-0.56^{+0.839}_{-0.857}$
ATLAS_FT_EFF_Eigen_b_1	$-0.134^{+0.993}_{-0.992}$
ATLAS_FT_EFF_Eigen_b_2	$0.0408^{+0.998}_{-0.998}$
ATLAS_FT_EFF_Eigen_c_0	-0.0104^{+1}_{-1}
ATLAS_FT_EFF_Eigen_c_1	$9.68e-05^{+1}_{-1}$
ATLAS_FT_EFF_Eigen_c_2	$1.26e-05^{+1}_{-1}$
ATLAS_FT_EFF_Eigen_light_0	$0.27^{+0.958}_{-0.955}$
ATLAS_FT_EFF_Eigen_light_1	0.013^{+1}_{-1}
ATLAS_FT_EFF_Eigen_light_2	$3.19e-05^{+1}_{-1}$
ATLAS_FT_EFF_Eigen_light_3	0.00403^{+1}_{-1}
ATLAS_FT_EFF_Eigen_light_4	0.000828^{+1}_{-1}
ATLAS_FT_EFF_extrapolation	$-1.91e-11^{+1}_{-1}$
ATLAS_FT_EFF_extrapolation_from_charm	$5.39e-05^{+1}_{-1}$
ATLAS_JER_NP_0	$-0.361^{+0.341}_{-0.286}$
ATLAS_JER_NP_1	$0.0258^{+0.459}_{-0.466}$
ATLAS_JER_NP_2	$-0.299^{+0.426}_{-0.394}$
ATLAS_JER_NP_3	$-0.191^{+0.33}_{-0.309}$
ATLAS_JER_NP_4	$-0.186^{+0.367}_{-0.402}$
ATLAS_JER_NP_5	$-0.292^{+0.474}_{-0.51}$
ATLAS_JER_NP_6	$-0.113^{+0.5}_{-0.472}$
ATLAS_JER_NP_7	$0.00113^{+0.463}_{-0.45}$
ATLAS_JER_NP_8	$0.339^{+0.508}_{-0.647}$

Nuisance parameter	Postfit value (in σ unit)
ATLAS_Forward_JVT	$2.19e-05^{+1}_{-1}$
ATLAS_JER_CROSSCALIBFWD	$0.33^{+0.665}_{-0.676}$
ATLAS_JER_NOISEFWD	$0.488^{+0.712}_{-0.689}$
ATLAS_JES_EffectiveNP_1	$-0.323^{+1.16}_{-0.708}$
ATLAS_JES_EffectiveNP_2	$0.071^{+0.707}_{-0.685}$
ATLAS_JES_EffectiveNP_3	$0.0551^{+0.728}_{-0.765}$
ATLAS_JES_EffectiveNP_4	$-0.0653^{+0.974}_{-0.959}$
ATLAS_JES_EffectiveNP_5	$-0.0311^{+0.986}_{-0.985}$
ATLAS_JES_EffectiveNP_6	$-0.035^{+0.964}_{-0.978}$
ATLAS_JES_EffectiveNP_7	$0.131^{+0.82}_{-0.789}$
ATLAS_JES_EffectiveNP_8	$-0.0976^{+1.02}_{-1}$
ATLAS_JES_EtaInter_Model	$0.673^{+0.659}_{-0.76}$
ATLAS_JES_EtaInter_NonClosure	$0.147^{+0.853}_{-0.828}$
ATLAS_JES_EtaInter_Stat	$0.392^{+0.898}_{-0.713}$
ATLAS_JES_Flavor_Comp	$0.201^{+0.944}_{-0.971}$
ATLAS_JES_Flavor_Comp_lephadzll	$-0.0285^{+0.986}_{-0.996}$
ATLAS_JES_Flavor_Comp_leplepzll	$-0.0307^{+0.95}_{-0.925}$
ATLAS_JES_Flavor_Resp	$-0.537^{+0.642}_{-0.772}$
ATLAS_JES_Flavor_Resp_lephadzll	$0.00813^{+0.996}_{-0.999}$
ATLAS_JES_Flavor_Resp_leplepzll	$0.011^{+0.872}_{-0.861}$
ATLAS_JES_PU_OffsetMu	$0.00321^{+0.758}_{-0.842}$
ATLAS_JES_PU_OffsetNPV	$-0.342^{+0.828}_{-0.826}$
ATLAS_JES_PU_PtTerm	$-0.687^{+0.781}_{-0.714}$
ATLAS_JES_PU_Rho	$-0.439^{+0.537}_{-0.523}$
ATLAS_JVT	0.000624^{+1}_{-1}
ATLAS_MET_SoftTrk_ResoPara	$0.694^{+0.631}_{-0.638}$
ATLAS_MET_SoftTrk_ResoPerp	$-0.0948^{+0.815}_{-0.805}$
ATLAS_MET_SoftTrk_Scale	$-0.000406^{+0.655}_{-0.67}$
ATLAS_MUONS_ID	$0.0933^{+0.969}_{-0.92}$
ATLAS_MUONS_MS	$-0.00231^{+0.99}_{-0.99}$
ATLAS_MUONS_SAGITTA_RESBIAS	$-0.0365^{+0.993}_{-0.994}$
ATLAS_MUONS_SAGITTA_RHO	$-0.00992^{+0.999}_{-0.998}$
ATLAS_MUONS_SCALE	$0.0605^{+1.04}_{-1.05}$
ATLAS_MUON_EFF_STAT	$3.45e-05^{+1}_{-1}$
ATLAS_MUON_EFF_SYS	0.0118^{+1}_{-1}
ATLAS_MUON_EFF_TrigStat2015	-0.000146^{+1}_{-1}
ATLAS_MUON_EFF_TrigStat2016	-0.000146^{+1}_{-1}
ATLAS_MUON_EFF_TrigSyst2015	$-8.05e-05^{+1}_{-1}$
ATLAS_MUON_EFF_TrigSyst2016	$-8.05e-05^{+1}_{-1}$
ATLAS_MUON_ISO_STAT	$3.56e-07^{+1}_{-1}$
ATLAS_MUON_ISO_SYS	$-9.06e-06^{+1}_{-1}$
ATLAS_PRW_DATASF	$-0.886^{+0.684}_{-0.673}$
LuminosityUncCombined	$0.103^{+0.991}_{-0.99}$
ATLAS_TAU_EFF_TRIG_STATDATA2015	-0.0131^{+1}_{-1}
ATLAS_TAU_EFF_TRIG_STATDATA2016	$-0.493^{+0.979}_{-0.977}$
ATLAS_TAU_EFF_TRIG_STATMC2016	$-0.378^{+0.992}_{-0.991}$
ATLAS_TAU_EFF_TRIG_SYST2015	$-1.49e-05^{+1}_{-1}$

Nuisance parameter	Postfit value (in σ unit)
ATLAS_TAU_EFF_ELEORL_TRUEELE	$-0.0142^{+0.999}_{-0.999}$
ATLAS_TAU_EFF_ELEORL_TRUEHADTAU	$-0.539^{+0.971}_{-0.967}$
ATLAS_TAU_EFF_ID_HIGHPT	$7.16e-05^{+1}_{-1}$
ATLAS_TAU_EFF_ID_TOTAL	$-1.03^{+0.654}_{-0.661}$
ATLAS_TAU_EFF_RECO_HIGHPT	$-1.91e-11^{+1}_{-1}$
ATLAS_TAU_EFF_RECO_TOTAL	$-0.465^{+0.929}_{-0.92}$
ATLAS_TAU_TES_DETECTOR	$1.27^{+0.672}_{-0.656}$
ATLAS_TAU_TES_INSITU	$-0.689^{+0.534}_{-0.529}$
ATLAS_TAU_TES_MODEL	$-0.22^{+0.807}_{-0.858}$
Theo_NLO_EW_Higgs_total	0.00427^{+1}_{-1}
Theo_QCDscale_VBF_total	0.000747^{+1}_{-1}
Theo_QCDscale_VH_total	-0.0014^{+1}_{-1}
Theo_QCDscale_ttH_total	0.00156^{+1}_{-1}
Theo_VBFH_MUR_MUF	$0.00256^{+0.998}_{-0.998}$
Theo_VBFH_shower	$0.0489^{+0.981}_{-0.986}$
Theo_VH_MUR_MUF	-0.0032^{+1}_{-1}
Theo_alphas_Higgs_VBF_total	0.00107^{+1}_{-1}
Theo_alphas_Higgs_VH_total	-0.000783^{+1}_{-1}
Theo_alphas_Higgs_ggH_total	-0.00626^{+1}_{-1}
Theo_alphas_Higgs_ttH_total	0.000413^{+1}_{-1}
Theo_ggH_shower	$-0.334^{+0.915}_{-0.909}$
Theo_ggH_sig_qcd_0	$-0.0158^{+0.997}_{-0.996}$
Theo_ggH_sig_qcd_1	$-0.0171^{+0.997}_{-0.997}$
Theo_ggH_sig_qcd_2	$0.00192^{+0.998}_{-0.997}$
Theo_ggH_sig_qcd_3	$-0.0666^{+0.999}_{-0.997}$
Theo_ggH_sig_qcd_4	$-0.0172^{+0.999}_{-0.999}$
Theo_ggH_sig_qcd_5	0.00437^{+1}_{-1}
Theo_ggH_sig_qcd_6	$-0.0464^{+0.998}_{-0.996}$
Theo_ggH_sig_qcd_7	$-0.137^{+1}_{-0.99}$
Theo_ggH_sig_qcd_8	$-0.0738^{+0.999}_{-0.997}$
Theo_hh_VH_PSUE	-0.00422^{+1}_{-1}
Theo_hh_boost_VBFH_PSUE	-0.00366^{+1}_{-1}
Theo_hh_boost_ggH_PSUE	-0.0178^{+1}_{-1}
Theo_hh_vbf_VBFH_PSUE	0.00133^{+1}_{-1}
Theo_hh_vbf_ggH_PSUE	$-0.000294^{+0.999}_{-0.999}$
Theo_lh_VH_PSUE	0.000563^{+1}_{-1}
Theo_lh_boost_VBFH_PSUE	0.00252^{+1}_{-1}
Theo_lh_boost_ggH_PSUE	$0.0198^{+0.999}_{-0.999}$
Theo_lh_vbf_VBFH_PSUE	-0.00823^{+1}_{-1}
Theo_lh_vbf_ggH_PSUE	$-0.0202^{+0.999}_{-0.999}$
Theo_ll_VH_PSUE	-0.000384^{+1}_{-1}
Theo_ll_boost_VBFH_PSUE	-0.000261^{+1}_{-1}
Theo_ll_boost_ggH_PSUE	0.00163^{+1}_{-1}
Theo_ll_vbf_VBFH_PSUE	0.0073^{+1}_{-1}
Theo_ll_vbf_ggH_PSUE	-0.00493^{+1}_{-1}
Theo_pdf_Higgs_VBF_total	0.00448^{+1}_{-1}
Theo_pdf_Higgs_VH_total	-0.00135^{+1}_{-1}

Nuisance parameter	Postfit value (in σ unit)
Theo_pdf_Higgs_ggH_total	$-0.00371^{+0.999}_{-0.999}$
Theo_pdf_Higgs_ttH_total	0.000619^{+1}_{-1}
Theo_sig_alphaS	$-0.0278^{+0.998}_{-0.998}$
Theo_sig_pdf_0	-0.000159^{+1}_{-1}
Theo_sig_pdf_1	0.000178^{+1}_{-1}
Theo_sig_pdf_14	$6.98e-06^{+1}_{-1}$
Theo_sig_pdf_16	-0.0139^{+1}_{-1}
Theo_sig_pdf_18	$-3.86e-07^{+1}_{-1}$
Theo_sig_pdf_20	$-1.17e-05^{+1}_{-1}$
Theo_sig_pdf_27	$-7.11e-05^{+1}_{-1}$
Theo_sig_pdf_29	$-2.04e-05^{+1}_{-1}$
Theo_sig_pdf_3	-0.000884^{+1}_{-1}
Theo_sig_pdf_4	0.018^{+1}_{-1}
Theo_sig_pdf_5	$1.74e-05^{+1}_{-1}$
ZttTheory_CKK_Relative_Bst	$0.41^{+0.772}_{-0.855}$
ZttTheory_CKK_Relative_VBF	$-0.265^{+0.854}_{-0.933}$
ZttTheory_CKK_boost_hadhad	$0.213^{+0.453}_{-0.498}$
ZttTheory_CKK_boost_lephad	$0.476^{+0.467}_{-0.443}$
ZttTheory_CKK_boost_leplep	$-0.305^{+0.867}_{-0.946}$
ZttTheory_CKK_vbf_hadhad	$0.0673^{+0.921}_{-0.973}$
ZttTheory_CKK_vbf_lephad	$-0.0427^{+0.942}_{-0.968}$
ZttTheory_CKK_vbf_leplep	-0.000208^{+1}_{-1}
ZttTheory_MGvsSH_Relative_Bst	$-0.518^{+0.957}_{-0.958}$
ZttTheory_MGvsSH_Relative_VBF	$0.368^{+0.814}_{-0.808}$
ZttTheory_MGvsSH_boost_hadhad	$0.232^{+0.945}_{-0.943}$
ZttTheory_MGvsSH_boost_lephad	$0.142^{+0.788}_{-0.779}$
ZttTheory_MGvsSH_boost_leplep	$0.148^{+0.613}_{-0.597}$
ZttTheory_MGvsSH_vbf_hadhad	$-0.0846^{+0.916}_{-0.909}$
ZttTheory_MGvsSH_vbf_lephad	$0.121^{+0.963}_{-0.959}$
ZttTheory_MGvsSH_vbf_leplep	$0.0496^{+0.971}_{-0.974}$
ZttTheory_MUR_MUF_Relative_Bst	$-0.00347^{+0.925}_{-0.929}$
ZttTheory_MUR_MUF_Relative_VBF	$-0.105^{+1}_{-0.998}$
ZttTheory_MUR_MUF_boost_hadhad	$-0.0287^{+0.9}_{-0.928}$
ZttTheory_MUR_MUF_boost_lephad	$-0.146^{+0.904}_{-0.941}$
ZttTheory_MUR_MUF_boost_leplep	$-0.0524^{+0.971}_{-0.998}$
ZttTheory_MUR_MUF_vbf_hadhad	$0.000287^{+0.998}_{-0.998}$
ZttTheory_MUR_MUF_vbf_lephad	$0.0334^{+0.971}_{-0.974}$
ZttTheory_MUR_MUF_vbf_leplep	$0.11^{+0.983}_{-0.974}$
ZttTheory_PDF_Relative_Bst	$0.187^{+0.999}_{-1.01}$
ZttTheory_PDF_Relative_VBF	$0.0242^{+0.998}_{-0.997}$
ZttTheory_PDF_boost_hadhad	$-0.131^{+1}_{-0.991}$
ZttTheory_PDF_boost_leplep	$-0.0607^{+1}_{-0.995}$
ZttTheory_PDF_vbf_hadhad	$0.00803^{+0.998}_{-0.998}$
ZttTheory_PDF_vbf_leplep	-0.00203^{+1}_{-1}
ZttTheory_QSF_Relative_Bst	$-0.0718^{+0.851}_{-0.836}$
ZttTheory_QSF_Relative_VBF	$-0.117^{+0.999}_{-0.995}$
ZttTheory_QSF_boost_lephad	0.00259^{+1}_{-1}

Nuisance parameter	Postfit value (in σ unit)
ZttTheory_QSF_boost_leplep	$-4.46e-05^{+1}_{-1}$
ZttTheory_QSF_vbf_leplep	-0.000161^{+1}_{-1}
Z_EWK_proportion	$0.0066^{+0.997}_{-0.997}$
hh_dPhiWeightClosSys	$-0.0145^{+0.893}_{-0.883}$
hh_dPhiWeightStat	0.00186^{+1}_{-1}
hh_fake_contamination	0.000434^{+1}_{-1}
lh_fake_nonclosure	$-0.142^{+0.401}_{-0.359}$
lh_fake_rvar_boost	$-0.416^{+0.954}_{-0.977}$
lh_fake_rvar_vbf	$0.0336^{+0.996}_{-0.996}$
lh_fake_stat_boost	$0.201^{+0.605}_{-0.593}$
lh_fake_stat_boost_top	$0.0376^{+0.999}_{-0.999}$
lh_fake_stat_vbf	$0.607^{+0.499}_{-0.52}$
lh_fake_stat_vbf_top	$0.0614^{+0.993}_{-0.992}$
ll_fake_nonclosure	$-0.498^{+0.37}_{-0.482}$
ll_fake_stat	-0.0179^{+1}_{-1}